Magic angles in twisted bilayer graphene near commensuration: Towards a hypermagic regime

Michael G. Scheer, Kaiyuan Gu, and Biao Lian Department of Physics, Princeton University, Princeton, New Jersey 08544, USA

(Received 28 March 2022; revised 29 August 2022; accepted 30 August 2022; published 15 September 2022)

The Bistritzer-MacDonald continuum model (BM model) describes the low-energy moiré bands for twisted bilayer graphene (TBG) at small twist angles. We derive a generalized continuum model for TBG near any commensurate twist angle, which is characterized by complex interlayer hoppings at commensurate AA stackings (rather than the real hoppings in the BM model), a real interlayer hopping at commensurate AB/BA stackings, and a global energy shift. The complex phases of the AA stacking hoppings and the twist angle together define a single angle parameter ϕ_0 . We compute the model parameters for the first six distinct commensurate TBG configurations, among which the 38.2° configuration may be within experimentally observable energy scales. We identify the first magic angle for any ϕ_0 at a condition similar to that of the BM model. At this angle, the lowest two moiré bands at charge neutrality become flat except near the Γ_M point and retain fragile topology but lose particle-hole symmetry. We further identify a hypermagic parameter regime centered at $\phi_0 = \pm \pi/2$ where many moiré bands around charge neutrality (often 8 or more) become flat simultaneously. Many of these flat bands resemble those in the kagome lattice and p_x , p_y 2-orbital honeycomb lattice tight-binding models.

DOI: 10.1103/PhysRevB.106.115418

I. INTRODUCTION

At certain discrete commensurate twist angles θ_0 , the honeycomb lattices of two graphene layers align to form a perfectly periodic superlattice [1,2]. The simplest such commensurate configuration is $\theta_0 = 0$ in which two layers of graphene are aligned with no twist. Bistritzer and MacDonald demonstrated that if two layers of graphene are twisted by a small angle relative to this $\theta_0 = 0$ configuration, forming twisted bilayer graphene (TBG), a moiré superlattice emerges, and the low energy single particle physics can be described by a continuum model [3]. Furthermore, at the so called magic angle, $\theta \approx 1.05^{\circ}$, this model predicts that the lowest two moiré bands (i.e., the first conduction and valence bands) at charge neutrality become approximately flat. Moreover, it has been shown that the two flat bands carry a fragile topology [4-8], obstructing the construction of maximally localized symmetric Wannier orbitals [9–14]. In this flat band regime, the physics is dominated by interactions. Interacting electronic states such as correlated insulators, superconductors, and Chern insulators have been observed [15–33], the mechanisms of which have been studied extensively [34–59]. Flat bands and interacting electronic states are also present in other two dimensional moiré materials such as twisted double bilayer graphene [60–63], twisted trilayer and multilayer graphene [64–69], ABC trilayer graphene [70–73], and twisted transition metal dichalcogenides [74–76]. For the purpose of exploring interacting states, the search for more flat band moiré platforms is important.

In this paper, we search for flat moiré bands in TBG twisted by a small angle relative to an arbitrary commensurate configuration. That is to say, we consider a twist angle $\theta = \theta_0 + \delta\theta$

where θ_0 is a commensurate angle and $\delta\theta$ is small. Without loss of generality, we can choose $0 \le \theta_0 < \pi/3$ because of the crystalline symmetries of TBG. When $\theta_0 = 0$, the interlayer hopping couples states near the top and bottom layer **K** points only among themselves. This allows one to explicitly derive the form of the Bistritzer-MacDonald continuum model (BM model) by computing the interlayer hopping in reciprocal space and making a few well-justified approximations [3]. However, for all other commensurate configurations, the calculations are more complicated since states near the top and bottom **K** points are coupled to many other states. The origin of this complication is the fact that the commensurate unit cell contains 4N atoms, where the integer N is 1 when $\theta_0 = 0$ but is 7 or greater for all other commensurate configurations [2].

Assuming that the interlayer hopping is not too strong, the states far from the top and bottom K points influence the low energy physics perturbatively. Rather than explicitly applying perturbation theory, we take an approach based on symmetry and parameter determination from a microscopic tight-binding model. We first show, based on an analysis of the magnitudes of the hopping terms, that the system is approximated by a continuum model of a certain general form. We then use the exact unitary and antiunitary crystalline symmetries of TBG to constrain the coefficients of this general model. Near a commensurate twist angle θ_0 , we arrive at a TBG continuum model containing four real parameters χ_0 , w_0, w_1 , and w_2 , which are ultimately determined by the microscopic hopping parameters. We show that w_1 controls the interlayer hopping at the commensurate AB and BA stacking configurations while $w_0e^{i\chi_0}$ and $w_0e^{-i\chi_0}$ control the interlayer hoppings at the commensurate AA stacking configuration. w_2 is simply a global energy shift. When $\theta_0 = 0$, the value of χ_0 is negligible because of an approximate mirror symmetry, and we recover the BM model.

In order to determine the model parameters near general commensurate configurations, we consider the geometry of TBG in real space. The key observation is that a small relative rotation $\delta\theta$ of the two graphene layers can be locally approximated by an interlayer translation [77]. By carefully taking the limit $\delta\theta \to 0$, we derive the model for commensurate twist angle θ_0 and interlayer displacement **d** from the model for twist angle $\theta = \theta_0 + \delta\theta$. We then determine the continuum model parameters from a numerical computation of the microscopic tight-binding model (without lattice relaxation or corrugation [78]) at commensurate angle θ_0 with two values of d corresponding to AA and AB stacking configurations. For the case $\theta_0 = 0$, we recover $w_0 \approx w_1 \approx 110 \,\mathrm{meV}$, $\chi_0 = 0$, $w_2 = 0$ 0 in agreement with the BM model. We additionally provide numerical values of the model parameters for the next five commensurate configurations in order of the number of atoms per commensurate unit cell. When determining the continuum model parameters, we only use numerical tight-binding results at a single crystal momentum (the commensurate K point) and two **d** vectors. However, we find that the continuum model matches the tight-binding model with high accuracy for all crystal momenta in the commensurate K valley and all d vectors. It is worth noting that in the first five nontrivial (i.e., $\theta_0 \neq 0$) commensurate configurations, the new parameters χ_0 and w_2 are non-negligible. Although we do not consider lattice relaxation or corrugation, we note that these effects can alter the values of the model parameters, but not the general form of the continuum model (assuming these effects preserve the moiré lattice symmetries) [10,78,79]. We note also the possibility that the model parameters can be altered by the effects of higher graphene bands which we do not consider.

Next, we compute the moiré band structures of TBG with twist angle near the first six commensurate configurations. By both the "tripod model" approximation [3,80] and accurate numerical computations, we identify the condition for the first magic angle in any nearly commensurate TBG system [Eqs. (66) and (67)]. This condition is similar to that of the original BM model. A further simplification of the generic TBG continuum model indicates that the moiré band structure only depends on a single angle variable $\phi_0 = \chi_0 + \theta_0/2$. At the first magic angle, the lowest two bands at charge neutrality in the nearly commensurate TBG model with $\phi_0 \neq 0$ are flat in most of the moiré Brillouin zone except in the vicinity of the Γ_M point. These bands are no longer particle-hole symmetric, though they do retain fragile topology. According to our model, the first magic angle near any nonzero commensurate twist angle θ_0 (e.g., the magic angle 0.004° near $\theta_0 \approx 38.2^{\circ}$) may be too small to be realized experimentally. However, it is possible that spontaneous commensurate atomic structural reconstructions (e.g., charge density wave orders), lattice relaxation or corrugation, or effective couplings mediated by higher graphene bands may enhance the moiré potential and enlarge the magic angles.

Finally, we reveal the existence of a *hypermagic regime* centered at $\phi_0 = \pm \pi/2$ where several moiré bands (often 8 or more) near charge neutrality become extremely flat simultaneously. The second and third magic angles in the chiral limit [12] are contained in the hypermagic regime, and for

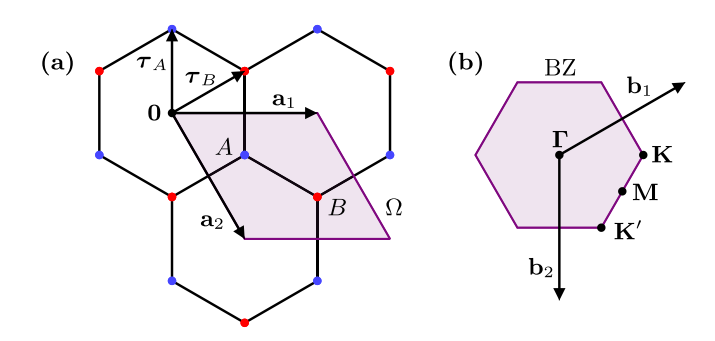


FIG. 1. Illustration of the definitions of quantities in Sec. II A. (a) The graphene lattice and its primitive unit cell. (b) The reciprocal lattice primitive vectors, Brillouin zone, and high-symmetry crystal momenta

these parameters the lowest two bands at charge neutrality have fragile topology [4–8]. On the other hand, for many parameters in the hypermagic regime the lowest bands at charge neutrality have trivial topology. In such cases, we expect that the strongly interacting physics may be similar to that of the Hubbard model with trivial bands and may host antiferromagnetic states. Interestingly, many of the flat bands in the hypermagic regime resemble those of the kagome lattice and p_x , p_y 2-orbital honeycomb lattice tight-binding models, which are known to exhibit flat bands [81,82].

The rest of this paper is organized as follows. Section II derives the generic form of the low energy TBG continuum model near commensuration from a microscopic graphene Hamiltonian. Section III further restricts the form of the TBG continuum model using crystalline symmetries, and gives the model parameters for the first six commensurate configurations. In Sec. IV, we discuss the low energy bands (namely, the first two conduction and valence bands) of commensurate TBG. Then in Sec. V, we compute the moiré band structure near several commensurate configurations with the actual model parameters and give the condition for the first magic angle. In Sec. VI, we further explore the parameter space of the nearly commensurate TBG continuum model, reveal the hypermagic regime, and investigate the topology of the moiré bands. Finally, we give a high level discussion in Sec. VII.

II. DERIVATION OF THE GENERIC CONTINUUM MODEL

A. Microscopic Hamiltonian

The honeycomb lattice of monolayer graphene consists of two sublattices A and B. We will often make the identifications A=1 and B=-1 when using A and B in equations. As shown in Fig. 1(a), the positions of the carbon atoms in sublattice α are given by $\mathbf{r}+\boldsymbol{\tau}_{\alpha}$ for $\alpha\in\{A,B\}$, \mathbf{r} in a triangular Bravais lattice L, and constant vectors $\mathbf{\tau}_{\alpha}$. It is convenient to choose the primitive vectors $(\mathbf{a}_1,\mathbf{a}_2)$ for L where $\mathbf{a}_1=a_0\sqrt{3}\hat{\mathbf{x}}$, $\mathbf{a}_2=R_{-\pi/3}\mathbf{a}_1, a_0\approx 0.142$ nm is the interatomic distance, and R_{ϕ} denotes rotation by angle ϕ about the $\hat{\mathbf{z}}$ axis. Additionally, we choose $\mathbf{\tau}_A=a_0\hat{\mathbf{y}}$ and $\mathbf{\tau}_B=R_{-\pi/3}\mathbf{\tau}_A$ so that the origin $\mathbf{0}$ is in the center of a hexagon. We define Ω to be the primitive unit cell of L and $|\Omega|$ to be its area.

The Bravais lattice *P* that is reciprocal to *L* has primitive vectors $(\mathbf{b}_1, \mathbf{b}_2)$ with $\mathbf{b}_1 = R_{2\pi/3}\mathbf{b}_2$ and $\mathbf{b}_2 = -4\pi\hat{\mathbf{y}}/(3a_0)$ so

that $\mathbf{b}_j \cdot \mathbf{a}_k = 2\pi \delta_{j,k}$. Explicitly, the lattices L and P are given by

$$L = \{n_1 \mathbf{a}_1 + n_2 \mathbf{a}_2 | n_1, n_2 \in \mathbb{Z} \},$$

$$P = \{n_1 \mathbf{b}_1 + n_2 \mathbf{b}_2 | n_1, n_2 \in \mathbb{Z} \}.$$
 (1)

We define the Brillouin zone BZ to be the Wigner-Seitz unit cell of P and |BZ| to be its area. Note that $|\Omega||BZ| = (2\pi)^2$. We additionally define the high-symmetry crystal momenta

$$\Gamma = \mathbf{0},
\mathbf{K} = \frac{2}{3}\mathbf{b}_{1} + \frac{1}{3}\mathbf{b}_{2} = \frac{4\pi\sqrt{3}}{9a_{0}}\hat{\mathbf{x}},
\mathbf{K}' = \frac{1}{3}\mathbf{b}_{1} + \frac{2}{3}\mathbf{b}_{2} = R_{-\pi/3}\mathbf{K},
\mathbf{M} = \frac{1}{2}\mathbf{b}_{1} + \frac{1}{2}\mathbf{b}_{2} = \frac{1}{2}\mathbf{K} + \frac{1}{2}\mathbf{K}',$$
(2)

which are shown in Fig. 1(b).

We consider a system consisting of two stacked graphene layers denoted by $l \in \{+, -\}$. We rotate layer l by the angle $-l\theta/2$ about the origin $\mathbf{0}$ and then translate it by an in-plane vector $-l\mathbf{d}/2$, so that θ and \mathbf{d} are the relative rotation and translation of the two layers. We show in Appendix \mathbf{C} that when θ is not a commensurate angle, a change in the translation vector \mathbf{d} is equivalent to a unitary change of basis, but this is not generally the case when θ is a commensurate angle.

Let L_l , P_l , and BZ $_l$ be the real space lattice, reciprocal lattice, and graphene Brillouin zone of layer l. Explicitly, $L_l = R_{-l\theta/2}L$, $P_l = R_{-l\theta/2}P$, and BZ $_l = R_{-l\theta/2}BZ$ where we use the notation $RS = \{Rs|s \in S\}$ for a set S of vectors and an operator or number R. We will additionally use the notations $S_1 \cap S_2$ and $S_1 \cup S_2$ for the intersection and union of sets S_1 , S_2 , as well as the notations $S_1 + S_2 = \{s_1 + s_2 | s_1 \in S_1, s_2 \in S_2\}$ and $s_1 + S_2 = \{s_1 + s_2 | s_2 \in S_2\}$ where s_1 is a vector and S_1 , S_2 are sets of vectors.

We neglect electron spin when describing the single-particle model because of the weak spin-orbit coupling in graphene [83]. The spinless p_z orbitals $|\mathbf{r}, l, \alpha\rangle$ for $\mathbf{r} \in L_l$, $l \in \{+, -\}$, and $\alpha \in \{A, B\}$ form an orthonormal basis for the Hilbert space. The orbital $|\mathbf{r}, l, \alpha\rangle$ is localized at position $\mathbf{r} + \mathbf{\tau}_{\alpha}^l$ where $\mathbf{\tau}_{\alpha}^l = R_{-l\theta/2}\mathbf{\tau}_{\alpha} - l\mathbf{d}/2$. Note that \mathbf{d} enters the formalism only through the definition of $\mathbf{\tau}_{\alpha}^l$.

The Bloch states are defined by

$$|\mathbf{k}, l, \alpha\rangle = \frac{1}{\sqrt{|\mathrm{BZ}|}} \sum_{\mathbf{r} \in L} e^{i\mathbf{k} \cdot (\mathbf{r} + \tau_{\alpha}^{l})} |\mathbf{r}, l, \alpha\rangle$$
 (3)

for crystal momentum vectors $\mathbf{k} \in \mathbb{R}^2$ and satisfy the normalization condition

$$\langle \mathbf{k}', l', \alpha' | \mathbf{k}, l, \alpha \rangle$$

$$= \delta_{l',l} \delta_{\alpha',\alpha} \sum_{\mathbf{G} \in P_l} \delta^2(\mathbf{k}' - \mathbf{k} - \mathbf{G}_l) e^{-i\tau_{\alpha}^l \cdot \mathbf{G}_l}. \tag{4}$$

Note that the origin for crystal momenta is Γ , defined in Eq. (2) and shown in Fig. 1. The Bloch states $|\mathbf{k}, l, \alpha\rangle$ with $\mathbf{k} \in \mathrm{BZ}_l$ form a continuous basis for the Hilbert space. However, for convenience we will sometimes use the overcomplete set formed by all Bloch states $|\mathbf{k}, l, \alpha\rangle$ for $\mathbf{k} \in \mathbb{R}^2$.

We consider a microscopic single-particle Hamiltonian *H* with matrix elements

$$\langle \mathbf{r}', l', \alpha' | H | \mathbf{r}, l, \alpha \rangle$$

$$= t_{l' \cdot l} (\mathbf{r}' + \boldsymbol{\tau}_{\alpha'}^{l'} - \mathbf{r} - \boldsymbol{\tau}_{\alpha}^{l}) - \mu \delta_{\mathbf{r}', \mathbf{r}} \delta_{l', l} \delta_{\alpha', \alpha}, \qquad (5)$$

where μ is a chemical potential and $t_{\pm}: \mathbb{R}^2 \to \mathbb{R}$ are rotationally symmetric functions (i.e., $t_{\pm}(\mathbf{r})$ depends only on $|\mathbf{r}|$) determining the intra- and interlayer hoppings. We allow the functions $t_{\pm}(\mathbf{r})$ to remain unspecified for now. The intralayer matrix elements are given by

$$\langle \mathbf{k}', l, \alpha' | H | \mathbf{k}, l, \alpha \rangle$$

$$= \langle \mathbf{k}', l, \alpha' | \mathbf{k}, l, \alpha' \rangle \left(-\mu + \sum_{\mathbf{r} \in L + \tau_{\alpha'} - \tau_{\alpha}} e^{-i(R_{l\theta/2}\mathbf{k}) \cdot \mathbf{r}} t_{+}(\mathbf{r}) \right)$$
(6)

(see Appendix A). If the value of μ is chosen appropriately, then for crystal momenta near $\mathbf{K}_l = R_{-l\theta/2}\mathbf{K}$, this matrix element can be approximated by a Dirac cone

$$\langle \mathbf{K}_{l} + \mathbf{p}', l, \alpha' | H | \mathbf{K}_{l} + \mathbf{p}, l, \alpha \rangle$$

$$= (\hbar v_{F}(\sigma_{l\theta/2} \cdot \mathbf{p})_{\alpha',\alpha} + O(|\mathbf{p}|^{2})) \delta^{2}(\mathbf{p}' - \mathbf{p}). \tag{7}$$

Here, $\sigma_{\phi} = e^{-i(\phi/2)\sigma_z}(\sigma_x \hat{\mathbf{x}} + \sigma_y \hat{\mathbf{y}})e^{i(\phi/2)\sigma_z}$ is a vector of rotated Pauli matrices satisfying

$$\boldsymbol{\sigma}_{\phi} \cdot \mathbf{p} = \boldsymbol{\sigma}_{0} \cdot (R_{\phi} \mathbf{p}) = \begin{pmatrix} 0 & \text{H.c.} \\ e^{i\phi}(p_{x} + ip_{y}) & 0 \end{pmatrix}$$
(8)

and v_F is the Fermi velocity, which depends on the function $t_+(\mathbf{r})$. We make the assumption throughout the paper that $v_F > 0$. See Appendix B for a derivation of Eq. (7) based on symmetry. The matrix elements for crystal momenta near the other Brillouin zone corners $R_{n\pi/3}\mathbf{K}_l$ for $1 \le n \le 5$ are given by similar Dirac cone Hamiltonians.

The interlayer matrix elements are given by

$$\langle \mathbf{k}', -l, \alpha' | H | \mathbf{k}, l, \alpha \rangle$$

$$= \sum_{\mathbf{G}_{-} \in P_{-}} \sum_{\mathbf{G}_{+} \in P_{+}} \frac{\hat{t}_{-}(\mathbf{k} + \mathbf{G}_{l})}{|\Omega|} e^{i\tau_{\alpha'}^{-l} \cdot \mathbf{G}_{-l}} e^{-i\tau_{\alpha}^{l} \cdot \mathbf{G}_{l}} \delta^{2}(\mathbf{k} + \mathbf{G}_{l} - \mathbf{k}' - \mathbf{G}_{-l}). \tag{9}$$

where the hatted functions $\hat{t}_{\pm}(\mathbf{k})$ are the two dimensional Fourier transforms of $t_{\pm}(\mathbf{r})$ (see Appendix A). We see that H is block diagonal: the Bloch states $|\mathbf{k}', l', \alpha'\rangle$ and $|\mathbf{k}, l, \alpha\rangle$ are in the same Hamiltonian block if and only if

$$\mathbf{k}' - \mathbf{k} \in P_- + P_+. \tag{10}$$

B. Commensurate configurations

Since layer l is invariant under translation by elements of the graphene Bravais lattice L_l , the bilayer system is invariant under translations by elements of $L_- \cap L_+$. Commensurate configurations are those for which $L_- \cap L_+ \neq \{0\}$, in which case $L_- \cap L_+$ forms a Bravais lattice called the commensuration superlattice. Let $\theta = \theta_0$ be a commensurate angle, by which we mean the twist angle for a commensurate configuration.

TABLE I. Numerically determined model parameters reported with three significant figures. For the more accurate parameters used in Figs. 5 to 7, 15, 16, and 18, see Appendix Table II.

(m, n)	θ_0	N	S	Xο	(w_0, w_1)	w_2
(1, 0)	0 °	1	1	0.00°	(113, 113) meV	0.0 meV
(5, 3)	38.2°	7	1	-3.10°	$(959, 1050) \mu eV$	$-4.44\mathrm{meV}$
(7, 3)	27.8°	13	-1	125°	$(5.50, 3.62) \mu eV$	$-4.43\mathrm{meV}$
(4, 3)	46.8°	19	1	-0.994°	$(33.2, 33.2) \mu eV$	$-4.32\mathrm{meV}$
(11, 3)	17.9°	31	1	1.24°	(653, 653) neV	$-4.43\mathrm{meV}$
(11, 9)	50.6°	37	1	-0.862°	(1300, 1300) neV	$-4.03\mathrm{meV}$

We show in Appendix C that the crystalline symmetries of TBG allow us to restrict our attention to configurations with $\theta_0 \in [0, \pi/3)$. These configurations can be enumerated by a pair of relatively prime integers $m > n \ge 0$ with

$$\theta_0 = \cos^{-1}\left(\frac{3m^2 - n^2}{3m^2 + n^2}\right) \tag{11}$$

(see Appendix D 1). The commensurate configuration corresponding to the pair (m, n) has 4N atoms per unit cell where the integer $N \ge 1$ is given in Eq. (D12) as a function of m and n.

As shown in Appendix D 3, if 3|n (i.e., 3 divides n), we have

$$\mathbf{K}_{+} - \mathbf{K}_{-}, \mathbf{K}'_{+} - \mathbf{K}'_{-} \in P_{-} + P_{+}$$
 (12)

and otherwise

$$\mathbf{K}_{+} - \mathbf{K}'_{-}, \mathbf{K}'_{+} - \mathbf{K}_{-} \in P_{-} + P_{+},$$
 (13)

where $\mathbf{K}_l = R_{-l\theta/2}\mathbf{K}$ and $\mathbf{K}_l' = R_{-l\theta/2}\mathbf{K}'$. Additionally, in either case, we have

$$\mathbf{K}_{+} - \mathbf{K}'_{+}, \mathbf{K}_{-} - \mathbf{K}'_{-} \notin P_{-} + P_{+}.$$
 (14)

If θ_0 is a commensurate angle then so is $\pi/3 - \theta_0$, and the Hamiltonians for these two configurations are unitarily equivalent (see Appendix C). Furthermore, we show in Appendix D 4 that among the two configurations corresponding to θ_0 and $\pi/3 - \theta_0$, one must satisfy 3|n while the other does not. As a result, we assume without loss of generality that 3|n and Eq. (12) holds. From here on, we will always assume 3|n unless we explicitly state otherwise. Table I lists properties of the first six commensurate configurations in increasing order of N. Figure 2 illustrates the locations of the atoms in real space for a particular commensurate configuration.

We saw in Eq. (10) that the microscopic Hamiltonian is block diagonal in accordance with the lattice $P_- + P_+$. We show in Appendix D 2 that when the system is commensurate, $P_- + P_+$ is the reciprocal lattice of the commensuration superlattice $L_- \cap L_+$. We see that the block diagonality can be attributed in this case to translation symmetry with respect to the commensuration superlattice. Each Hamiltonian block has a basis consisting of Bloch states with N nonequivalent crystal momenta in each layer, for a total dimension of 4N. As an example, Fig. 3(a) illustrates the crystal momenta involved in the Hamiltonian block containing K_+ and K_- for a particular commensurate configuration. We show in Appendix D 5 that

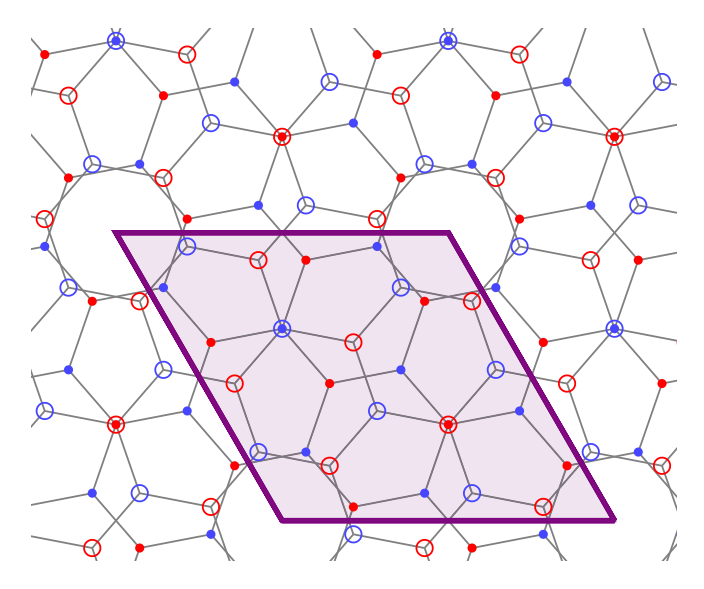


FIG. 2. The real space structure of commensurate TBG with (m, n) = (5, 3) and $\mathbf{d} = \mathbf{0}$, in which case $\theta_0 \approx 38.2^\circ$ and N = 7. The top (bottom) atoms are represented by dots (circles) and the A (B) sublattices in each layer are colored blue (red). The purple rhombus is an example of a primitive unit cell for the commensuration superlattice. This unit cell contains 4N = 28 atoms. Note that this configuration has AA stacking as described in Appendix D 6.

 $L_- \cap L_+ = \sqrt{N}L$ and $P_- + P_+ = P/\sqrt{N}$ so that the Brillouin zone BZ₀ corresponding to the commensuration superlattice is a regular hexagon.

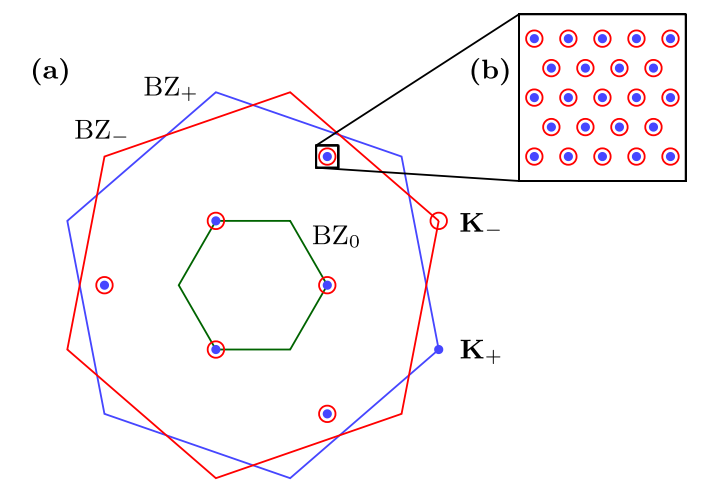


FIG. 3. (a) Illustration of the crystal momenta involved in the Hamiltonian block containing \mathbf{K}_+ and \mathbf{K}_- for the commensurate configuration with (m,n)=(5,3). The top (bottom) Brillouin zone boundaries are shown in blue (red) and the boundary of the Brillouin zone BZ₀ corresponding to the commensuration superlattice is shown in green. The N=7 top (bottom) layer momenta are marked with blue dots (red circles). All shown crystal momenta in a given layer differ by elements of $P_- + P_+$ and are contained in the given layer's Brillouin zone. (b) Illustration of the set $B_{l,q}$ defined in Sec. II D for l=+ or l=-, some large value q, and some small value $\delta\theta$. There is a lattice of crystal momenta near each point in (a).

C. Incommensurate configurations

We now consider an incommensurate twist angle θ . We show in Appendix E that in this case $P_- + P_+$ is a dense subset of \mathbb{R}^2 . As a result, the block diagonality of H given by Eq. (10) cannot be directly used to define a band structure. In this section, we will construct a notion of distance between Bloch states that can be used in place of block diagonality to analyze H.

We show in Appendix D 1 that since θ is incommensurate, we have $P_- \cap P_+ = \{0\}$. It follows that for any $l \in \{+, -\}$ and crystal momentum vectors \mathbf{k} , \mathbf{k}' with $\mathbf{k}' - \mathbf{k} \in P_- + P_+$ there are unique vectors $\mathbf{G}_- \in P_-$, $\mathbf{G}_+ \in P_+$ such that

$$\mathbf{k} + \mathbf{G}_l = \mathbf{k}' + \mathbf{G}_{-l}. \tag{15}$$

This pair of vectors \mathbf{G}_- , \mathbf{G}_+ determines the interlayer matrix element in Eq. (9). Since $\hat{t}_-(\mathbf{k})$ depends only on $|\mathbf{k}|$, the magnitude of $\langle \mathbf{k}', -l, \alpha' | H | \mathbf{k}, l, \alpha \rangle$ depends only on $|\mathbf{k} + \mathbf{G}_l|$. We assume that $\hat{t}_-(\mathbf{k})$ monotonically decreases with $|\mathbf{k}|$, so that interlayer matrix elements with large magnitude correspond to small values of $|\mathbf{k} + \mathbf{G}_l|$. Similarly, the intralayer matrix element in Eq. (6) is zero unless $\mathbf{k}' - \mathbf{k} \in P_l$. As a result, $\langle \mathbf{k}', l, \alpha' | H | \mathbf{k}, l, \alpha \rangle$ is only nonzero when \mathbf{k} and \mathbf{k}' are related as in Eq. (15) with $|\mathbf{G}_{-l}| = 0$.

With this motivation, we define a function d that quantifies the magnitude of the matrix elements of H

$$d(\mathbf{k}, l, \mathbf{k}', l') = \begin{cases} \infty & \text{if } \mathbf{k}' - \mathbf{k} \notin P_- + P_+ \\ |\mathbf{k} + \mathbf{G}_l| & \text{if } l' = -l \text{ and Eq. (15).} \\ |\mathbf{G}_{-l}| & \text{if } l' = l \text{ and Eq. (15)} \end{cases}$$
 (16)

We show in Appendix F that d satisfies

- (1) $d(\mathbf{k}, l, \mathbf{k}, l) = 0$,
- (2) $d(\mathbf{k}, l, \mathbf{k}', l') = d(\mathbf{k}', l', \mathbf{k}, l)$,
- (3) $d(\mathbf{k}, l, \mathbf{k''}, l'') \leq d(\mathbf{k}, l, \mathbf{k'}, l') + d(\mathbf{k'}, l', \mathbf{k''}, l'')$, so that d defines a notion of distance on the set $\mathbb{R}^2 \times \{+, -\}$. Suppose we define the distance between Bloch states $|\mathbf{k}, l, \alpha\rangle$, $|\mathbf{k'}, l', \alpha'\rangle$ to be $d(\mathbf{k}, l, \mathbf{k'}, l')$. Then by construction, the microscopic Hamiltonian H described by Eqs. (6) and (9) is local with respect to this notion of distance.

D. Continuum model for incommensurate configurations

We now take

$$\theta = \theta_0 + \delta\theta,\tag{17}$$

where θ_0 is a commensurate angle as in Eq. (11) and $\delta\theta$ is small. We assume that θ is an incommensurate angle so that the distance function d from Sec. II C is defined. We are interested in the single particle physics of H near the Fermi level at charge neutrality, as this determines the low energy excitations of the many-body Hamiltonian. In this section, we will derive a continuum model that approximates the relevant energies and eigenvectors of H.

We will make use of the following characterization of the distance function d that applies when $\theta = \theta_0 + \delta\theta$. Let $L_l^0 =$

 $R_{-l\theta_0/2}L$, $P_l^0=R_{-l\theta_0/2}P$, and recall from Sec. II B that $L_-^0\cap L_+^0$ is the commensuration superlattice corresponding to twist angle θ_0 and $P_-^0+P_+^0$ is its reciprocal lattice. Define the set

$$Q(\mathbf{k}, l, \mathbf{k}', l') = -\delta_{l', l} \mathbf{k}' + (\mathbf{k} + P_l^0) \cap (\mathbf{k}' + P_{-l}^0)$$
(18)

and the operator

$$D(\delta\theta) = R_{\delta\theta/2} - R_{-\delta\theta/2} = 2\sin(\delta\theta/2)R_{\pi/2}.$$
 (19)

Let $\mathbf{k} \in \mathbb{R}^2$, $l \in \{+, -\}$, and define $\mathbf{k}_0 = R_{l\delta\theta/2}\mathbf{k}$. Then for any pair (\mathbf{k}', l') with $d(\mathbf{k}, l, \mathbf{k}', l') < \infty$, there are unique vectors $\mathbf{k}'_0 \in \mathbf{k}_0 + P^0_+ P^0_+$ and $\mathbf{Q} \in \mathcal{Q}(\mathbf{k}_0, l, \mathbf{k}'_0, l')$ such that

$$\mathbf{k}' = R_{-l'\delta\theta/2}\mathbf{k}_0' - lD(\delta\theta)\mathbf{Q}.$$
 (20)

Additionally, we have $|\mathbf{Q}| = d(\mathbf{k}, l, \mathbf{k}', l')$ so that

$$|R_{l'\delta\theta/2}\mathbf{k}' - \mathbf{k}_0'| = 2|\sin(\delta\theta/2)|d(\mathbf{k}, l, \mathbf{k}', l'). \tag{21}$$

Conversely, if \mathbf{k}' is given by Eq. (20) for some $\mathbf{k}'_0 \in \mathbf{k}_0 + P^0_- + P^0_+$ and $\mathbf{Q} \in \mathcal{Q}(\mathbf{k}_0, l, \mathbf{k}'_0, l')$ then $d(\mathbf{k}, l, \mathbf{k}', l') = |\mathbf{Q}|$. These claims are proved in Appendix G.

Since monolayer graphene has Dirac cones at the **K** and **K**' points (i.e., graphene has two valleys), the single-particle physics of H near the Fermi level at charge neutrality is dominated by Bloch states with crystal momenta near \mathbf{K}_{\pm} or \mathbf{K}'_{\pm} . Consider two momenta $\mathbf{k} = \mathbf{K}_l$, $\mathbf{k}' = \mathbf{K}'_{l'}$ from opposite graphene valleys. Then $\mathbf{k}_0 = \mathbf{K}_l^0$ and $R_{l'8\theta/2}\mathbf{k}' = \mathbf{K}'_{l'}^0$ where $\mathbf{K}_{\pm}^0 = R_{\mp\theta_0/2}\mathbf{K}$ and $\mathbf{K}''_{\pm} = R_{\mp\theta_0/2}\mathbf{K}'$. By Eqs. (12) and (14), $\mathbf{K}''_{l'} \notin \mathbf{K}_l^0 + P_-^0 + P_+^0$ so there is some minimal value $\kappa > 0$ taken by the quantity $|\mathbf{K}''_{l'} - \mathbf{k}'_0|$ for $\mathbf{k}'_0 \in \mathbf{k}_0 + P_-^0 + P_+^0$. By Eq. (21),

$$d(\mathbf{K}_{l}, l, \mathbf{K}'_{l'}, l') \geqslant \frac{\kappa}{2|\sin(\delta\theta/2)|},\tag{22}$$

which diverges as $\delta\theta \to 0$. This implies that for small $\delta\theta$, the spectrum of H splits into two nearly uncoupled valleys corresponding to \mathbf{K} and \mathbf{K}' . We will neglect intervalley coupling and focus on the \mathbf{K} valley, noting that time-reversal symmetry interchanges the valleys (see Appendix I).

For any q > 0, define $U(\mathbf{k}, l, q)$ to be the subspace generated by all Bloch states $|\mathbf{k}', l', \alpha'\rangle$ with $d(\mathbf{k}, l, \mathbf{k}', l') < q$, and note that $U(\mathbf{k}, l, q)$ is finite dimensional. To compute the eigenstates and energies of H in the \mathbf{K} valley, we consider the projection of H into $U(\mathbf{K}_l + \mathbf{p}, l, q)$ for a small vector \mathbf{p} and a large value q. Let $B_{l,q}$ be the set of pairs (\mathbf{k}', l') such that \mathbf{k}' is given by Eq. (20) with $\mathbf{k} = \mathbf{K}_l$, $\mathbf{k}'_0 \in \mathrm{BZ}_l^0 = R_{-l'\theta_0/2}\mathrm{BZ}$, and $|\mathbf{Q}| < q$. Then for all vectors \mathbf{p} small enough, the set of Bloch states $|\mathbf{k}' + \mathbf{p}, l', \alpha'\rangle$ with $(\mathbf{k}', l') \in B_{l,q}$ forms a basis for $U(\mathbf{K}_l + \mathbf{p}, l, q)$. The set $B_{l,q}$ is illustrated in Fig. 3(b).

Recall from Sec. II B that we can write $L_-^0 \cap L_+^0 = \sqrt{N}L$ and $P_-^0 + P_+^0 = P/\sqrt{N}$ where 4N is the number of atoms in the primitive unit cell of $L_-^0 \cap L_+^0$. When N>1 and q is large enough, there are elements $(\mathbf{k}',l') \in B_{l,q}$ for which the value of \mathbf{k}'_0 is not \mathbf{K}'_0 [e.g., the points shown in Fig. 3(b)]. The corresponding Bloch states in $U(\mathbf{K}_l + \mathbf{p}, l, q)$ have expected energies with respect to the intralayer Hamiltonian that are far from the Fermi level at charge neutrality. Assuming that $|\hat{\imath}_-(\mathbf{K})|$ is not too large, these Bloch states can be treated perturbatively. There is then some effective Hamiltonian supported only on the subspace generated by Bloch states $|\mathbf{k}' + \mathbf{p}, l', \alpha'\rangle$ such that $(\mathbf{k}', l') \in B_{l,q}$ and the value

¹Technically, *d* is not a metric because it assumes the value ∞ and $d(\mathbf{k}, l, \mathbf{k}', l') = 0$ whenever $l' = -l, \mathbf{k} \in P_l, \mathbf{k}' \in P_{-l}$ or $l' = l, \mathbf{k}' - \mathbf{k} \in P_l$. Nonetheless, it is useful to think of *d* as a distance function.

of \mathbf{k}'_0 is $\mathbf{K}''_{l'}$. Note that these conditions are equivalent to $\mathbf{k}' + \mathbf{p} = \mathbf{K}_{l'} + \mathbf{p}'$, where

$$\mathbf{p}' = \mathbf{p} - lD(\delta\theta)\mathbf{Q} \tag{23}$$

and $\mathbf{Q} \in \mathcal{Q}(\mathbf{K}_l^0, l, \mathbf{K}_{l'}^0, l')$ with $|\mathbf{Q}| < q$. For convenience, we define

$$Q_{+} = Q(\mathbf{K}_{+}^{0}, +, \mathbf{K}_{-}^{0}, -)$$

$$= Q(\mathbf{K}_{-}^{0}, -, \mathbf{K}_{+}^{0}, +)$$

$$= (\mathbf{K}_{-}^{0} + P_{-}^{0}) \cap (\mathbf{K}_{+}^{0} + P_{+}^{0}),$$
(24)

$$Q_{-} = -Q_{+}, \tag{25}$$

$$Q_{0} = Q(\mathbf{K}_{+}^{0}, +, \mathbf{K}_{+}^{0}, +)$$

$$= Q(\mathbf{K}_{-}^{0}, -, \mathbf{K}_{-}^{0}, -)$$

$$= P_{-}^{0} \cap P_{+}^{0}.$$
(26)

We will now describe a class of continuum models that approximate these effective Hamiltonians. We introduce continuum states $|\mathbf{p}, l, \alpha\rangle_c$ for $\mathbf{p} \in \mathbb{R}^2$, $l \in \{+, -\}$, $\alpha \in \{A, B\}$ in a new Hilbert space, satisfying the normalization condition

$$\langle \mathbf{p}', l', \alpha' |_{c} \mathbf{p}, l, \alpha \rangle_{c} = \delta_{l',l} \delta_{\alpha',\alpha} \delta^{2} (\mathbf{p}' - \mathbf{p}).$$
 (27)

Although **p** is allowed to range over all of \mathbb{R}^2 , $|\mathbf{p}, l, \alpha\rangle_c$ represents the Bloch state $|\mathbf{K}_l + \mathbf{p}, l, \alpha\rangle$ when **p** is small. When **p** is large, these states cannot be identified because they satisfy different normalization conditions, namely Eqs. (4) and (27). Because of Eq. (7), we take the part of the continuum Hamiltonian due to intralayer coupling to be $\tilde{H}_{intra} = \int d^2\mathbf{p}|\mathbf{p}\rangle_c \mathcal{H}_{intra}(\mathbf{p})\langle\mathbf{p}|_c$, where

$$\mathcal{H}_{intra}(\mathbf{p}) = \hbar v_F \begin{pmatrix} \boldsymbol{\sigma}_{\theta/2} \cdot \mathbf{p} & 0\\ 0 & \boldsymbol{\sigma}_{-\theta/2} \cdot \mathbf{p} \end{pmatrix}$$
(28)

and

$$|\mathbf{p}\rangle_c = (|\mathbf{p}, +, A\rangle_c \quad |\mathbf{p}, +, B\rangle_c \quad |\mathbf{p}, -, A\rangle_c \quad |\mathbf{p}, -, B\rangle_c)$$
(29)

is a row vector of states. Because of Eq. (23), we take the part of the continuum Hamiltonian due to interlayer coupling to be $\tilde{H}_{inter} = \int d^2 \mathbf{p}' d^2 \mathbf{p} |\mathbf{p}'\rangle_c \mathcal{H}_{inter}(\mathbf{p}', \mathbf{p}) \langle \mathbf{p}|_c$, where

$$\mathcal{H}_{inter}(\mathbf{p}', \mathbf{p})$$

$$= \sum_{\mathbf{Q} \in \mathcal{Q}_{0}} {S_{\mathbf{Q}}^{+} \choose 0} \delta^{2}(\mathbf{p}' - \mathbf{p} - D(\delta\theta)\mathbf{Q})$$

$$+ \sum_{\mathbf{Q} \in \mathcal{Q}_{+}} {0 \choose 0} \delta^{2}(\mathbf{p}' - \mathbf{p} - D(\delta\theta)\mathbf{Q})$$

$$+ \sum_{\mathbf{Q} \in \mathcal{Q}_{-}} {0 \choose T_{\mathbf{Q}} \choose 0} \delta^{2}(\mathbf{p}' - \mathbf{p} - D(\delta\theta)\mathbf{Q}). \quad (30)$$

Here, $T_{\mathbf{Q}}$ and $S_{\mathbf{Q}}^{l}$ denote complex 2×2 matrices, which are functions of $\delta\theta$ and the translation parameter **d**. Note that since \tilde{H}_{inter} is Hermitian, we have

$$T_{\mathbf{Q}}^{\dagger} = T_{-\mathbf{Q}}, \quad \left(S_{\mathbf{Q}}^{l}\right)^{\dagger} = S_{\mathbf{Q}}^{l}.$$
 (31)

The full continuum Hamiltonian is given by $\tilde{H} = \tilde{H}_{\text{intra}} + \tilde{H}_{\text{inter}}$.

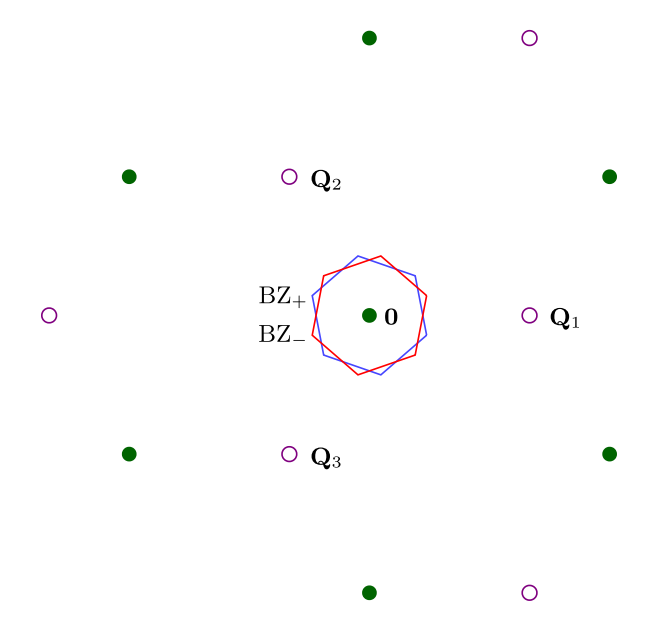


FIG. 4. The Q_+ and Q_0 lattices for the commensurate configuration with (m, n) = (5, 3), in which case s = 1. The elements of Q_+ (Q_0) are denoted by purple circles (green dots) and the elements of both lattices with minimal norm are labeled. The top (bottom) Brillouin zone boundaries are shown in blue (red).

We show in Appendix D 5 that

$$Q_{+} = s\sqrt{N}\mathbf{K} + \sqrt{N}P,$$

$$Q_{0} = \sqrt{N}P,$$
(32)

where $s = \pm 1$ is given by Eq. (D43). Furthermore, the elements of Q_+ with minimal norm are

$$\mathbf{Q}_1 = s\sqrt{N}\mathbf{K}, \quad \mathbf{Q}_2 = R_{2\pi/3}\mathbf{Q}_1, \quad \mathbf{Q}_3 = R_{4\pi/3}\mathbf{Q}_1.$$
 (33)

The lattices Q_+ and Q_0 and the vectors \mathbf{Q}_1 , \mathbf{Q}_2 , and \mathbf{Q}_3 are shown in Fig. 4.

We now observe that \tilde{H} is block diagonal: the states $|\mathbf{p}',l',\alpha'\rangle_c$ and $|\mathbf{p},l,\alpha\rangle_c$ are in the same Hamiltonian block if and only if

$$(\mathbf{p}' + l'\mathbf{q}_1) - (\mathbf{p} + l\mathbf{q}_1) \in D(\delta\theta)\mathcal{Q}_0, \tag{34}$$

where

$$\mathbf{q}_j = D(\delta\theta)\mathbf{Q}_j \quad \text{for } j \in \{1, 2, 3\}. \tag{35}$$

More explicitly, we have

$$\mathbf{q}_1 = 2\sin(\delta\theta/2)s\sqrt{N}|\mathbf{K}|\hat{\mathbf{y}},$$

$$\mathbf{q}_2 = R_{2\pi/3}\mathbf{q}_1, \quad \mathbf{q}_3 = R_{4\pi/3}\mathbf{q}_1.$$
 (36)

We refer to $D(\delta\theta)Q_0$ as the moiré reciprocal lattice and $\mathbf{p} + l\mathbf{q}_1$ as the moiré quasimomentum for $|\mathbf{p}, l, \alpha\rangle_c$. The Wigner-Seitz unit cell of the moiré reciprocal lattice is $\mathrm{BZ}_M = D(\delta\theta)\sqrt{N}\mathrm{BZ}$ and it is called the moiré Brillouin zone. Additionally, we define the high-symmetry moiré quasimomenta

$$\mathbf{X}_{M} = D(\delta\theta)s\sqrt{N}\mathbf{X} \tag{37}$$

for $X \in \{\Gamma, K, K', M\}$ and note that

$$\Gamma_M = \mathbf{0}, \quad \mathbf{K}_M = \mathbf{q}_1, \tag{38}$$

and

$$|\mathbf{K}_{M}| = 2|\sin(\delta\theta/2)|\sqrt{N}|\mathbf{K}|. \tag{39}$$

To further explicate the moiré translation symmetry, we transform to real space. We define states

$$|\mathbf{r}, l, \alpha\rangle_c = \frac{1}{2\pi} \int d^2 \mathbf{p} e^{-i\mathbf{p}\cdot\mathbf{r}} |\mathbf{p}, l, \alpha\rangle_c,$$
 (40)

which satisfy the normalization condition

$$\langle \mathbf{r}', l', \alpha'|_{c} \mathbf{r}, l, \alpha \rangle_{c} = \delta_{l',l} \delta_{\alpha',\alpha} \delta^{2} (\mathbf{r}' - \mathbf{r}).$$
 (41)

Defining the row vector of states

$$|\mathbf{r}\rangle_c = (|\mathbf{r}, +, A\rangle_c \quad |\mathbf{r}, +, B\rangle_c \quad |\mathbf{r}, -, A\rangle_c \quad |\mathbf{r}, -, B\rangle_c),$$
(42)

we can rewrite the Hamiltonian in the form $\tilde{H}_{\text{intra}} = \int d^2 \mathbf{r} |\mathbf{r}\rangle_c \mathcal{H}_{\text{intra}}(\mathbf{r}) \langle \mathbf{r}|_c$ and $\tilde{H}_{\text{inter}} = \int d^2 \mathbf{r} |\mathbf{r}\rangle_c \mathcal{H}_{\text{inter}}(\mathbf{r}) \langle \mathbf{r}|_c$, where

$$\mathcal{H}_{intra}(\mathbf{r}) = -i\hbar v_F \begin{pmatrix} \sigma_{\theta/2} \cdot \nabla & 0\\ 0 & \sigma_{-\theta/2} \cdot \nabla \end{pmatrix},$$

$$\mathcal{H}_{inter}(\mathbf{r}) = \begin{pmatrix} S^+(\mathbf{r}) & T(\mathbf{r})\\ T^{\dagger}(\mathbf{r}) & S^-(\mathbf{r}) \end{pmatrix}, \tag{43}$$

and

$$T(\mathbf{r}) = \sum_{\mathbf{Q} \in \mathcal{Q}_{+}} T_{\mathbf{Q}} e^{i\mathbf{r} \cdot D(\delta\theta)\mathbf{Q}},$$

$$S^{l}(\mathbf{r}) = \sum_{\mathbf{Q} \in \mathcal{Q}_{0}} S^{l}_{\mathbf{Q}} e^{i\mathbf{r} \cdot D(\delta\theta)\mathbf{Q}}.$$
(44)

We interpret \tilde{H} as the Hamiltonian for a system of Dirac electrons moving through the spatially varying potentials $T(\mathbf{r})$, $S^+(\mathbf{r})$, and $S^-(\mathbf{r})$. Note that these potentials are periodic (up to a phase) with respect to the moiré superlattice $D(\delta\theta)^{-1}L/\sqrt{N}$, which is reciprocal to $D(\delta\theta)Q_0$.

E. Continuum model for commensurate configurations

As in Sec. IID we take $\theta = \theta_0 + \delta\theta$, where θ_0 is a commensurate twist angle, $\delta\theta$ is small, and θ is an incommensurate angle. Since the microscopic Hamiltonian is continuous with respect to twist angle, we can take the limit $\delta\theta \to 0$ to derive a continuum model for the commensurate configuration with twist angle θ_0 .

In this section, we use $T_{\mathbf{Q}}(\delta\theta, \mathbf{d})$, $S_{\mathbf{Q}}^{l}(\delta\theta, \mathbf{d})$, $T(\mathbf{r}, \delta\theta, \mathbf{d})$, and $S^{l}(\mathbf{r}, \delta\theta, \mathbf{d})$, to denote the $T_{\mathbf{Q}}$ and $S_{\mathbf{Q}}^{l}$ matrices and the $T(\mathbf{r})$ and $S^{l}(\mathbf{r})$ potentials with twist angle $\theta = \theta_{0} + \delta\theta$ and translation vector \mathbf{d} . To determine the correct definition of $T_{\mathbf{Q}}(\mathbf{0}, \mathbf{d})$, note that

$$R_{-l\delta\theta/2}\mathbf{r} = \mathbf{r} - l\delta\theta R_{\pi/2}\mathbf{r}/2 + O(\delta\theta^2)$$
$$= \mathbf{r} - lD(\delta\theta)\mathbf{r}/2 + O(\delta\theta^2). \tag{45}$$

This implies that the pattern of atoms near position ${\bf r}$ with $\theta=\theta_0+\delta\theta$ and ${\bf d}={\bf 0}$ is the same to first order in $\delta\theta$ as the pattern with $\theta=\theta_0$ and

$$\mathbf{d} = D(\delta\theta)\mathbf{r} = 2\sin(\delta\theta/2)R_{\pi/2}\mathbf{r}.$$
 (46)

Taking into account the phase shift accrued by the continuum momentum states when the translation vector \mathbf{d} is changed

(see Appendix H), we must then have

$$e^{i\cos(\theta/2)\mathbf{K}\cdot D(\delta\theta)\mathbf{r}}T(\mathbf{r},\delta\theta,\mathbf{0})$$

$$= T(\mathbf{r},0,D(\delta\theta)\mathbf{r}) + O(\delta\theta^2)$$
(47)

and

$$S^{l}(\mathbf{r}, \delta\theta, \mathbf{0}) = S^{l}(\mathbf{r}, 0, D(\delta\theta)\mathbf{r}) + O(\delta\theta^{2}). \tag{48}$$

It follows that

$$e^{i\cos(\theta/2)\mathbf{K}\cdot D(\delta\theta)\mathbf{r}}\sum_{\mathbf{Q}\in\mathcal{Q}_{+}}T_{\mathbf{Q}}(\delta\theta,\mathbf{0})e^{i\mathbf{r}\cdot D(\delta\theta)\mathbf{Q}}$$

$$= \sum_{\mathbf{Q} \in \mathcal{Q}_{+}} T_{\mathbf{Q}}(0, D(\delta\theta)\mathbf{r}) + O(\delta\theta^{2})$$
 (49)

and

$$\sum_{\mathbf{Q} \in \mathcal{Q}_{0}} S_{\mathbf{Q}}^{l}(\delta\theta, \mathbf{0}) e^{i\mathbf{r} \cdot D(\delta\theta)\mathbf{Q}}$$

$$= \sum_{\mathbf{Q} \in \mathcal{Q}_{0}} S_{\mathbf{Q}}^{l}(0, D(\delta\theta)\mathbf{r}) + O(\delta\theta^{2}). \tag{50}$$

Taking $\mathbf{r} = D(\delta\theta)^{-1}\mathbf{d}$ and then taking the limit as $\delta\theta \to 0$ with \mathbf{d} fixed, we find

$$\sum_{\mathbf{Q}\in\mathcal{Q}_{+}} T_{\mathbf{Q}}(0,\mathbf{0}) e^{i\mathbf{d}\cdot(\cos(\theta_{0}/2)\mathbf{K}-\mathbf{Q})} = \sum_{\mathbf{Q}\in\mathcal{Q}_{+}} T_{\mathbf{Q}}(0,\mathbf{d})$$

$$\sum_{\mathbf{Q}\in\mathcal{Q}_{0}} S_{\mathbf{Q}}^{l}(0,\mathbf{0}) e^{-i\mathbf{d}\cdot\mathbf{Q}} = \sum_{\mathbf{Q}\in\mathcal{Q}_{0}} S_{\mathbf{Q}}^{l}(0,\mathbf{d}).$$
(51)

Taking $\delta\theta \to 0$ in Eq. (30) then gives $\mathcal{H}_{inter}(\mathbf{p}', \mathbf{p}) = \mathcal{H}_{inter}^0 \delta^2(\mathbf{p}' - \mathbf{p})$, where

$$\mathcal{H}_{\text{inter}}^{0} = \begin{pmatrix} S_0^+(\mathbf{d}) & T_0(\mathbf{d}) \\ T_0^+(\mathbf{d}) & S_0^-(\mathbf{d}) \end{pmatrix}$$
 (52)

and

$$T_{0}(\mathbf{d}) = \sum_{\mathbf{Q} \in \mathcal{Q}_{+}} T_{\mathbf{Q}}(0, \mathbf{0}) e^{i\mathbf{d} \cdot (\cos(\theta_{0}/2)\mathbf{K} - \mathbf{Q})},$$

$$S_{0}^{l}(\mathbf{d}) = \sum_{\mathbf{Q} \in \mathcal{Q}_{0}} S_{\mathbf{Q}}^{l}(0, \mathbf{0}) e^{-i\mathbf{d} \cdot \mathbf{Q}}.$$
(53)

We see that in the commensurate case, the continuum Hamiltonian describes four energy bands, approximating the bands nearest the Fermi level at charge neutrality.

Note that $T_0(\mathbf{d})$ and $S_0^I(\mathbf{d})$ are periodic (up to a phase) with respect to the lattice $L_-^0 + L_+^0 = L/\sqrt{N}$ which is reciprocal to \mathcal{Q}_0 (see Appendixes D 2 and D 5). As a result, for $\theta = \theta_0$ the continuum Hamiltonian \tilde{H} is periodic in \mathbf{d} (up to unitary equivalence) with respect to $L_-^0 + L_+^0$. It is worthwhile to note that the microscopic Hamiltonian H has the exact same periodicity in \mathbf{d} (see Appendix C).

III. SYMMETRY CONSTRAINTS AND MODEL PARAMETERS

We now consider the constraints that can be put on the TBG continuum model at twist angle $\theta = \theta_0 + \delta\theta$ based on the symmetries of TBG, and explicitly determine the parameters of the TBG continuum model near various commensurate angles.

Note that the continuum model is fully determined by the $T_{\mathbf{Q}}$ and $S_{\mathbf{Q}}^l$ matrices with $\mathbf{d}=\mathbf{0}$ in both the commensurate $(\delta\theta=0)$ and incommensurate $(\delta\theta\neq0)$ cases. We therefore make the assumption that $\mathbf{d}=\mathbf{0}$ throughout this section. For $\theta\neq0$, the valley preserving symmetries of the microscopic Hamiltonian H are generated by the unitary operators C_{3z} (rotation by $2\pi/3$ about $\mathbf{\hat{z}}$), C_{2x} (rotation by π about $\mathbf{\hat{x}}$), and the antiunitary operator $C_{2z}\mathcal{T}$ (time-reversal followed by rotation by π about $\mathbf{\hat{z}}$). The representations of these symmetry operators on the $|\mathbf{k}, l, \alpha\rangle$ and $|\mathbf{p}, l, \alpha\rangle_c$ states are given in Appendix I.

We require that \tilde{H} commutes with these symmetry operators. \tilde{H}_{intra} commutes with the symmetry operators identically so we need only consider \tilde{H}_{inter} . Assuming $\delta\theta \neq 0$, the symmetry constraint $[C_{2z}T, \tilde{H}_{\text{inter}}] = 0$ is equivalent to

$$\sigma_x \overline{T_{\mathbf{Q}}} \sigma_x = T_{\mathbf{Q}}, \quad \sigma_x \overline{S_{\mathbf{Q}}^l} \sigma_x = S_{\mathbf{Q}}^l,$$
 (54)

 $[C_{3z}, \tilde{H}_{inter}] = 0$ is equivalent to

$$e^{i(2\pi/3)\sigma_z} T_{\mathbf{Q}} e^{-i(2\pi/3)\sigma_z} = T_{R_{2\pi/3}\mathbf{Q}},$$

$$e^{i(2\pi/3)\sigma_z} S_{\mathbf{Q}}^l e^{-i(2\pi/3)\sigma_z} = S_{R_{2\pi/3}\mathbf{Q}}^l,$$
(55)

and $[C_{2x}, \tilde{H}_{inter}] = 0$ is equivalent to

$$\sigma_x T_{\mathbf{O}}^{\dagger} \sigma_x = T_{R^x \mathbf{Q}}, \quad \sigma_x S_{\mathbf{O}}^{-l} \sigma_x = S_{-R^x \mathbf{Q}}^{l},$$
 (56)

where we use the notation \overline{M} for the complex conjugate of a matrix M. By continuity, these equations also hold for $\delta\theta = 0$.

Since $\hat{t}_{-}(\mathbf{k})$ monotonically decreases with $|\mathbf{k}|$, we expect that the magnitudes of $T_{\mathbf{Q}}$ and $S_{\mathbf{Q}}^l$ decay rapidly with $|\mathbf{Q}|$. We therefore neglect $T_{\mathbf{Q}}$ and $S_{\mathbf{Q}}^l$ for all \mathbf{Q} with nonminimal norm. Recall that the elements of \mathcal{Q}_{+} of minimal norm are \mathbf{Q}_{1} , \mathbf{Q}_{2} , and \mathbf{Q}_{3} which are given in Eq. (33). The elements of \mathcal{Q}_{-} with minimal norm are $-\mathbf{Q}_{1}$, $-\mathbf{Q}_{2}$, and $-\mathbf{Q}_{3}$, and the only element of \mathcal{Q}_{0} of minimal norm is $\mathbf{0}$. See Fig. 4 for an illustration of the \mathbf{Q}_{1} , \mathbf{Q}_{2} , and \mathbf{Q}_{3} vectors.

By Eq. (31), it suffices to determine the matrices $T_{\mathbf{Q}_1}$, $T_{\mathbf{Q}_2}$, $T_{\mathbf{Q}_3}$, S_0^+ , S_0^- which correspond to minimal norm momenta. By expanding these matrices in the Pauli basis and applying Eqs. (54) to (56) we find

$$T_{\mathbf{Q}_{j}} = w_{0}e^{i\chi_{0}\sigma_{z}} + w_{1}(\sigma_{x}\cos\zeta_{j} + \sigma_{y}\sin\zeta_{j}),$$

$$S_{\mathbf{0}}^{+} = S_{\mathbf{0}}^{-} = w_{2}\sigma_{0}$$
(57)

for real model parameters χ_0 , w_0 , w_1 , and w_2 with $w_0 \geqslant 0$ and $\chi_0 \in [0, 2\pi)$. Here, we have used $\zeta_j = \frac{2\pi(j-1)}{3}$ for $j \in \{1, 2, 3\}$ and σ_0 for the 2×2 identity matrix. Note that the model parameters χ_0 , w_0 , w_1 , and w_2 depend on θ_0 and $\delta\theta$ but not on \mathbf{d} .

In the special case $\theta=0$ (i.e., no twist), there is an additional valley preserving unitary mirror symmetry M_y (reflection across the xz plane). The symmetry constraint $[M_y, \tilde{H}_{inter}] = 0$ is equivalent to

$$\sum_{\mathbf{Q}\in\mathcal{Q}_{+}} [T_{\mathbf{Q}}, \sigma_{x}] = \sum_{\mathbf{Q}\in\mathcal{Q}_{0}} \left[S_{\mathbf{Q}}^{l}, \sigma_{x} \right] = 0$$
 (58)

(see Appendix I). When $\theta = 0$, Eq. (58) implies $\chi_0 = 0$. Therefore, if the twist angle is near 0 (i.e., $\theta_0 = 0$, $\theta = \delta\theta \approx 0$) one will find $\chi_0 \approx 0$ because of the approximate M_{ν} sym-

metry. This agrees with the Bistritzer-MacDonald model for small angle TBG [3].

In Appendix J, we show that when $\delta\theta = 0$, the model parameters can be determined from numerical computations of the Hamiltonian block containing \mathbf{K}_{\pm} using Eqs. (6) and (9). Additionally, Appendixes D 6 and J show that the χ_0 , w_0 , and w_2 parameters determine the band structure of AA stacked commensurate configurations, while the w_1 and w_2 parameters determine the band structures of AB and BA stacked commensurate configurations. For numerical computations, we choose the $t_{+}(\mathbf{r})$ functions in Eq. (5) to be those used in Refs. [77,78,84] and described in Appendix K. Table I shows approximate values of the model parameters derived from these functions for the first six commensurate configurations in order of the number of atoms per unit cell. Appendix Table II lists these parameters with more significant figures. Appendix Fig. 15 shows that the continuum models with parameters in Appendix Table II are accurate low energy approximations of the microscopic Hamiltonian for all **d** vectors. Additionally, Appendix Fig. 16 compares the band structures for each commensurate configuration in Table I with the band structure derived from the microscopic Hamiltonian, and we see very good agreement. We note that we do not include any lattice relaxation or corrugation effects here in the microscopic model, nor do we include coupling mediated by higher graphene bands. Such effects may alter the true model parameters.

IV. COMMENSURATE MODELS: BAND STRUCTURES

By Eqs. (28), (52), and (53), the continuum model corresponding to commensurate twist angle θ_0 and translation vector \mathbf{d} is $\tilde{H} = \int d^2\mathbf{p} |\mathbf{p}\rangle_c \mathcal{H}_0(\mathbf{p}) \langle \mathbf{p}|_c$, where the explicit Hamiltonian matrix is

$$\mathcal{H}_0(\mathbf{p}) = w_2 I + \begin{pmatrix} \hbar v_F \boldsymbol{\sigma}_{\theta_0/2} \cdot \mathbf{p} & T_0(\mathbf{d}) \\ T_0^{\dagger}(\mathbf{d}) & \hbar v_F \boldsymbol{\sigma}_{-\theta_0/2} \cdot \mathbf{p} \end{pmatrix}, \quad (59)$$

$$T_0(\mathbf{d}) = \sum_{i=1}^{3} T_{\mathbf{Q}_j} e^{i\mathbf{d} \cdot (\cos(\theta_0/2)\mathbf{K} - \mathbf{Q}_j)}.$$
 (60)

The matrices $T_{\mathbf{Q}_j}$ are given in Eq. (57) and I is the 4 × 4 identity matrix. Recall that σ_{ϕ} is the Pauli matrix vector defined in Eq. (8), \mathbf{Q}_j is defined in Eq. (33), and the momentum space basis $|\mathbf{p}\rangle_c$ is defined in Eq. (29). Using Eqs. (43) and (44) we can also describe this model in real space as $\tilde{H} = \int d^2\mathbf{r}|\mathbf{r}\rangle_c \mathcal{H}_0(\mathbf{r})\langle\mathbf{r}|_c$, where the Hamiltonian matrix takes the form

$$\mathcal{H}_{0}(\mathbf{r}) = w_{2}I + \begin{pmatrix} -i\hbar v_{F}\boldsymbol{\sigma}_{\theta_{0}/2} \cdot \nabla & T_{0}(\mathbf{d}) \\ T_{0}^{\dagger}(\mathbf{d}) & -i\hbar v_{F}\boldsymbol{\sigma}_{-\theta_{0}/2} \cdot \nabla \end{pmatrix}$$
(61)

and the real space basis $|\mathbf{r}\rangle_c$ is defined in Eq. (42).

Figure 5 shows the low energy band structures of the model in Eqs. (59) and (60) for the first two commensurate configurations in Table I, namely (m,n)=(1,0) (the untwisted configuration with $\theta_0=0$) and (m,n)=(5,3) ($\theta_0\approx 38.2^\circ$). For both configurations, we show three translation vectors \mathbf{d} , and use the parameters in Appendix Table II. Similar band structures for the other commensurate configurations in Table I are shown in Appendix Fig. 16. We compare the band

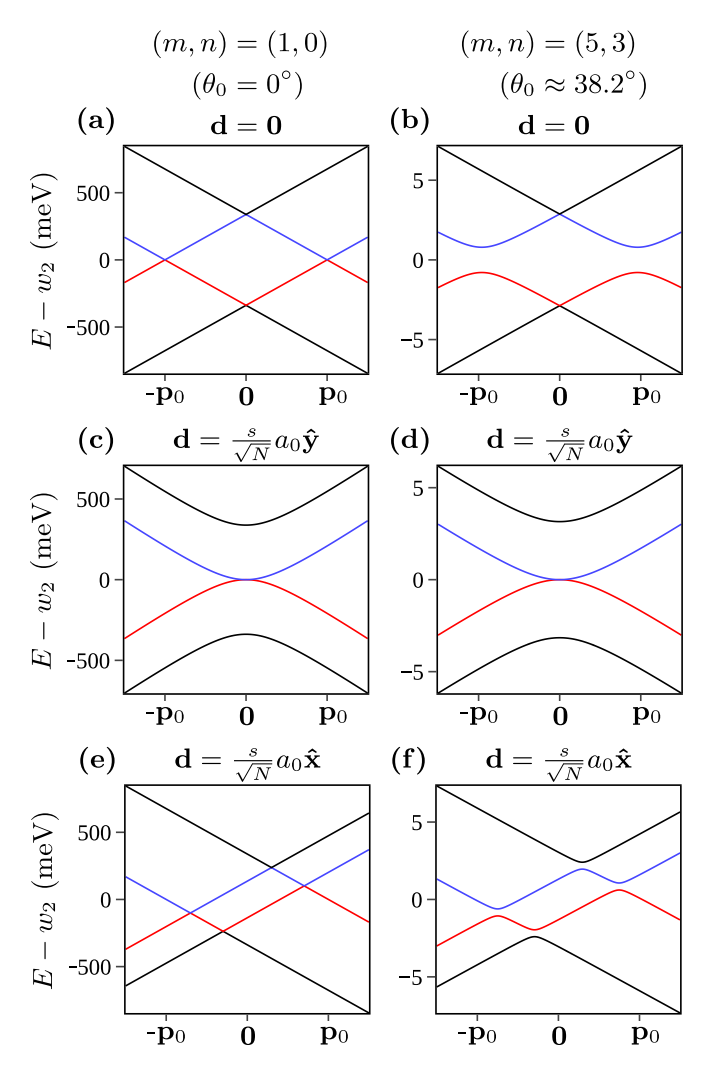


FIG. 5. Commensurate band structures using the model in Eqs. (59) and (60) with parameters in Appendix Table II. The vector \mathbf{p} ranges linearly from $-3\mathbf{p}_0/2$ to $3\mathbf{p}_0/2$, where $\hbar v_F \mathbf{p}_0 = 3|w_0|\hat{\mathbf{x}}$. The first and second columns correspond to commensurate configurations with (m,n)=(1,0) ($\theta_0=0^\circ$) and (m,n)=(5,3) ($\theta_0\approx38.2^\circ$), and the first and second rows correspond to AA and AB stackings, respectively (see Appendix D 6).

structures of untwisted bilayer graphene and commensurate TBG in the following cases.

(1) At AA stacking where $\mathbf{d} = \mathbf{0}$. In this case, untwisted bilayer graphene is gapless at momentum $|\mathbf{p}| = |\mathbf{p}_0| = 3|w_0|/(\hbar v_F)$ at charge neutrality as in Fig. 5(a). In contrast, commensurate TBG develops a gap at $|\mathbf{p}| = |\mathbf{p}_0|$ at charge neutrality as in Fig. 5(b), due to the relative rotation angle between the Dirac fermions in different layers and the nonzero value of χ_0 . Specifically, the gap at $|\mathbf{p}| = |\mathbf{p}_0|$ is given in general by

$$12|w_0|\min(|\cos(\phi_0/2)|, |\sin(\phi_0/2)|) \tag{62}$$

where $\phi_0 = \chi_0 + \theta_0/2$. In the $\theta_0 \approx 38.2^\circ$ commensurate configuration, the charge neutrality gap in Fig. 5(b) is approximately 1.6 meV, which should be experimentally measurable.

(2) At *AB* stacking where $\mathbf{d} = \frac{s}{\sqrt{N}} a_0 \hat{\mathbf{y}}$ (recall that $s = \pm 1$ was introduced in Eq. (32)). In this case, both untwisted

(Bernal) bilayer graphene, shown in Fig. 5(c), and commensurate TBG, shown in Fig. 5(d), have gapless quadratic Dirac band touchings [85] at charge neutrality.

(3) At generic asymmetric stackings such as $\mathbf{d} = \frac{s}{\sqrt{N}} a_0 \hat{\mathbf{x}}$. Untwisted bilayer graphene remains gapless as in Fig. 5(e). In contrast, commensurate TBG has a tilted band gap at charge neutrality as in Fig. 5(f), but there may not be an indirect gap.

Although the above observations are made at exactly commensurate angles, they may also hold for local measurements (e.g., scanning tunneling microscopy experiments) near the corresponding stackings if the angle θ is close enough to a commensurate angle θ_0 . In particular, when θ_0 is significantly far from zero, one expects to observe a local charge neutrality gap at AA stacking positions (e.g., a 1.6 meV gap at $\theta_0 \approx 38.2^{\circ}$). However, we note that the local charge neutrality at AA stacking is generically different from the global charge neutrality of an incommensurate angle, due to local charge transfers between AA stacking regions and AB stacking regions. This can be seen in Fig. 7(c), by noting that the moiré bands at global charge neutrality are close to the conduction band energy at AA stacking in Fig. 5(b).

V. CONTINUUM MODELS NEAR COMMENSURATION: MOIRÉ BAND STRUCTURES AND MAGIC ANGLES

The continuum model corresponding to twist angle $\theta = \theta_0 + \delta\theta$ and translation vector $\mathbf{d} = \mathbf{0}$ is described by Eqs. (28), (30), and (57). Note that when $\delta\theta \neq 0$, the microscopic Hamiltonians for different choices of translation vector \mathbf{d} differ only by a unitary transformation (see Appendix C) so it is sufficient to consider the case $\mathbf{d} = \mathbf{0}$. In this section, we further develop the continuum model Hamiltonian and investigate its moiré band structures and magic angles using the parameters determined in Sec. III.

Since $\delta\theta$ is small, we approximate the rotation angles $\pm\theta/2$ of the Dirac cones in Eq. (28) by $\pm\theta_0/2$. This is a common approximation in the literature [3]. Additionally, we approximate the χ_0 , w_0 , w_1 , and w_2 parameters by their values at angle θ_0 (i.e., with $\delta\theta=0$), which can be determined using the method described in Sec. III. The continuum model then becomes $\tilde{H}=\int d^2\mathbf{p}'d^2\mathbf{p}|\mathbf{p}'\rangle_c\mathcal{H}(\mathbf{p}',\mathbf{p})\langle\mathbf{p}|_c$, where the Hamiltonian matrix is

$$\mathcal{H}(\mathbf{p}', \mathbf{p}) = w_2 I \delta^2(\mathbf{p}' - \mathbf{p})$$

$$+ \hbar v_F \begin{pmatrix} \sigma_{\theta_0/2} \cdot \mathbf{p} & 0 \\ 0 & \sigma_{-\theta_0/2} \cdot \mathbf{p} \end{pmatrix} \delta^2(\mathbf{p}' - \mathbf{p})$$

$$+ \sum_{j=1}^3 \begin{pmatrix} 0 & T_{\mathbf{Q}_j} \\ 0 & 0 \end{pmatrix} \delta^2(\mathbf{p}' - \mathbf{p} - \mathbf{q}_j)$$

$$+ \sum_{j=1}^3 \begin{pmatrix} 0 & 0 \\ T_{\mathbf{Q}_j}^{\dagger} & 0 \end{pmatrix} \delta^2(\mathbf{p}' - \mathbf{p} + \mathbf{q}_j)$$
(63)

and the matrices $T_{\mathbf{Q}_j}$ are defined in Eq. (57). Recall that σ_{ϕ} is the Pauli matrix vector defined in Eq. (8), \mathbf{q}_j is defined in Eq. (35), and the momentum space basis $|\mathbf{p}\rangle_c$ is defined in Eq. (29). Note that w_2 only provides a constant energy shift.

Using Eqs. (43) and (44), we can also describe this model in real space by $\tilde{H} = \int d^2 \mathbf{r} |\mathbf{r}\rangle_c \mathcal{H}(\mathbf{r}) \langle \mathbf{r}|_c$, where

$$\mathcal{H}(\mathbf{r}) = w_2 I + \begin{pmatrix} -i\hbar v_F \sigma_{\theta_0/2} \cdot \nabla & T(\mathbf{r}) \\ T^{\dagger}(\mathbf{r}) & -i\hbar v_F \sigma_{-\theta_0/2} \cdot \nabla \end{pmatrix},$$

$$T(\mathbf{r}) = \sum_{j=1}^{3} T_{\mathbf{Q}_j} e^{i\mathbf{r} \cdot \mathbf{q}_j},$$
(64)

and the real space basis $|\mathbf{r}\rangle_c$ is defined in Eq. (42).

Following Refs. [3,12], we introduce the dimensionless parameter

$$\alpha = \frac{|w_1|}{\hbar v_F |\mathbf{K}_M|} = \frac{|w_1|}{2|\sin(\delta\theta/2)|\hbar v_F \sqrt{N}|\mathbf{K}|}.$$
 (65)

Recall that 4N is the number of atoms in each commensurate unit cell at twist angle θ_0 . Note that $\alpha^{-1} \propto |\delta\theta|$ when $\delta\theta$ is small.

As a first step in the search for magic angles, we cut off the continuum model in Eq. (63) to a subspace of four quasimomenta, namely \mathbf{p} and $\mathbf{p} - \mathbf{q}_j$ for $j \in \{1, 2, 3\}$. This truncation is known as the tripod model approximation [3,80] and it yields an approximate $\mathbf{k} \cdot \mathbf{p}$ model at the \mathbf{K}_M point at charge neutrality. Generically, the lowest bands of this model have a Dirac fermion spectrum with Fermi velocity v_M . In this tripod model approximation, it can be shown (see Appendix O) that the velocity v_M reaches its minimum (which is generically nonzero unless $\theta_0 = 0$) near

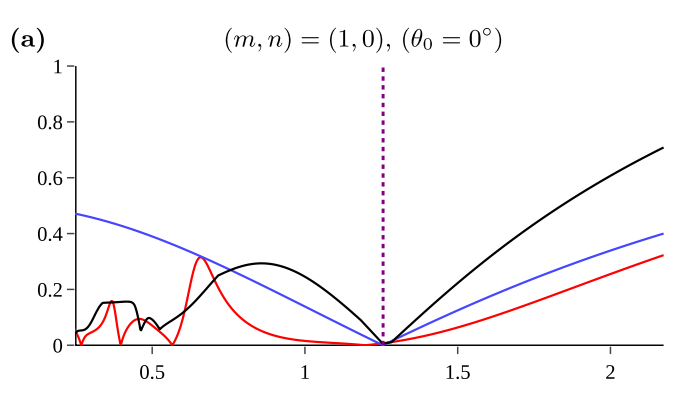
$$\alpha^{-1} \approx \sqrt{3},$$
 (66)

given that the energy E at the \mathbf{K}_M point satisfies $\frac{|E-w_2|}{\hbar v_F |\mathbf{K}_M|} \ll 1$. Note that the energy $E-w_2$ at the \mathbf{K}_M point is generically nonzero when θ_0 is nonzero. It is also known that the magic angle condition in Eq. (66) generically requires $w_0 \leqslant |w_1|$ to avoid hybridization with the remote bands [80], and this is also true here (see Fig. 19 for examples illustrating this point). By Eq. (65), we conclude that the first magic angle occurs at

$$\delta\theta = \delta\theta_{\text{magic}} \approx \pm \frac{\sqrt{3}w_1}{\hbar v_F \sqrt{N} |\mathbf{K}|}.$$
 (67)

The tripod model approximation, however, does not give the higher (i.e., second, third, etc.) magic angles.

Figures 6(a) and 6(b) show numerical results for Dirac velocities v_M and the bandwidth of the lowest two moiré bands at charge neutrality, near the commensurate configurations with $(m, n) = (1, 0) (\theta_0 = 0^\circ) \text{ and } (m, n) = (5, 3) (\theta_0 \approx 38.2^\circ),$ respectively. The blue curves show v_M/v_F values computed from the tripod model, and have a minimum around the angle in Eq. (67). The red curves show the accurate v_M/v_F values computed using 768 moiré bands (see Appendix M and Fig. 17). In both cases, the value of v_M/v_F is computed by numerical differentiation in the \mathbf{q}_1 direction at \mathbf{K}_M . Intriguingly, at $\theta_0 \approx 38.2^{\circ}$, the accurate Fermi velocity v_M at the first magic angle $\delta\theta_{\rm magic}$ is almost zero and much smaller than that found in the tripod model. The black curves show the total bandwidth (in units of $\hbar v_F |\mathbf{K}_M|$) of the lowest two bands at charge neutrality using 768 moiré bands. From the accurate v_M/v_F (red) and bandwidth (black) curves, we clearly see the



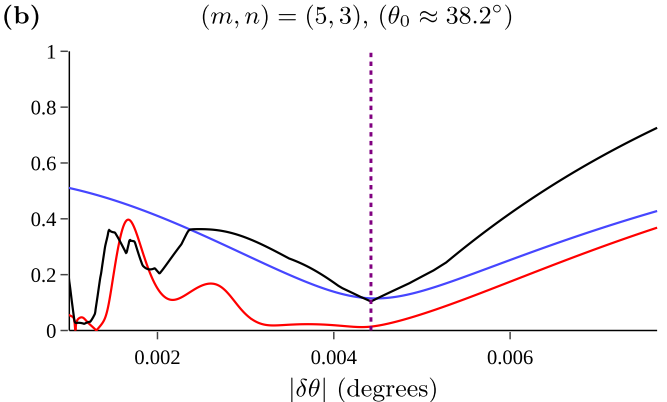


FIG. 6. The red, blue, and black curves show properties of the spectrum of the continuum Hamiltonian in Eq. (63) as a function of $\delta\theta$. The red and blue curves show v_M/v_F (v_M is the Dirac velocity at the \mathbf{K}_M point at charge neutrality), while the black curve shows the bandwidth (in units of $\hbar v_F |\mathbf{K}_M|$) of the two lowest bands at charge neutrality. The purple dashed lines indicate $\delta\theta = \delta\theta_{\text{magic}}$, at which point the bandwidth is minimized. The blue curves use the 8 band tripod model analyzed in Appendix O while the red and black curves use the more accurate 768 band model illustrated in Appendix Fig. 17. The bandwidth shown in the black curve is the difference between the highest conduction energy and the lowest valence energy among the points \mathbf{F}_M , \mathbf{K}_M , \mathbf{M}_M , $\mathbf{K}_M/2$, $\mathbf{M}_M/2$, $-\mathbf{M}_M/2$ in BZ_M. (a) and (b) correspond to the commensurate configurations with (m,n)=(1,0) ($\theta_0=0^\circ$) and (m,n)=(5,3) ($\theta_0\approx38.2^\circ$), respectively, and use the parameters in Appendix Table II.

first magic angle around the value in Eq. (67). There are higher (i.e., smaller) magic angles near $\theta_0 \approx 38.2^\circ$ as well, where the lowest two bands become flat.

Figures 7(a) and 7(c) show the moiré band structures at the first magic angle $\delta\theta = \delta\theta_{\rm magic}$ the commensurate configurations with (m,n)=(1,0) ($\theta_0=0^\circ$) and (m,n)=(5,3) ($\theta_0\approx 38.2^\circ$), respectively. The band structure with $\theta_0=0^\circ$ shows the usual magic angle moiré bands of small angle TBG studied in [3]. At $\theta_0\approx 38.2^\circ$, the band structure is clearly not symmetric across the Fermi level, indicating the absence of both particle-hole symmetry P [5,45,86] and chiral symmetry P [12] (see definitions in Appendix L). The lowest two moiré bands at charge neutrality are still approximately flat near the \mathbf{K}_M and $-\mathbf{K}_M$ points, and are energetically shifted close to a remote conduction band. The two bands are however not quite flat near the $\mathbf{\Gamma}_M$ point.

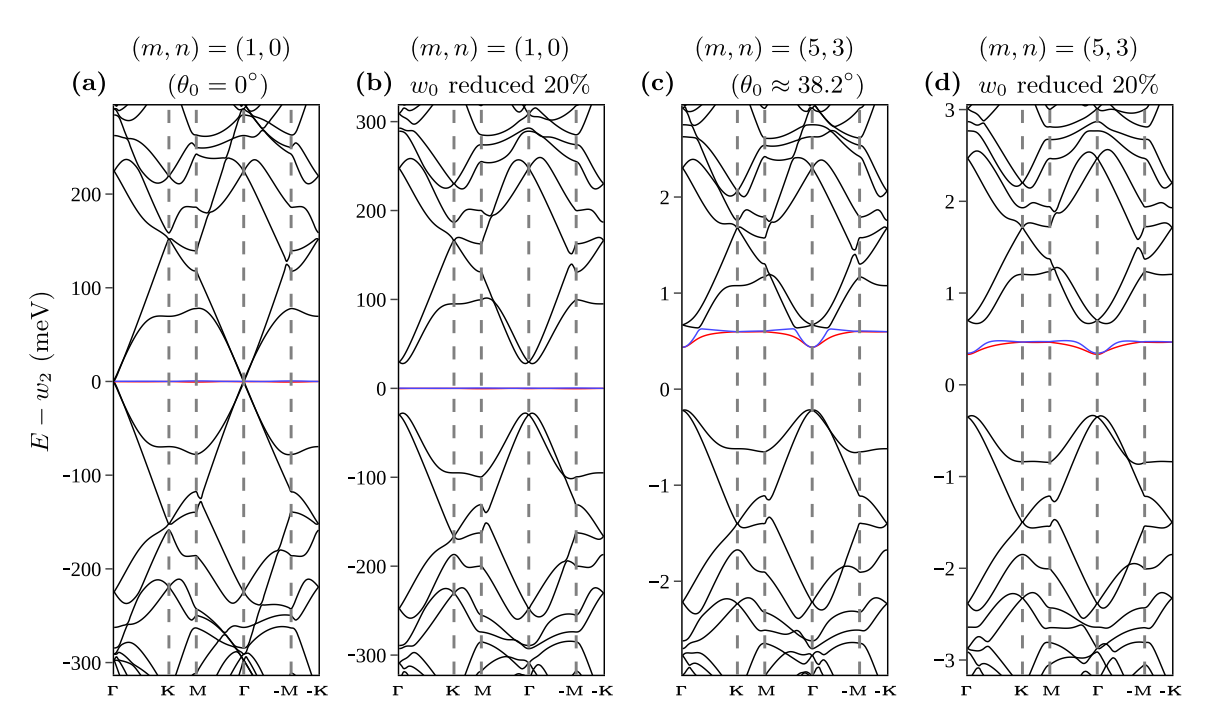


FIG. 7. Moiré band structures using the model in Eq. (63) with $\delta\theta = \theta - \theta_0 = \delta\theta_{\text{magic}}$ (where the bandwidth is minimal in Fig. 6) and the quasimomentum truncation illustrated in Appendix Fig. 17. The horizontal axes follow the moiré quasimomentum trajectory $\Gamma_M \to \mathbf{K}_M \to \mathbf{M}_M \to \mathbf{\Gamma}_M \to -\mathbf{M}_M \to -\mathbf{K}_M$. The two bands nearest charge neutrality are shown in blue and red while all other bands are shown in black. (a) and (b) correspond to the commensurate configurations with (m, n) = (1, 0) ($\theta_0 = 0^\circ$) and (m, n) = (5, 3) ($\theta_0 \approx 38.2^\circ$), respectively and use the parameters in Appendix Table II. The parameters for panels (b) and (d) are the same as those for (a) and (c) except with the values of w_0 reduced by 20%. Similar plots for the other commensurate configurations in Table I are shown in Appendix Fig. 18.

It is known that in small angle TBG, lattice relaxation has the effect of slightly reducing the value of w_0 [10,78,79]. Although we do not here consider relaxation from first principles, it is nonetheless worthwhile to consider the effect of a reduction in w_0 on the moiré band structure. Figures 7(b) and 7(d) show moiré band structures using the same parameters as in Fig. 7(a) and 7(c), but with w_0 reduced by 20%. In both cases, we see that the two lowest bands at charge neutrality develop a gap from the higher bands, but are otherwise qualitatively similar. Moiré band structures at the first magic angle in Eq. (67) near the other commensurate configurations listed in Table I are shown in Appendix Fig. 18. Additionally, other example moiré band structures near the first magic angle can be found in Figs. 10 and 19.

Appendix Table II shows the values of $\delta\theta_{\rm magic}$ for the first six commensurate configurations. Due to the small magnitude of w_0 and w_1 for nonzero commensurate angles, the corresponding values of $\delta\theta_{\rm magic}$ are so small that they likely cannot be achieved experimentally. However, we note the possibility that atomic structural reconstructions (e.g., charge density wave orders) may occur in large twist angle TBG and enhance the effective interlayer hoppings w_0 and w_1 . Additionally, lattice relaxation or corrugation or couplings mediated by higher graphene bands could also change these parameters. Provided these perturbations do not break the symmetries of the moiré superlattice (translation, C_{3z} , $C_{2z}\mathcal{T}$, and C_{2x}), the form of effective continuum model will not change, and we may arrive at larger first magic angles in nearly commensurate TBG.

VI. FLAT BANDS IN THE CONTINUUM MODEL PARAMETER SPACE: THE HYPERMAGIC REGIME

Regarding the possibility that the actual model parameters may change due to atomic structural reconstruction, lattice relaxation or corrugation, or couplings mediated by higher graphene bands, we now investigate the band structure of the TBG continuum model near commensuration in Eq. (63) with arbitrary parameters. We reveal the existence of a remarkable hypermagic regime centered at $\phi_0 = \pm \pi/2$ where many moiré bands (often 8 or more) become extremely flat simultaneously.

A. Model simplification

We first simplify the continuum model in Eq. (63) by applying a unitary transformation of the basis from $|\mathbf{p}\rangle_c$ to $|\mathbf{p}\rangle_c' = |\mathbf{p}\rangle_c U_{\theta_0}$, where

$$U_{\theta_0} = \begin{pmatrix} e^{-i(\theta_0/4)\sigma_z} & 0\\ 0 & e^{i(\theta_0/4)\sigma_z} \end{pmatrix}. \tag{68}$$

Such a transformation removes the rotation angles $\pm \theta_0/2$ for the Dirac cones, and transforms the Hamiltonian into $\tilde{H} = \int d^2 \mathbf{p}' d^2 \mathbf{p} |\mathbf{p}'\rangle_c' \mathcal{H}'(\mathbf{p}',\mathbf{p})\langle \mathbf{p}|_c'$, where the Hamiltonian matrix is given by

$$\mathcal{H}'(\mathbf{p}', \mathbf{p}) = w_2 I \delta^2(\mathbf{p}' - \mathbf{p}) + \hbar v_F \begin{pmatrix} \boldsymbol{\sigma} \cdot \mathbf{p} & 0 \\ 0 & \boldsymbol{\sigma} \cdot \mathbf{p} \end{pmatrix} \delta^2(\mathbf{p}' - \mathbf{p})$$

$$+\sum_{j=1}^{3} \begin{pmatrix} 0 & T'_{\mathbf{Q}_j} \\ 0 & 0 \end{pmatrix} \delta^2(\mathbf{p}' - \mathbf{p} - \mathbf{q}_j)$$

$$+\sum_{i=1}^{3} \begin{pmatrix} 0 & 0 \\ T_{\mathbf{Q}_{j}}^{\prime\dagger} & 0 \end{pmatrix} \delta^{2}(\mathbf{p}' - \mathbf{p} + \mathbf{q}_{j}). \quad (69)$$

Here, $\boldsymbol{\sigma} = \sigma_x \mathbf{\hat{x}} + \sigma_y \mathbf{\hat{y}}$ is a vector of Pauli matrices, and

$$T_{\mathbf{Q}_{i}}' = e^{i(\theta_{0}/4)\sigma_{z}} T_{\mathbf{Q}_{i}} e^{i(\theta_{0}/4)\sigma_{z}}.$$
 (70)

More explicitly,

$$T'_{\mathbf{Q}_j} = w_0 e^{i\phi_0 \sigma_z} + w_1(\sigma_x \cos \zeta_j + \sigma_y \sin \zeta_j), \qquad (71)$$

where $\zeta_j = \frac{2\pi(j-1)}{3}$ for $j \in \{1, 2, 3\}$, and we have defined

$$\phi_0 = \chi_0 + \frac{\theta_0}{2}.\tag{72}$$

This implies that the angles χ_0 and θ_0 do not have fully independent effects on the band structure. We are left with a single angle variable ϕ_0 in the continuum model of Eq. (69), occurring in the matrices T'_{Q_j} in Eq. (71). We note that the angle ϕ_0 in Eq. (72) also occurs in the expression for the energy gap in the commensurate AA stacking configuration in Eq. (62). This can also be understood via the transformation in Eq. (68).

The model can similarly be written in the transformed real space basis

$$|\mathbf{r}\rangle_c' = |\mathbf{r}\rangle_c U_{\theta_0}. \tag{73}$$

The Hamiltonian then becomes $\tilde{H} = \int d^2 \mathbf{r} |\mathbf{r}\rangle_c' \mathcal{H}'(\mathbf{r}) \langle \mathbf{r}|_c'$, where the Hamiltonian matrix is given by

$$\mathcal{H}'(\mathbf{r}) = w_2 I + \begin{pmatrix} -i\hbar v_F \boldsymbol{\sigma} \cdot \nabla & T'(\mathbf{r}) \\ T'^{\dagger}(\mathbf{r}) & -i\hbar v_F \boldsymbol{\sigma} \cdot \nabla \end{pmatrix}, \tag{74}$$

and where we have defined

$$T'(\mathbf{r}) = \sum_{i=1}^{3} T'_{\mathbf{Q}_{j}} e^{i\mathbf{r}\cdot\mathbf{q}_{j}}$$
 (75)

in terms of the matrices $T'_{\mathbf{O}_i}$ in Eq. (71).

By the results of Appendix L, we can assume without loss of generality that s = 1 [recall that s affects the direction of \mathbf{q}_j , see Eqs. (33) and (35)], and

$$\phi_0 \in \left[0, \frac{\pi}{2}\right], \quad w_0 \geqslant 0, \quad w_1 \geqslant 0, \quad \delta\theta \geqslant 0.$$
 (76)

In addition, since w_2 simply shifts the energy bands globally, we assume $w_2=0$ hereafter. As shown in Appendix L, the moiré band structures at angle ϕ_0 and angle $-\phi_0$ are particle-hole transformations of each other, while the moiré band structures at angle ϕ_0 and angle $\pi-\phi_0$ are equivalent.

We note that in the chiral limit $w_0 = 0$ [12], the continuum model in Eq. (69) is independent of the angle ϕ_0 . This is revealed as a symmetry of the TBG continuum model in the chiral limit in Ref. [14].

B. Changing ϕ_0 in the first magic manifold

We first describe the evolution of the flat bands with respect to the angle variable ϕ_0 defined in Eq. (72) with the magic

angle criteria $\alpha^{-1} \approx \sqrt{3}$ and $0 \leqslant w_0/w_1 \leqslant 1$ [see Eq. (66)]. Following Ref. [80], we refer to the parameter space satisfying these conditions and minimizing the bandwidth of the lowest two bands at charge neutrality as the *first magic manifold*.

Figure 8 contains three heat maps showing the base 10 logarithm of the bandwidth (in units of $\hbar v_F |\mathbf{K}_M|$) of the two lowest bands at charge neutrality. The first magic manifold appears in Fig. 8(b) (where $\phi_0 = 0$) as a dark nearly horizontal curve on the left of the plot. In the first magic manifold with $\phi_0 = 0$, the lowest two flat bands at charge neutrality are symmetric about zero energy due to an anticommuting particle-hole symmetry P defined in Appendix L [5]. Band structures for parameters in the first magic manifold with $\phi_0 = 0$ can be found in Fig. 7(a), 7(b), and 10(a).

For a fixed w_0/w_1 and with $\alpha^{-1} \approx \sqrt{3}$, tuning ϕ_0 away from 0 shifts the two flat bands at charge neutrality away from zero energy (breaking the particle-hole symmetry P), and gradually increases the bandwidth of the flat bands. As shown in Fig. 8(a), the bandwidth around $\alpha^{-1} = \sqrt{3}$ increases as ϕ_0 increases from 0 to $\pi/2$, but still shows a local minimum near $\alpha^{-1} = \sqrt{3}$. The precise value of α^{-1} that minimizes the bandwidth decreases as ϕ_0 increases. The increase of the bandwidth is mostly due to band curvature at the Γ_M point. This can be seen in Figs. 7(c), 7(d), and 10(b)–10(d). In particular, the lowest two bands at charge neutrality remain quite flat near the K_M and $-K_M$ points in the first magic manifold for small ϕ_0 . See Appendix Figs. 18 and 19 for additional band structures in the first magic manifold.

Figures 11(a) and 11(b) show the real space wave functions at Γ_M corresponding to the flat bands in Figs. 10(a) and 10(b). We see that when ϕ_0 is increased from 0 in the first magic manifold, the annular shape of the real space wave functions remains unchanged.

C. The hypermagic regime

One may have noticed that in the bandwidth plot of Fig. 8(a) (where $w_0/w_1=0.8$) there are three dark spots at $\phi_0=\pi/2$ near $\alpha^{-1}=0.7,0.4$, and 0.3, indicating parameters with very small bandwidths for the lowest two bands at charge neutrality. The situation is identical at $\phi_0=-\pi/2$, which is related to $\phi_0=\pi/2$ by a particle-hole transformation P (see Appendix L).

To investigate what happens to the flat bands at $\phi_0 = \pm \pi/2$, we compute the bandwidth of the lowest two bands at charge neutrality at angle $\phi_0 = \pi/2$, as a function of α^{-1} and w_0/w_1 . The result is given in Fig. 8(c), where we find a small bandwidth region containing three curves with α^{-1} values around 0.7, 0.4, and 0.3 when $0 \le w_0/w_1 \le 3$. These curves start at $w_0/w_1 = 0$ and extend to at least $w_0/w_1 = 5$. The upper two curves merge around $w_0/w_1 = 0.2$, $\alpha^{-1} = 0.45$ and contain the so-called second magic angle in the chiral limit at $w_0/w_1 = 0$, $\alpha^{-1} = 0.45$ [12]. The third magic angle in the chiral limit at $w_0/w_1 = 0$, $\alpha^{-1} = 0.267$ lies on the lowest curve.

Figures 10(e) and 10(f) show example moiré band structures at points on each of the upper two dark curves in Fig. 8(c). Surprisingly, in both cases, we find several extremely flat bands in addition to the lowest two bands at

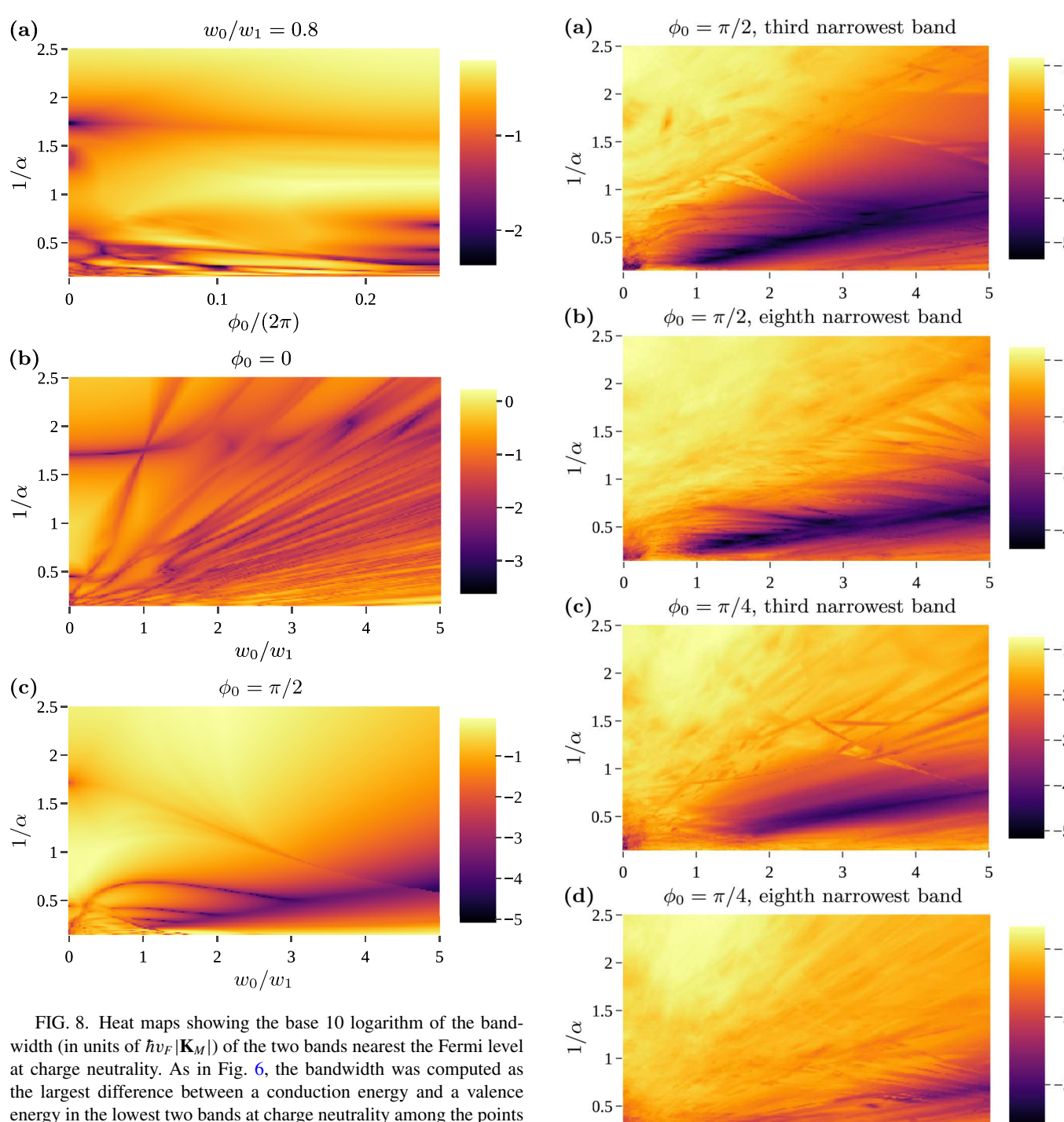


FIG. 8. Heat maps showing the base 10 logarithm of the bandwidth (in units of $\hbar v_F |\mathbf{K}_M|$) of the two bands nearest the Fermi level at charge neutrality. As in Fig. 6, the bandwidth was computed as the largest difference between a conduction energy and a valence energy in the lowest two bands at charge neutrality among the points Γ_M , \mathbf{K}_M , \mathbf{M}_M , $\mathbf{K}_M/2$, $\mathbf{M}_M/2$, $-\mathbf{M}_M/2$ in BZ_M. For this computation, we use the model in Eq. (69) with the quasimomentum truncation illustrated in Appendix Fig. 17. (a) shows the logarithm of the bandwidth as a function of α^{-1} [defined in Eq. (65)] and $\phi_0/(2\pi)$ while w_0/w_1 is fixed at 0.8. The nearly horizontal dark curve near $\alpha^{-1} = \sqrt{3}$ is part of the first magic manifold (see Sec. VIB). (b) and (c) show the logarithm of the bandwidth as a function of α^{-1} and w_0/w_1 while ϕ_0 is fixed at 0 and $\pi/2$, respectively. In panel (b), the nearly horizontal dark curve at $\alpha^{-1} \approx \sqrt{3}$ and $0 \leqslant w_0/w_1 \lesssim 1$ corresponds to the first magic manifold of small angle TBG. In (c), the three nearly horizontal dark curves around $\alpha^{-1} = 0.7$, 0.4, and 0.3 contain many simultaneous flat bands and are part of the hypermagic regime discussed in Sec. VIC.

FIG. 9. Heat maps showing the base 10 logarithm of the bandwidth (in units of $\hbar v_F |\mathbf{K}_M|$) of the third and eighth narrowest bands among the first 20 conduction bands and the first 20 valence bands at charge neutrality for $\phi_0 = \pi/2$ and $\pi/4$. The bandwidth was computed with the points Γ_M , \mathbf{K}_M , \mathbf{M}_M , $\mathbf{K}_M/2$, $\mathbf{M}_M/2$, $-\mathbf{M}_M/2$ in BZ_M. For this computation, we use the model in Eq. (69) with the quasimomentum truncation illustrated in Appendix Fig. 17. The dark regions indicate parameters in the hypermagic regime discussed in Sec. VI C. See Appendix Fig. 20 for similar heat maps with $\phi_0 = 0$, $\pi/8$, and $3\pi/8$.

 w_0/w_1

3

4

5

2

0

1

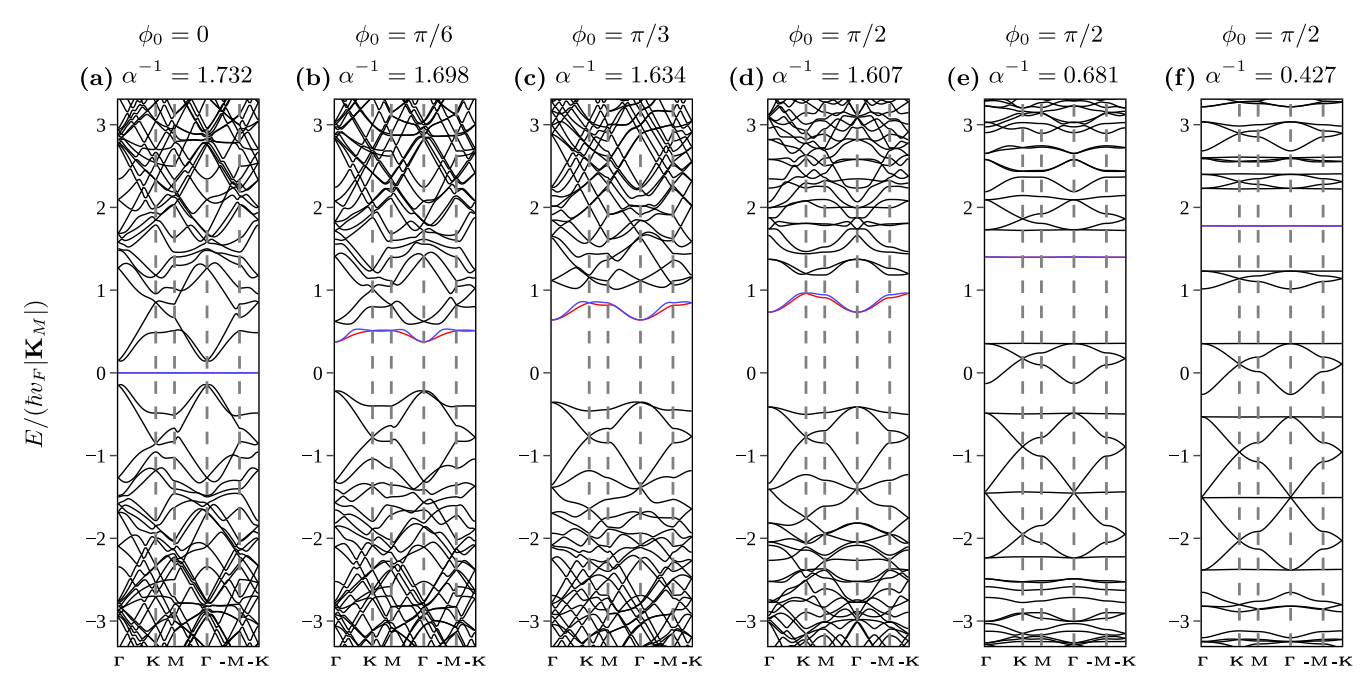


FIG. 10. Moiré band structures using the model in Eq. (69) with $w_0/w_1 = 0.8$, $w_2 = 0$, and the quasimomentum truncation illustrated in Appendix Fig. 17. The horizontal axes follow the moiré quasimomentum trajectory $\Gamma_M \to \mathbf{K}_M \to \mathbf{M}_M \to \Gamma_M \to -\mathbf{M}_M \to -\mathbf{K}_M$. The two bands nearest charge neutrality are shown in blue and red while all other bands are shown in black. The first four band structures have parameters in the first magic manifold (see Sec. VIB) with varying ϕ_0 . The last two band structures take parameters from the top two dark curves in Fig. 10(c).

charge neutrality. In total, there are at least seven flat bands in Fig. 10(e) and nine flat bands in Fig. 10(f)! Additional moiré band structures with parameters lying on the curves in Fig. 8(c) are given in Fig. 21. All of the plots show multiple flat bands, including those in Figs. 21(i) and 21(j), which correspond to the second and third magic angles in the chiral limit.

To further investigate this multiple flat band phenomenon, we plot in Fig. 9 the bandwidth of the third and eighth narrowest bands among the first 20 conduction bands and the first 20 valence bands at charge neutrality for $\phi_0 = \pi/2$ and $\pi/4$. In Fig. 9(a), we see that for $\phi_0 = \pi/2$ there is a large region (the dark diagonal band rising from the bottom left of the plot) in which there are 3 or more flat bands. Additionally, Fig. 9(b) shows that the region in which there are 8 or more flat bands is nearly as large as the region in which there are 3 or more flat bands. Figures 9(c) and 9(d) show that when ϕ_0 is decreased to $\pi/4$ the flat bands are often still present though less narrow. Appendix Fig. 20 shows similar heat maps for the angles $\phi_0 = 0$, $\pi/8$, and $3\pi/8$. At $\phi_0 = 0$, there are very few parameters for which there are more than two flat bands. We call the parameter region centered at $\phi_0 = \pm \pi/2$ in which there are many simultaneous flat bands the hypermagic regime.

Taking a closer look at the moiré bands around charge neutrality in Figs. 10(e) and 10(f), we see groups of three connected bands in which one band is very flat, there are Dirac cones at \mathbf{K}_M and $-\mathbf{K}_M$ between the other two bands, and there is a quadratic band touching at Γ_M between the flat band and one of the other bands. The second to fourth

valence bands at charge neutrality in Figs. 10(e) and 10(f) are examples of this pattern. Each such group of three connected bands resembles those of a tight-binding model on the kagome lattice [82,87,88]. Furthermore, the corresponding real space wavefunctions at Γ_M in Figs. 11(e) and 11(f) show a kagome lattice pattern and the Wilson loop bands in Fig. 13(f) are consistent with exponentially localizable Wannier functions [89,90]. Intriguingly, there is a band inversion transition along the lowest dark curve in Fig. 8(c) around $w_0/w_1 = 0.86$, $\alpha^{-1} = 0.3$. For w_0/w_1 slightly below 0.86, the lowest two moiré bands at charge neutrality are part of a group of three kagome-like bands while for w_0/w_1 just above 0.86, they form a pair of two isolated bands. This transition is illustrated in Figs. 12(a)-12(c).

In addition to the groups of three connected bands, we also see groups of four connected bands in which the top and bottom bands are very flat, there are Dirac cones at \mathbf{K}_{M} and $-\mathbf{K}_{M}$ between the middle two bands, and there are two quadratic band touchings at Γ_M , each involving one flat band. The second to fifth conduction bands at charge neutrality in Figs. 10(e) and 10(f) are examples of this pattern. These groups of four bands resemble those of the p_x , p_y 2-orbital honeycomb lattice tight-binding model [81,82]. Furthermore, the corresponding real space wave functions at Γ_M in Fig. 11(c) show a honeycomb lattice pattern and the Wilson loop bands in Fig. 13(d) are consistent with exponentially localizable Wannier functions [89,90]. We note that similar groups of three or four bands were also observed in a recent study of twisted Kitaev bilayers in Ref. [91]. Additional moiré band structures with parameters in the hypermagic regime

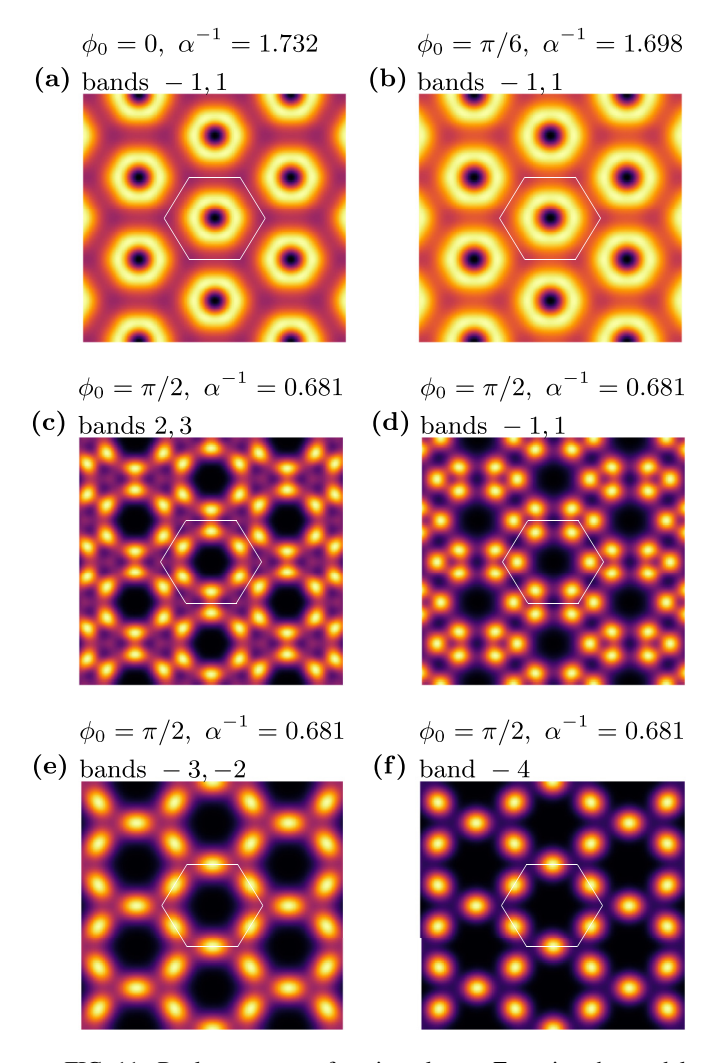


FIG. 11. Real space wave-function plots at Γ_M using the model in Eq. (69) with $w_0/w_1=0.8$ and the quasimomentum truncation illustrated in Appendix Fig. 17. Each plot shows the sum of the squares of the norms of the wave functions at Γ_M in the indicated bands, as a function of space. See Appendix N for more details. Light colors indicate large values and dark colors indicate small values, but the color scales in each plot are independent. The valence (conduction) bands are denoted with negative (positive) integers, so the highest (lowest) valence (conduction) band is denoted -1 (1). The white hexagons indicate the hexagonal primitive unit cell of the moiré superlattice. (a) and (b) correspond to Figs. 10(a) and 10(b) while (c)–(f) correspond to Fig. 10(e).

including some with $\phi_0 < \pi/2$ can be found in Appendix Fig. 22.

The continuum model in Eq. (69) (with $w_2 = 0$) at $\phi_0 = \pm \pi/2$ clearly has neither the particle-hole symmetry P nor the chiral symmetry C (see Appendix L for the definitions of these operators), due to the asymmetry between conduction bands and valence bands, for example in Refs. 10(e) and 10(f). As shown in Appendix L, conjugation by P maps the Hamiltonian \tilde{H} at angle ϕ_0 to $-\tilde{H}$ at angle $-\phi_0$, while keeping the other parameters invariant. In contrast, conjugation by P maps P at angle P0 to P1 at angle P1 at angle P2 to the other parameters invariant. Therefore the continuum model at angle

 $\phi_0 = \pm \pi/2$ has a combined *CP* symmetry:

$$[CP, \tilde{H}] = 0$$
 when $\phi_0 = \pm \frac{\pi}{2}$. (77)

No other values of ϕ_0 possess this symmetry unless $w_0 = 0$.

D. Band topology

Lastly, we discuss the band topology of the lowest two moiré bands at charge neutrality. It is known that in the BM model for small angle TBG [3], which corresponds to $\phi_0 = 0$ here [see Eq. (72)], the lowest two moiré bands carry a fragile topology protected by $C_{2z}\mathcal{T}$ symmetry, provided the two bands are disconnected from all other bands [4–8,92–94]. It was further shown in Ref. [86] that in the presence of both $C_{2z}\mathcal{T}$ symmetry and the anticommuting particle-hole symmetry P, the fragile topology becomes stable. See Appendix L for the definition of the P operator and recall that particle-hole symmetry is present only when $\phi_0 = 0$.

The fragile topology in the lowest two moiré bands at charge neutrality can be detected by computing their Wilson loop winding number modulo 2 [5,86,89,90]. See Appendix M for an explanation of the Wilson loop matrix and its band structure. Figure 13(a) shows the Wilson loop bands of the lowest two moiré bands using parameters corresponding to small angle TBG at the first magic angle. We find a winding number of 1, indicating nontrivial fragile topology. Away from $\phi_0 = 0$, the system no longer has particle-hole symmetry P, so the fragile topology of the lowest two moiré bands can potentially be lost.

We find that the fragile topology of the lowest two moiré flat bands at charge neutrality remains robust for any $\phi_0 \in [0, \pi/2]$ in the first magic manifold (see Sec. VIB) as long as they are gapped from the remote bands. Two examples of Wilson loop bands in the first magic manifold (with $w_0/w_1 = 0.8$) are given in Figs. 13(b) and 13(c) and both have a winding number of 1.

Computing Wilson loop bands in the hypermagic regime, we find that among parameters for which the lowest two bands are gapped from the higher bands, it is possible for the lowest two bands to have either trivial topology or nontrivial fragile topology. In order to transition from one of these possibilities to the other, there must be a gap closing between the lowest two bands and the higher bands. We illustrate one such gap closing in Figs. 12(d)–12(f). The gap closing occurs in Fig. 12(e) near the crossing between the upper two dark curves in Fig. 8(c). The parameters in Fig. 12(d) are near the second magic angle in the chiral limit and as a result the lowest two bands at charge neutrality have fragile topology [4–8]. In contrast, the bands in Fig. 12(f) are topologically trivial and resemble those of a honeycomb lattice tight-binding model. The Wilson loop bands corresponding to Figs. 12(d) and 12(f) are given in Figs. 13(g) and 13(h) and have Wilson loop winding numbers of 1 and 0, respectively. Figures 13(e) shows the Wilson bands corresponding to the lowest two bands at charge neutrality in Fig. 10(e) which are topologically trivial.

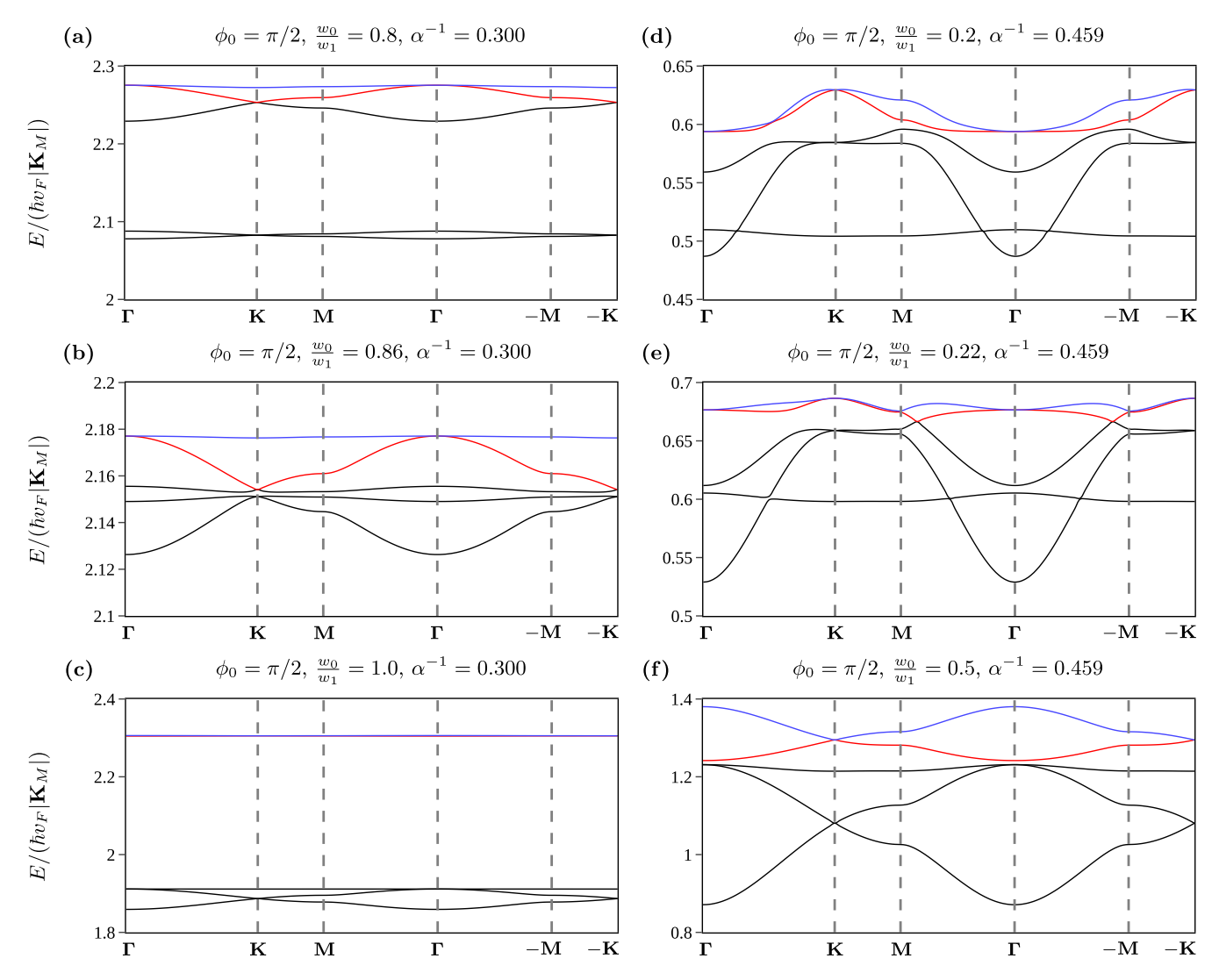


FIG. 12. Zoomed plots of moiré band structures near charge neutrality using the Hamiltonian in Eq. (69) and the quasimomentum truncation illustrated in Fig. 17. The horizontal axes follow the moiré quasimomentum trajectory $\Gamma_M \to K_M \to M_M \to \Gamma_M \to -M_M \to -K_M$. The two bands nearest charge neutrality are shown in blue and red while all other bands are shown in black. (a)–(c) show a band inversion transition near the lowest dark curve in Fig. 8(c). In (a), the lowest two moiré bands at charge neutrality form two of a group of three connected kagome-like bands. In contrast, in (c), the lowest two moiré bands at charge neutrality are gapped from the remote bands. A larger band structure with the same parameters as (a) is shown in Appendix Fig. 22(b). (d)–(f) show a gap closing transition between the lowest two bands at charge neutrality and the remote bands around the crossing of the upper two dark curves in Fig. 8(c). At this crossing, the topology of the lowest two bands changes from fragile topological in (d) to trivial in (f). The Wilson bands corresponding to (d) and (f) are shown in Figs. 13(g) and 13(h).

VII. DISCUSSION

We have derived an effective low energy continuum model for TBG at angle $\theta=\theta_0+\delta\theta$ near generic commensurate angles θ_0 . The model is characterized by complex interlayer hopping amplitudes $w_0e^{i\chi_0}$ and $w_0e^{-i\chi_0}$ at commensurate AA stackings, a real interlayer hopping amplitude w_1 at commensurate AB/BA stackings, and a global energy shift w_2 . The twist angle θ_0 and the phase χ_0 combine into a single angle parameter $\phi_0=\chi_0+\theta_0/2$ which affects the band structure of the effective continuum model in Eq. (69). Unless $\theta_0=0$, as in small angle TBG, ϕ_0 is generically nonzero. Taking the $\delta\theta\to 0$ limit yields a low-energy model for commensurate TBG, which gives a nonzero charge neutrality gap in the

AA stacking case if $\phi_0 \neq 0 \pmod{\pi}$, and gapless quadratic band touching in the AB/BA stacking cases. For commensurate angle $\theta_0 \approx 38.2^{\circ}$, the gap in the AA stacking case is around 1.6 meV and is therefore experimentally detectable. Away from commensurate angles, we find the first magic angle $\delta\theta_{\rm magic}$ near a generic commensurate angle θ_0 is still approximately given by $\alpha^{-1} = \sqrt{3}$ with α defined in Eq. (65). When $\phi_0 \neq 0$ at the first magic angle, the lowest two moiré bands at charge neutrality are generically flat except in the vicinity of the Γ_M point.

We have also revealed a hypermagic parameter regime centered at $\phi_0 = \pm \pi/2$, in which several moiré bands (often 8 or more) become flat simultaneously. The hypermagic regime

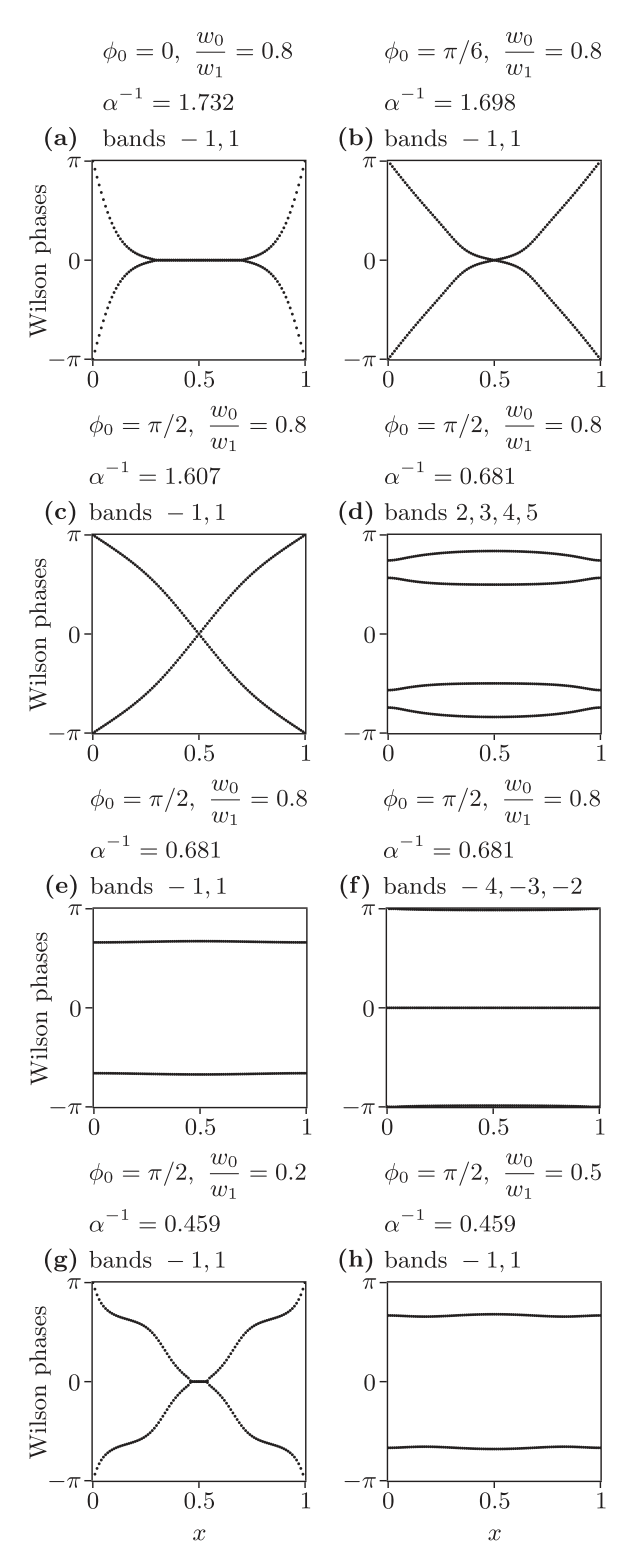


FIG. 13. Wilson loop bands for various connected groups of energy bands using the Hamiltonian in Eq. (69) and the quasimomentum truncation illustrated in Fig. 17. See Appendix M for an explanation of Wilson loop band structure. The valence (conduction) bands are denoted with negative (positive) integers, so the highest (lowest) valence (conduction) band is denoted -1 (1). The parameters of (a)–(c) are the same as those in Figs. 10(a), 10(b), and 10(d). The parameters of (d)–(f) are the same as those in Figs. 12(d) and 12(f).

includes the second and third magic angles in the chiral limit as well as parameters with large w_0/w_1 . We have identified a gap closing transition in the hypermagic regime between the lowest two bands at charge neutrality and the higher bands, across which the topology of the lowest two bands changes from fragile topological to trivial.

Many of the flat bands in the hypermagic regime belong to disconnected groups of bands which may be understood in terms of effective tight-binding models. Some groups of three bands resemble the kagome lattice tight-binding model which contains a flat band [82,87,88]. Other groups of four bands resemble the p_x , p_y 2-orbital honeycomb lattice tight-binding model which contains two flat bands [81,82].

The lowest two bands at charge neutrality often resemble the honeycomb lattice tight-binding model which can be used to describe monolayer graphene. If such hypermagic parameters can be achieved experimentally, one may expect the strongly interacting physics in the flat bands to be analogous to that in the conventional Hubbard model with trivial single-particle bands. This may allow the occurrence of antiferromagnetic states, in contrast to the spin-valley ferromagnetic states in interacting magic angle TBG with $\phi_0 = 0$ [44,45,57–59].

A practical future concern is how to achieve a continuum model with ϕ_0 near $\pm \pi/2$ and a sufficiently large energy scale for the parameters w_0 and w_1 to observe the hypermagic regime in experiment. The effective hopping parameters w_0 and w_1 at nonzero commensurate angles θ_0 (without lattice relaxation or other effects not considered here) are generically small. For example, w_0 and w_1 at $\theta_0 \approx 38.2^{\circ}$ are about 1 percent of those at $\theta_0 = 0^\circ$. One idea to enhance w_0 and w_1 is to explore the possibility of atomic interaction induced structural reconstruction (e.g., charge density waves) or lattice relaxation, which may enhance the moiré potential modulation between commensurate AA and AB/BA stackings. In addition, for small twist angles near the untwisted configuration $\theta_0 = 0$, breaking the mirror symmetry M_y (while preserving the other symmetries) would allow χ_0 to be nonzero, and therefore also ϕ_0 to be nonzero. Thus strong M_v breaking perturbations could transform small angle TBG into a large ϕ_0 model realization. Another interesting question is whether or not there exist other moiré models (e.g., involving twisted graphene multilayers or other twisted materials) for which there is a similar hypermagic regime where many bands become simultaneously flat. If other such models exist, it would be interesting to consider their common features and the underlying reasons for the existence of these hypermagic regimes. We leave these ideas and questions for future study.

ACKNOWLEDGMENTS

We thank Jonah Herzog-Arbeitman, Frank Schindler, and B. Andrei Bernevig for valuable discussions. This work is supported by the Alfred P. Sloan Foundation, the National Science Foundation through Princeton University's Materials Research Science and Engineering Center DMR-2011750, and the National Science Foundation under Award No. DMR-2141966. Additional support is provided by the Gordon and

Betty Moore Foundation through Grant No. GBMF8685 towards the Princeton theory program.

APPENDIX A: MICROSCOPIC HAMILTONIAN MATRIX ELEMENTS

In this Appendix, we derive Eqs. (6) and (9) for the intraand interlayer microscopic Hamiltonian matrix elements. Recall that L is the Bravais lattice of monolayer graphene, P is its reciprocal lattice, BZ is the Brillouin zone, $L_l = R_{-l\theta/2}L$, and $P_l = R_{-l\theta/2}P$. The Bloch states $|\mathbf{k}, l, \alpha\rangle$ are defined by Eq. (3) and satisfy the normalization condition Eq. (4). We first derive Eq. (6) under the simplifying assumption $\mu = 0$ so that Eq. (5) becomes $\langle \mathbf{r}', l, \alpha' | H | \mathbf{r}, l, \alpha \rangle = t_+(\mathbf{r}' + \boldsymbol{\tau}''_{\alpha'} - \mathbf{r} - \boldsymbol{\tau}'_{\alpha})$. Using the identity

$$\frac{1}{|BZ|} \sum_{\mathbf{r} \in L} e^{i\mathbf{k} \cdot \mathbf{r}} = \sum_{\mathbf{G} \in P} \delta^2(\mathbf{k} - \mathbf{G}), \tag{A1}$$

where |BZ| is the area of BZ, we compute

$$\langle \mathbf{k}', l, \alpha' | H | \mathbf{k}, l, \alpha \rangle = \frac{1}{|BZ|} \sum_{\mathbf{r}, \mathbf{r}' \in L_{l}} e^{-i\mathbf{k}' \cdot (\mathbf{r}' + \boldsymbol{\tau}_{\alpha'}^{l})} e^{i\mathbf{k} \cdot (\mathbf{r} + \boldsymbol{\tau}_{\alpha}^{l})} t_{+} (\mathbf{r}' + \boldsymbol{\tau}_{\alpha'}^{l} - \mathbf{r} - \boldsymbol{\tau}_{\alpha}^{l})$$

$$= \frac{1}{|BZ|} \sum_{\mathbf{r}' \in L_{l}} e^{-i\mathbf{r}' \cdot (\mathbf{k}' - \mathbf{k})} \sum_{\mathbf{r} \in L_{l}} e^{-i\mathbf{k}' \cdot \boldsymbol{\tau}_{\alpha'}^{l}} e^{i\mathbf{k} \cdot (\mathbf{r} - \mathbf{r}' + \boldsymbol{\tau}_{\alpha}^{l})} t_{+} (\mathbf{r}' - \mathbf{r} + \boldsymbol{\tau}_{\alpha'}^{l} - \boldsymbol{\tau}_{\alpha}^{l})$$

$$= \sum_{\mathbf{G}_{l} \in P_{l}} \delta^{2} (\mathbf{k}' - \mathbf{k} - \mathbf{G}_{l}) \sum_{\mathbf{r} \in L_{l}} e^{-i\mathbf{k}' \cdot \boldsymbol{\tau}_{\alpha'}^{l}} e^{i\mathbf{k} \cdot (-\mathbf{r} + \boldsymbol{\tau}_{\alpha}^{l})} t_{+} (\mathbf{r} + \boldsymbol{\tau}_{\alpha'}^{l} - \boldsymbol{\tau}_{\alpha}^{l})$$

$$= \sum_{\mathbf{G}_{l} \in P_{l}} \delta^{2} (\mathbf{k}' - \mathbf{k} - \mathbf{G}_{l}) e^{-i\mathbf{G}_{l} \cdot \boldsymbol{\tau}_{\alpha'}^{l}} \sum_{\mathbf{r} \in L_{l}} e^{-i\mathbf{k} \cdot (\mathbf{r} + \boldsymbol{\tau}_{\alpha'}^{l} - \boldsymbol{\tau}_{\alpha}^{l})} t_{+} (\mathbf{r} + \boldsymbol{\tau}_{\alpha'}^{l} - \boldsymbol{\tau}_{\alpha}^{l})$$

$$= \langle \mathbf{k}', l, \alpha' | \mathbf{k}, l, \alpha' \rangle \sum_{\mathbf{r} \in L + \boldsymbol{\tau}_{\lambda'} - \boldsymbol{\tau}_{\alpha}} e^{-i(R_{l\theta/2}\mathbf{k}) \cdot \mathbf{r}} t_{+} (\mathbf{r}). \tag{A2}$$

Note that we have used the rotational symmetry of the $t_+(\mathbf{r})$ function in the last step. When $\mu \neq 0$, the Hamiltonian is modified by subtraction of μ times the identity. As a result, the general form of the matrix element is

$$\langle \mathbf{k}', l, \alpha' | H | \mathbf{k}, l, \alpha \rangle = \langle \mathbf{k}', l, \alpha' | \mathbf{k}, l, \alpha' \rangle \left(-\mu + \sum_{\mathbf{r} \in L + \tau_{\alpha'} - \tau_{\alpha}} e^{-i(R_{l\theta/2}\mathbf{k}) \cdot \mathbf{r}} t_{+}(\mathbf{r}) \right), \tag{A3}$$

which is Eq. (6).

Next, we derive Eq. (9). Using Eq. (A1) and the identities

$$t_{-}(\mathbf{r}) = \int \frac{d^2\mathbf{q}}{(2\pi)^2} \hat{t}_{-}(\mathbf{q}) e^{i\mathbf{q}\cdot\mathbf{r}}, \quad |\Omega||BZ| = (2\pi)^2, \tag{A4}$$

where $|\Omega|$ is the area of the primitive unit cell Ω of L, we compute

$$\langle \mathbf{k}', -l, \alpha' | H | \mathbf{k}, l, \alpha \rangle = \frac{1}{|BZ|} \sum_{\mathbf{r}' \in L_{-l}} \sum_{\mathbf{r} \in L_{l}} e^{-i\mathbf{k}' \cdot (\mathbf{r}' + \boldsymbol{\tau}_{\alpha'}^{-l})} e^{i\mathbf{k} \cdot (\mathbf{r} + \boldsymbol{\tau}_{\alpha}^{l})} t_{-} (\mathbf{r}' + \boldsymbol{\tau}_{\alpha'}^{-l} - \mathbf{r} - \boldsymbol{\tau}_{\alpha}^{l})$$

$$= \frac{1}{|BZ|} \sum_{\mathbf{r}' \in L_{-l}} \sum_{\mathbf{r} \in L_{l}} \int \frac{d^{2}\mathbf{q}}{(2\pi)^{2}} \hat{t}_{-}(\mathbf{q}) e^{-i\mathbf{k}' \cdot (\mathbf{r}' + \boldsymbol{\tau}_{\alpha'}^{-l})} e^{i\mathbf{k} \cdot (\mathbf{r} + \boldsymbol{\tau}_{\alpha'}^{l})} e^{i\mathbf{q} \cdot (\mathbf{r}' + \boldsymbol{\tau}_{\alpha'}^{-l} - \mathbf{r} - \boldsymbol{\tau}_{\alpha}^{l})}$$

$$= |BZ| \int \frac{d^{2}\mathbf{q}}{(2\pi)^{2}} \hat{t}_{-}(\mathbf{q}) e^{i\boldsymbol{\tau}_{\alpha'}^{-l} \cdot (\mathbf{q} - \mathbf{k}')} e^{i\boldsymbol{\tau}_{\alpha}^{l} \cdot (\mathbf{k} - \mathbf{q})} \sum_{\mathbf{G}_{-l} \in P_{-l}} \delta^{2}(\mathbf{q} - \mathbf{k}' - \mathbf{G}_{-l}) \sum_{\mathbf{G}_{l} \in P_{l}} \delta^{2}(\mathbf{k} - \mathbf{q} + \mathbf{G}_{l})$$

$$= \sum_{\mathbf{G}_{-l} \in P_{-l}} \sum_{\mathbf{G}_{-l} \in P_{-l}} \frac{\hat{t}_{-}(\mathbf{k} + \mathbf{G}_{l})}{|\Omega|} e^{i\boldsymbol{\tau}_{\alpha'}^{-l} \cdot \mathbf{G}_{-l}} e^{-i\boldsymbol{\tau}_{\alpha'}^{l} \cdot \mathbf{G}_{l}} \delta^{2}(\mathbf{k} + \mathbf{G}_{l} - \mathbf{k}' - \mathbf{G}_{-l}), \tag{A5}$$

which is Eq. (9).

APPENDIX B: DIRAC CONES

In this Appendix, we derive Eq. (7). Since this equation is an approximation of Eq. (6) and both equations depend on the crystal momentum \mathbf{k} only through $R_{l\theta/2}\mathbf{k}$, it suffices to consider the case $\theta = 0$. That is, we need to show that the

single particle Hamiltonian for monolayer graphene at $\mathbf{K} + \mathbf{p}$ takes the form

$$\hbar v_F \sigma_0 \cdot \mathbf{p} + O(|\mathbf{p}|^2) \tag{B1}$$

when the chemical potential is chosen appropriately. Although this is well known, the most common derivation employs a model of graphene that has only first or second order hopping (for example, see Refs. [95,96]). We will now give an argument based on symmetry to show that Eq. (B1) holds with arbitrary order hopping. This is similar to the symmetry argument given in Sec. III in the case of twisted bilayer graphene near commensuration.

For monolayer graphene, we consider an orthonormal basis of spinless p_z orbitals $|\mathbf{r}, \alpha\rangle$ for $\mathbf{r} \in L$ and $\alpha \in \{A, B\}$ localized at $\mathbf{r} + \tau_{\alpha}$. We ignore the electron spin because of the weak spin-orbit coupling in graphene [83]. The Bloch states are defined by

$$|\mathbf{k}, \alpha\rangle = \frac{1}{\sqrt{|\mathrm{BZ}|}} \sum_{\mathbf{r} \in L} e^{i\mathbf{k} \cdot (\mathbf{r} + \tau_{\alpha})} |\mathbf{r}, \alpha\rangle$$
 (B2)

for crystal momentum vectors \mathbf{k} , and satisfy the normalization condition

$$\langle \mathbf{k}', \alpha' | \mathbf{k}, \alpha \rangle = \delta_{\alpha', \alpha} \sum_{\mathbf{G} \in P} \delta^2(\mathbf{k}' - \mathbf{k} - \mathbf{G}) e^{-i\tau_{\alpha} \cdot \mathbf{G}}.$$
 (B3)

We consider a microscopic Hamiltonian H_{mono} with matrix elements

$$\langle \mathbf{r}', \alpha' | H_{\text{mono}} | \mathbf{r}, \alpha \rangle = t_{+} (\mathbf{r}' + \boldsymbol{\tau}_{\alpha'} - \mathbf{r} - \boldsymbol{\tau}_{\alpha}) - \mu \delta_{\mathbf{r}', \mathbf{r}} \delta_{\alpha', \alpha},$$
(B4)

where μ is a chemical potential and $t_+: \mathbb{R}^2 \to \mathbb{R}$ is a rotationally symmetric function (i.e., $t_+(\mathbf{r})$ depends only on $|\mathbf{r}|$). The symmetries of H_{mono} are generated by the unitary operators C_{6z} (rotation by $\pi/3$ about $\hat{\mathbf{z}}$), M_y (reflection across the xz plane), and the antiunitary operator \mathcal{T} (time-reversal). These operators take the form

$$C_{6z} |\mathbf{k}, \alpha\rangle = |R_{\pi/3}\mathbf{k}, -\alpha\rangle,$$

$$M_{y} |\mathbf{k}, \alpha\rangle = |R^{x}\mathbf{k}, -\alpha\rangle,$$

$$\mathcal{T} |\mathbf{k}, \alpha\rangle = |-\mathbf{k}, \alpha\rangle,$$
(B5)

where R^x denotes reflection across the x axis. The symmetry subgroup that preserves the high-symmetry crystal momentum **K** is generated by $C_{2z}\mathcal{T}$, C_{3z} , and M_y , where $C_{2z} = C_{6z}^3$ and $C_{3z} = C_{6z}^2$. Using Eq. (B3), we find

$$C_{2z}\mathcal{T}|\mathbf{K}+\mathbf{p},\alpha\rangle = |\mathbf{K}+\mathbf{p},-\alpha\rangle,$$
 (B6)

$$C_{3z} | \mathbf{K} + \mathbf{p}, \alpha \rangle = e^{i(2\pi/3)\alpha} | \mathbf{K} + R_{2\pi/3} \mathbf{p}, \alpha \rangle,$$
 (B7)

$$M_{v} | \mathbf{K} + \mathbf{p}, \alpha \rangle = | \mathbf{K} + R^{x} \mathbf{p}, -\alpha \rangle.$$
 (B8)

If we expand the matrix elements of $H_{\rm mono}$ to second order around ${\bf K}$, we find

$$\langle \mathbf{K} + \mathbf{p}', \alpha' | H_{\text{mono}} | \mathbf{K} + \mathbf{p}, \alpha \rangle$$

= $(\mathcal{H}_{\text{mono}}(\mathbf{p})_{\alpha',\alpha} + O(|\mathbf{p}|^2))\delta^2(\mathbf{p}' - \mathbf{p}),$ (B9)

where $\mathcal{H}_{mono}(\mathbf{p})$ is a Hermitian 2×2 matrix that is linear in \mathbf{p} . Requiring

$$[C_{2z}T, H_{\text{mono}}] = [C_{3z}, H_{\text{mono}}] = [M_y, H_{\text{mono}}] = 0$$
 (B10)

implies

$$\mathcal{H}_{\text{mono}}(\mathbf{p}) = \sigma_{x} \overline{\mathcal{H}_{\text{mono}}(\mathbf{p})} \sigma_{x}$$
 (B11)

$$= e^{-i(2\pi/3)\sigma_z} \mathcal{H}_{\text{mono}}(R_{2\pi/3}\mathbf{p}) e^{i(2\pi/3)\sigma_z} \quad (B12)$$

$$= \sigma_x \mathcal{H}_{\text{mono}}(R^x \mathbf{p}) \sigma_x, \tag{B13}$$

where we use the notation \overline{M} for the complex conjugate of a matrix M. We now expand \mathcal{H}_{mono} in Pauli matrices as

$$\mathcal{H}_{\text{mono}}(\mathbf{p}) = h_0^0 \sigma_0 + h_0^x \sigma_x + h_0^y \sigma_y + h_0^z \sigma_z + (h_x^0 \sigma_0 + h_x^x \sigma_x + h_x^y \sigma_y + h_x^z \sigma_z) p_x + (h_v^0 \sigma_0 + h_v^x \sigma_x + h_v^y \sigma_y + h_v^z \sigma_z) p_y,$$
(B14)

where the h coefficients are real. First, we choose the value of μ so that $h_0^0 = 0$. Next, Eq. (B11) implies $h_0^z = h_x^z = h_y^z = 0$ and Eq. (B12) implies $h_0^x = h_0^y = h_x^0 = h_y^0 = 0$ and $h_y^y + ih_y^y = i(h_x^x + ih_x^y)$. If we define v_F and ϕ_F by $\hbar v_F e^{i\phi_F} = h_x^x + ih_x^y$, we have

$$\mathcal{H}_{\text{mono}}(\mathbf{p}) = \hbar v_F \boldsymbol{\sigma}_{\phi_F} \cdot \mathbf{p}. \tag{B15}$$

Finally, Eq. (B13) implies $\phi_F = 0$ so the Hamiltonian is described by Eq. (B1). We conclude that the $C_{2z}\mathcal{T}$ and C_{3z} symmetries imply that \mathcal{H}_{mono} takes the form of a Dirac cone and M_y symmetry determines the rotation angle of the Dirac cone.

APPENDIX C: EQUIVALENT CONFIGURATIONS

Note that the microscopic Hamiltonian in Eq. (5) is uniquely determined up to unitary equivalence by the relative positions of the carbon atoms in the *xy* plane and their partitioning into two layers. We will therefore consider systems differing only by an isometry of the *xy* plane and a relabeling of the basis states to be equivalent. This leads to significant redundancy in the specification of bilayer configurations, as we will now show.

With angle and translation parameters (θ, \mathbf{d}) , the atoms are located at sites

$$\{R_{-\theta/2}(\mathbf{r} + \boldsymbol{\tau}_{\alpha}) - \mathbf{d}/2 | \mathbf{r} \in L, \alpha \in \{A, B\}\} \cup \{R_{\theta/2}(\mathbf{r} + \boldsymbol{\tau}_{\alpha}) + \mathbf{d}/2 | \mathbf{r} \in L, \alpha \in \{A, B\}\},$$
(C1)

where the two terms indicate the top and bottom layers. Since this set and partitioning is invariant under the mapping $\theta \mapsto -\theta$, $\mathbf{d} \mapsto -\mathbf{d}$ (with an interchange of the two layers) the configurations with parameters (θ, \mathbf{d}) and $(-\theta, -\mathbf{d})$ are equivalent.

Next, consider the configuration with parameters $(\theta + \pi/3, R_{-\pi/6}\mathbf{d})$. If we rotate the whole system by the angle $\pi/6$, the bottom layer atoms are located at

$${R_{\theta/2+\pi/3}(\mathbf{r}+\mathbf{\tau}_{\alpha})+\mathbf{d}/2|\mathbf{r}\in L, \alpha\in\{A,B\}}$$
 (C2)

and the top layer atoms are located at

$${R_{-\theta/2}(\mathbf{r} + \boldsymbol{\tau}_{\alpha}) - \mathbf{d}/2 | \mathbf{r} \in L, \alpha \in {A, B}}.$$
 (C3)

Since $R_{\pi/3}L = L$ and $R_{\pi/3}\tau_{\alpha} - \tau_{-\alpha} \in L$, the bottom layer atoms are equivalently located at

$${R_{\theta/2}(\mathbf{r} + \boldsymbol{\tau}_{\alpha}) + \mathbf{d}/2 | \mathbf{r} \in L, \alpha \in {A, B}}.$$
 (C4)

Since these locations now match Eq. (C1), we see that the configurations with parameters (θ, \mathbf{d}) and $(\theta + \pi/3, R_{-\pi/6}\mathbf{d})$ are equivalent. As a result of these equivalences, we can restrict θ to the interval $[0, \pi/3)$ and note that the configurations (θ, \mathbf{d}) and $(\pi/3 - \theta, -R_{-\pi/6}\mathbf{d})$ are equivalent.

Next, consider the configuration with parameters $(\theta, \mathbf{d} + \mathbf{X})$ for a vector $\mathbf{X} \in \mathbb{R}^2$. If we translate the whole system by

 $\mathbf{X}/2$, the atoms are located at sites

$$\{R_{-\theta/2}(\mathbf{r} + \boldsymbol{\tau}_{\alpha}) - \mathbf{d}/2 | \mathbf{r} \in L, \alpha \in \{A, B\}\} \cup \{R_{\theta/2}(\mathbf{r} + \boldsymbol{\tau}_{\alpha}) + \mathbf{d}/2 + \mathbf{X} | \mathbf{r} \in L, \alpha \in \{A, B\}\}.$$
(C5)

If $X \in L_{-}$ then this matches Eq. (C1) so the configurations with parameters (θ, \mathbf{d}) and $(\theta, \mathbf{d} + \mathbf{X})$ are equivalent. Similarly, if we translate the whole system by $-\mathbf{X}/2$, we see that when $\mathbf{X} \in L_+$ the configurations with parameters (θ, \mathbf{d}) and $(\theta, \mathbf{d} + \mathbf{X})$ are equivalent. Putting these results together, we see that whenever $X \in L_{-} + L_{+}$, the configurations with parameters (θ, \mathbf{d}) and $(\theta, \mathbf{d} + \mathbf{X})$ are equivalent.

We show in Appendix D2 that when θ is a commensurate angle, $L_{-} + L_{+}$ is a Bravais lattice whose reciprocal lattice is $P_- \cap P_+$. Furthermore, it follows from the results of Appendix D6 that for commensurate θ , no set S larger than $L_{-} + L_{+}$ has the property that the configurations with parameters (θ, \mathbf{d}) and $(\theta, \mathbf{d} + \mathbf{X})$ are equivalent for all $\mathbf{d} \in \mathbb{R}^2$ and all $X \in S$. On the other hand, we show in Appendix E that when θ is not a commensurate angle, $L_{-} + L_{+}$ is a dense subset of \mathbb{R}^2 . Since the Hamiltonian depends continuously on **d**, it follows that for incommensurate θ the configurations with parameters $(\theta, \mathbf{0})$ and (θ, \mathbf{d}) are equivalent for all $\mathbf{d} \in \mathbb{R}^2$.

APPENDIX D: PROPERTIES OF COMMENSURATE CONFIGURATIONS

Using a combination of elementary number theory and symmetry arguments, these appendices enumerate and characterize the commensurate configurations of TBG. The approach taken in Appendixes D 1 and D 2 is similar to that in Ref. [2], but we include detailed derivations for completeness. We follow the notations of Secs. II A and II B.

1. Enumeration of commensurate configurations

We first seek to enumerate the commensurate configurations. Recall that \mathbf{a}_1 , \mathbf{a}_2 are primitive vectors for L and \mathbf{b}_1 , \mathbf{b}_2 are primitive vectors for P, as illustrated in Fig. 1. Let a and b denote matrices with columns $(\mathbf{a}_1, \mathbf{a}_2)$ and $(\mathbf{b}_1, \mathbf{b}_2)$, respectively. Explicitly, we have

$$a = a_0 \begin{pmatrix} \sqrt{3} & \sqrt{3}/2 \\ 0 & -3/2 \end{pmatrix},$$

$$b = \frac{2\pi}{a_0} \begin{pmatrix} \sqrt{3}/3 & 0 \\ 1/3 & -2/3 \end{pmatrix}.$$
 (D1)

Recall from Sec. IIB that the bilayer system is commensurate when $L_- \cap L_+ \neq \{0\}$, and in this case $L_- \cap L_+$ is the commensuration superlattice. $L_- \cap L_+ \neq \{0\}$ is equivalent to the existence of nonzero integer vectors \mathbf{u}_+ and \mathbf{u}_- such that

$$\mathbf{u}_{+} = a^{-1} R_{\theta} a \mathbf{u}_{-}. \tag{D2}$$

Similarly, $P_- \cap P_+ \neq \{0\}$ is equivalent to the existence of nonzero integer vectors \mathbf{v}_+ and \mathbf{v}_- such that

$$\mathbf{v}_{+} = b^{-1} R_{\theta} b \mathbf{v}_{-}. \tag{D3}$$

Note that

$$a^{-1}R_{\theta}a = \begin{pmatrix} x_0 + y_0 & 2y_0 \\ -2y_0 & x_0 - y_0 \end{pmatrix},$$
(D4)
$$b^{-1}R_{\theta}b = \begin{pmatrix} x_0 - y_0 & 2y_0 \\ -2y_0 & x_0 + y_0 \end{pmatrix},$$
(D5)

$$b^{-1}R_{\theta}b = \begin{pmatrix} x_0 - y_0 & 2y_0 \\ -2y_0 & x_0 + y_0 \end{pmatrix},$$
 (D5)

where $x_0 = \cos \theta$, $y_0 = \frac{1}{\sqrt{3}} \sin \theta$. It follows that the bilayer system is commensurate if and only if x_0 and y_0 are both rational, which is equivalent to the $L_- \cap L_+ \neq \{0\}$ and $P_- \cap P_+ \neq \{0\}$ **{0**}.

From here on, we will use θ_0 in place of θ when we assume the system is commensurate in order to match the notation of Sec. IIB. If the system is commensurate, then (x_0, y_0) is a rational point on the ellipse $x^2 + 3y^2 = 1$. Unless $(x_0, y_0) = (1, 0)$, the line through (x_0, y_0) and (1, 0) intersects the y axis at a rational point (0, m/n) where m, n are relatively prime integers with n > 0. Solving $x^2 + 3y^2 = 1$ simultaneously with $x = -\frac{n}{m}y + 1$ yields

$$x_0 = \frac{3m^2 - n^2}{3m^2 + n^2},$$

$$y_0 = \frac{2mn}{3m^2 + n^2}.$$
 (D6)

The special case $(x_0, y_0) = (1, 0)$ corresponds to (m, n) =(1,0). By the results of Appendix C, we can restrict $\theta_0 \in$ $[0, \pi/3)$ so that $m > n \ge 0$ and $\theta_0 = \cos^{-1}(x_0)$.

2. Commensuration lattices

We now determine the primitive vectors and reciprocal lattices of $L_- \cap L_+$ and $P_- \cap P_+$ assuming θ_0 is a commensurate angle. We have

$$a^{-1}R_{\theta_0}a = \frac{1}{N} \begin{pmatrix} \alpha & \beta \\ -\beta & \gamma \end{pmatrix}, \tag{D7}$$

$$b^{-1}R_{\theta_0}b = \frac{1}{N} \begin{pmatrix} \gamma & \beta \\ -\beta & \alpha \end{pmatrix}, \tag{D8}$$

$$\alpha = (m+n)(3m-n)/d_0,$$
 (D9)

$$\beta = 4mn/d_0 = \alpha - \gamma, \tag{D10}$$

$$\gamma = (m - n)(3m + n)/d_0,$$
 (D11)

$$N = (3m^2 + n^2)/d_0,$$
 (D12)

where d_0 is the greatest common divisor of the numerators of α , β , γ , N. Note that α should not be confused with the model parameter defined in Eq. (65) and used in the main text. If $3 \nmid n$ (i.e., 3 does not divide n) then the numerator of N is 1 (mod 3) so $3 \nmid d_0$. On the other hand, if $3 \mid n$ then $3 \mid d_0$ but $9 \nmid d_0$ since $3 \nmid m$. In either case, $3 \nmid N$. If one of m and n is even, then the numerator of N is odd so d_0 is odd. On the other hand, if m and n are both odd then $4|d_0$, but considering the numerator of β we see that $8 \nmid d_0$. If p is a prime divisor of d_0 other than 2 then considering the numerator of β , we see that p|m or p|n but not both. Considering the numerator of N,

we see that p = 3. We conclude

$$d_0 = \gcd(4mn, 3m^2 + n^2)$$

$$= \begin{cases} 1 & \text{if } (2|n \text{ or } 2|m) \text{ and } 3 \nmid n \\ 3 & \text{if } (2|n \text{ or } 2|m) \text{ and } 3|n \\ 4 & \text{if } 2 \nmid n \text{ and } 2 \nmid m \text{ and } 3 \nmid n, \\ 12 & \text{if } 2 \nmid n \text{ and } 2 \nmid m \text{ and } 3|n \end{cases}$$
(D13)

so that $gcd(\beta, N) = 1$. Also, since $det(a^{-1}R_{\theta_0}a) = 1$ we have $\alpha \gamma + \beta^2 = N^2$.

Assume for now that $(m, n) \neq (1, 0)$ so that $\beta \neq 0$. Writing \mathbf{u}_{-} in components as $\mathbf{u}_{-} = x\hat{\mathbf{x}} + y\hat{\mathbf{y}}$ for integers x, y, Eq. (D2) becomes

$$\frac{1}{N} \begin{pmatrix} \alpha & \beta \\ -\beta & \gamma \end{pmatrix} \begin{pmatrix} x \\ y \end{pmatrix} \in \mathbb{Z}^2, \tag{D14}$$

which is in turn equivalent to the pair of congruences

$$\alpha x + \beta y \equiv 0 \pmod{N},$$
 (D15)

$$-\beta x + \gamma y \equiv 0 \pmod{N}.$$
 (D16)

Since $\beta \neq 0$ and $gcd(\beta, N) = 1$, we can multiply Eq. (D16) through by β . However since $-\beta^2 \equiv \alpha \gamma \pmod{N}$, we see that this equation is implied Eq. (D15). Furthermore, Eq. (D15) can be solved as

$$x = n_1,$$

 $y = n_1(-\beta^{-1}\alpha) + n_2N$ (D17)

for integers n_1 , n_2 , where β^{-1} is the smallest non-negative integer such that $\beta^{-1}\beta = 1 \pmod{N^2}$. As a result, the set of integer vectors **u** such that $a^{-1}R_{\theta_0}a\mathbf{u}$ is an integer vector forms a Bravais lattice with primitive vectors

$$\mathbf{u}_{1}^{-} = \hat{\mathbf{x}} - \beta^{-1}\alpha\hat{\mathbf{y}},$$

$$\mathbf{u}_{2}^{-} = N\hat{\mathbf{y}}.$$
 (D18)

In the case (m, n) = (1, 0), $a^{-1}R_{\theta_0}a = I$, N = 1, and $\beta^{-1} = 0$ so this result still holds. The image of this lattice under $a^{-1}R_{\theta_0}a$ is also a Bravais lattice with corresponding primitive vectors

$$\mathbf{u}_{1}^{+} = a^{-1}R_{\theta_{0}}a\mathbf{u}_{1}^{-} = -\alpha\rho\hat{\mathbf{x}} + (\beta\rho - \beta^{-1}N)\hat{\mathbf{y}},$$

$$\mathbf{u}_{2}^{+} = a^{-1}R_{\theta_{0}}a\mathbf{u}_{2}^{-} = \beta\hat{\mathbf{x}} + \gamma\hat{\mathbf{y}},$$

$$\rho = (\beta^{-1}\beta - 1)/N \in N\mathbb{Z}.$$
(D19)

We conclude that the commensuration superlattice takes the form

$$L_{-} \cap L_{+} = \{R_{-\theta_{0}/2}a(n_{1}\mathbf{u}_{1}^{+} + n_{2}\mathbf{u}_{2}^{+})|n_{1}, n_{2} \in \mathbb{Z}\}$$

$$= \{R_{\theta_{0}/2}a(n_{1}\mathbf{u}_{1}^{-} + n_{2}\mathbf{u}_{2}^{-})|n_{1}, n_{2} \in \mathbb{Z}\}. \quad (D20)$$

Note that the unit cell of $L_- \cap L_+$ has area $N|\Omega|$.

We can use this result to compute the reciprocal lattice of $L_- \cap L_+$. Let this reciprocal lattice be called \tilde{P} and note that primitive vectors for \tilde{P} can be given by

$$\tilde{\mathbf{u}}_{1} = \frac{1}{N} R_{-\theta_{0}/2} b(\gamma \hat{\mathbf{x}} - \beta \hat{\mathbf{y}}) = R_{\theta_{0}/2} b \hat{\mathbf{x}},$$

$$\tilde{\mathbf{u}}_{2} = R_{-\theta_{0}/2} b[(-\beta \rho/N + \beta^{-1}) \hat{\mathbf{x}} - (\alpha \rho/N) \hat{\mathbf{y}}]$$

$$= \frac{1}{N} R_{\theta_{0}/2} b(\beta^{-1} \alpha \hat{\mathbf{x}} + \hat{\mathbf{y}}).$$
(D21)

Since ρ/N is an integer, $\tilde{\mathbf{u}}_1 \in P_-$, $\tilde{\mathbf{u}}_2 \in P_+$ so $\tilde{P} \subset P_- + P_+$. However, by the definition of the reciprocal lattice $P_- + P_+ \subset \tilde{P}$ so that $\tilde{P} = P_- + P_+$. Note that the unit cell for \tilde{P} has area $|\mathrm{BZ}|/N$.

Since Eqs. (D7) and (D8) are related by the interchange of α and γ , corresponding results for the reciprocal lattices can be obtained by interchanging α and γ . The set of integer vectors \mathbf{v} such that $b^{-1}R_{\theta_0}b\mathbf{v}$ is an integer vector forms a Bravais lattice with primitive vectors

$$\mathbf{v}_{1}^{-} = \hat{\mathbf{x}} - \beta^{-1} \gamma \hat{\mathbf{y}},$$

$$\mathbf{v}_{2}^{-} = N \hat{\mathbf{y}},$$
 (D22)

and the image of this lattice under $b^{-1}R_{\theta_0}b$ is also a Bravais lattice with corresponding primitive vectors

$$\mathbf{v}_{1}^{+} = b^{-1} R_{\theta_{0}} b \mathbf{v}_{1}^{-} = -\gamma \rho \hat{\mathbf{x}} + (\beta \rho - \beta^{-1} N) \hat{\mathbf{y}},$$

$$\mathbf{v}_{2}^{+} = b^{-1} R_{\theta_{0}} b \mathbf{v}_{2}^{-} = \beta \hat{\mathbf{y}} + \alpha \hat{\mathbf{y}}.$$
 (D23)

We conclude

$$P_{-} \cap P_{+} = \{ R_{-\theta_{0}/2}b(n_{1}\mathbf{v}_{1}^{+} + n_{2}\mathbf{v}_{2}^{+})|n_{1}, n_{2} \in \mathbb{Z} \}$$
$$= \{ R_{\theta_{0}/2}b(n_{1}\mathbf{v}_{1}^{-} + n_{2}\mathbf{v}_{2}^{-})|n_{1}, n_{2} \in \mathbb{Z} \}, \quad (D24)$$

the reciprocal lattice of $P_- \cap P_+$ is $L_- + L_+$, and the unit cell of $P_- \cap P_+$ has area N|BZ|.

3. Equivalences between top and bottom K and K' points

We will now derive Eqs. (12) to (14) starting with Eq. (14). By Eq. (2),

$$\mathbf{K}_{l} = R_{-l\theta_{0}/2}\mathbf{K}$$

$$= R_{-l\theta_{0}/2}(2\mathbf{b}_{1} + \mathbf{b}_{2})/3$$

$$= R_{-l\theta_{0}/2}b(2\hat{\mathbf{x}} + \hat{\mathbf{y}})/3$$
 (D25)

and similarly $\mathbf{K}'_l = R_{-l\theta_0/2}b(\hat{\mathbf{x}} + 2\hat{\mathbf{y}})$, so that $\mathbf{K}_l - \mathbf{K}'_l = R_{-l\theta_0/2}(\hat{\mathbf{x}} - \hat{\mathbf{y}})/3$. Examining the primitive vectors $\hat{\mathbf{u}}_1$ and $\tilde{\mathbf{u}}_2$ for $P_- + P_+$ in Eq. (D21), we see that if $R_{-l\theta_0/2}b\mathbf{v} \in P_- + P_+$ where \mathbf{v} is a rational vector then the denominators of $\mathbf{v} \cdot \hat{\mathbf{x}}$ and $\mathbf{v} \cdot \hat{\mathbf{y}}$ must divide N. Since $3 \nmid N$, it follows that $\mathbf{K}_l - \mathbf{K}'_l \not\in P_- + P_+$, which is Eq. (14).

Next, since $3 \nmid N$ there is an integer $k \in \{0, 1, 2\}$ such that

$$kN = 2 + \beta^{-1} \gamma \pmod{3}$$
 (D26)

so that by Eq. (D22) we have

$$\mathbf{v}_1^- + k\mathbf{v}_2^- = \hat{\mathbf{x}} + 2\hat{\mathbf{y}} \pmod{3}.$$
 (D27)

Recalling that $\mathbf{v}_{i}^{+} = b^{-1}R_{\theta_{0}}b\mathbf{v}_{i}^{-}$ for j = 1, 2 we then have

$$\mathbf{K}_{-} = -R_{\theta_0/2}b(\mathbf{v}_{1}^{-} + k\mathbf{v}_{2}^{-})/3 + \mathbf{G}_{-}$$

$$= -R_{-\theta_0/2}b(\mathbf{v}_{1}^{+} + k\mathbf{v}_{2}^{+})/3 + \mathbf{G}_{-},$$

$$\mathbf{K}'_{-} = R_{\theta_0/2}b(\mathbf{v}_{1}^{-} + k\mathbf{v}_{2}^{-})/3 + \mathbf{G}'_{-}$$

$$= R_{-\theta_0/2}b(\mathbf{v}_{1}^{+} + k\mathbf{v}_{2}^{+})/3 + \mathbf{G}'_{-}$$
(D28)

for some G_- , $G'_- \in P_-$. Multiplying these equations by $R_{-\theta_0}$, we find

$$\mathbf{K}_{+} = -R_{-\theta_{0}/2}b(\mathbf{v}_{1}^{-} + k\mathbf{v}_{2}^{-})/3 + \mathbf{G}_{+},$$

$$\mathbf{K}'_{+} = R_{-\theta_{0}/2}b(\mathbf{v}_{1}^{-} + k\mathbf{v}_{2}^{-})/3 + \mathbf{G}'_{+},$$
(D29)

where $G_{+} = R_{-\theta_0}G_{-} \in P_{+}$ and $G'_{+} = R_{-\theta_0}G'_{+} \in P_{+}$. Note

$$\mathbf{K}_{+} - \mathbf{K}_{-} = R_{-\theta_0/2}b(\mathbf{v}_{1}^{+} - \mathbf{v}_{1}^{-} + k(\mathbf{v}_{2}^{+} - \mathbf{v}_{2}^{-}))/3 + \mathbf{G}_{+} - \mathbf{G}_{-}$$
(D30)

so $\mathbf{K}_{+} - \mathbf{K}_{-} \in P_{-} + P_{+}$ if and only if $R_{-\theta_{0}/2}b(\mathbf{v}_{1}^{+} - \mathbf{v}_{1}^{-} + k(\mathbf{v}_{2}^{+} - \mathbf{v}_{2}^{-}))/3 \in P_{-} + P_{+}$. By the same argument as before, we see that $\mathbf{K}_+ - \mathbf{K}_- \in P_- + P_+$ if and only if

$$\mathbf{v}_1^+ + k\mathbf{v}_2^+ = \hat{\mathbf{x}} + 2\hat{\mathbf{y}} \pmod{3}$$
 (D31)

in which case we also have $\mathbf{K}'_{+} - \mathbf{K}'_{-} \in P_{-} + P_{+}$. Similarly, $\mathbf{K}_{+} - \mathbf{K}'_{-} \in P_{-} + P_{+}$ if and only if

$$\mathbf{v}_1^+ + k\mathbf{v}_2^+ = 2\hat{\mathbf{x}} + \hat{\mathbf{y}} \pmod{3}$$
 (D32)

in which case we also have $\mathbf{K}'_{+} - \mathbf{K}_{-} \in P_{-} + P_{+}$.

Using Eqs. (D23) and (D26), $\alpha \gamma + \beta^2 = N^2 = 1 \pmod{3}$, and $\beta = \alpha - \gamma$, one can show

$$\mathbf{v}_1^+ + k\mathbf{v}_2^+ = N(\alpha + \gamma)(2\hat{\mathbf{x}} + \hat{\mathbf{y}}) \pmod{3}.$$
 (D33)

Additionally, using Eq. (D13), we find

$$N(\alpha + \gamma) = 2(9m^4 - n^4)/d_0^2$$

$$= \begin{cases} 1 \pmod{3} & \text{if } 3 \nmid n \\ 2 \pmod{3} & \text{if } 3 \mid n \end{cases}$$
(D34)

Let $(\mathbf{J}_{-}, \mathbf{J}'_{-})$ denote $(\mathbf{K}_{-}, \mathbf{K}'_{-})$ when 3|n and $(\mathbf{K}'_{-}, \mathbf{K}_{-})$ when $3 \nmid n$. We then conclude $\mathbf{K}_+ - \mathbf{J}_-, \mathbf{K}'_+ - \mathbf{J}'_- \in P_- +$ P_+ , which is equivalent to Eqs. (12) and (13).

4. Pairs of complementary commensurate configurations

It follows from Appendix C that when θ_0 is a commensurate angle, $\pi/3 - \theta_0$ is also a commensurate angle. We will now prove this statement another way and consider an important relationship between the two configurations that is used in Sec. IIB.

Returning to the notation of Appendix D 1, let

$$x_1 = \cos(\pi/3 - \theta_0) = \frac{1}{2}(x_0 + 3y_0),$$

$$y_1 = \frac{1}{\sqrt{3}}\sin(\pi/3 - \theta_0) = \frac{1}{2}(x_0 - y_0).$$
 (D35)

Since θ_0 is a commensurate angle, x_0 and y_0 are rational, and therefore x_1 and y_1 are rational. It follows that $\pi/3 - \theta_0$ is also commensurate. If (x_0, y_0) corresponds to the integer pair (m_0, n_0) and (x_1, y_1) corresponds to the integer pair (m_1, n_1) then

$$\frac{m_1}{n_1} = \frac{y_1}{1 - x_1} = \frac{3m_0^2 - 2m_0n_0 - n_0^2}{3(m_0 - n_0)^2}.$$
 (D36)

If $3|n_0$ then $3\nmid m_0$ so the denominator of this fraction is divisible by 3 exactly once. However, the numerator is also divisible by 3 so we conclude 3 n_1 . On the other hand, suppose 3 n_0 . It is straightforward to see that the largest power of 3 dividing the numerator is the same as the largest power of 3 dividing $m_0 - n_0$, so we conclude $3|n_1$. As a result, in one of the commensurate configurations corresponding to θ_0 and $\pi/3 - \theta_0$ we have $(\mathbf{J}_-, \mathbf{J}'_-) = (\mathbf{K}_-, \mathbf{K}'_-)$, and in the other we have $(J_-, J'_-) = (K'_-, K_-)$.

5. The lattices Q_+ and Q_0

In this section, we prove Eq. (32), find the minimal norm elements of $(\mathbf{K}_- + P_-) \cap (\mathbf{K}_+ + P_+)$, and derive the forms of $L_- \cap L_+$, $P_- \cap P_+$, $L_- + L_+$, and $P_- + P_+$. As explained in Sec. II B, we assume 3|n so that $\mathbf{J}_{-} = \mathbf{K}_{-}$. Since $(\mathbf{K}_{-} + P_{-}) \cap$ $(\mathbf{K}_+ + P_+)$ is closed under addition by elements of $P_- \cap P_+$ and has the property that the difference of any two elements is in $P_- \cap P_+$, we must have

$$(\mathbf{K}_{-} + P_{-}) \cap (\mathbf{K}_{+} + P_{+}) = \mathbf{k}_{0} + P_{-} \cap P_{+}$$
 (D37)

for some vector \mathbf{k}_0 . Since $P_- \cap P_+$ is a triangular lattice, $\mathbf{k}_0 + P_- \cap P_+$ has at most three elements of minimal norm. However, since $(\mathbf{K}_- + P_-) \cap (\mathbf{K}_+ + P_+)$ has 3-fold rotational symmetry and does not contain 0, it must have exactly three elements of minimal norm. Since $(\mathbf{K}_{-} + P_{-}) \cap (\mathbf{K}_{+} + P_{+})$ additionally has symmetry under reflection across the vector K, one of the elements of minimal norm must be proportional to **K**. Since the unit cell of $P_- \cap P_+$ has area N|BZ|, we conclude $P_- \cap P_+ = \sqrt{N}P$ and the element of minimal norm proportional to **K** must be $\mathbf{Q}_1 = s\sqrt{N}\mathbf{K}$ where s is 1 or -1. The other two elements of minimal norm are $\mathbf{Q}_2 = R_{2\pi/3}\mathbf{Q}_1$ and $\mathbf{Q}_3 = R_{4\pi/3}\mathbf{Q}_1$, and we can write

$$(\mathbf{K}_{-} + P_{-}) \cap (\mathbf{K}_{+} + P_{+}) = s\sqrt{N}\mathbf{K} + P_{-} \cap P_{+}.$$
 (D38)

Recalling from Appendix D2 that the reciprocal lattice of $P_- \cap P_+$ is $L_- + L_+$, it follows that $L_- + L_+ = L/\sqrt{N}$. Applying the same argument to the real space lattices, we see that $L_- \cap L_+ = \sqrt{NL}$ so that $P_- + P_+ = P/\sqrt{N}$.

We will now determine the sign s. We have $s\sqrt{N}\mathbf{K} - \mathbf{K}_l \in$ P_l or equivalently $(s\sqrt{NR_{l\theta_0/2}} - I)\mathbf{K} \in P$. Using the halfangle formulas and the results of Appendixes D 1 and D 2 we find

$$\cos(\theta_0/2) = \frac{m\sqrt{3}}{\sqrt{d_0 N}},$$

$$\sin(\theta_0/2) = \frac{n}{\sqrt{d_0 N}},$$
(D39)

$$\sin(\theta_0/2) = \frac{n}{\sqrt{d_0 N}},\tag{D40}$$

$$(s\sqrt{N}R_{l\theta_0/2} - I)\mathbf{K} = \frac{4\pi\sqrt{3}}{9a_0}((sm\sqrt{3/d_0} - 1)\mathbf{\hat{x}} + (sln/\sqrt{d_0})\mathbf{\hat{y}}).$$
(D41)

For comparison,

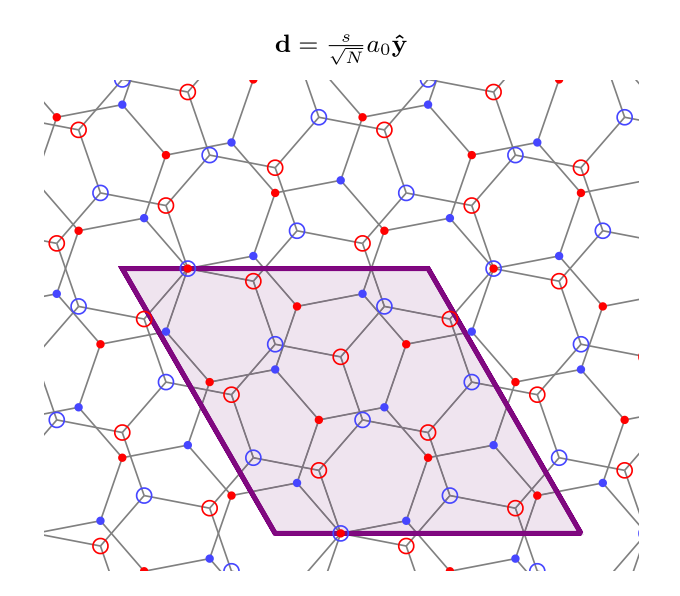
$$n_1 \mathbf{b}_1 + n_2 \mathbf{b}_2 = \frac{4\pi\sqrt{3}}{9a_0} ((3n_1/2)\hat{\mathbf{x}} + (n_1/2 - n_2)\sqrt{3}\hat{\mathbf{y}}).$$
(D42)

By Eq. (D13), when $m \pm n$ is odd, we have $d_0 = 3$ so the equation $(s\sqrt{NR_{l\theta_0/2}}-I)\mathbf{K}=n_1\mathbf{b}_1+n_2\mathbf{b}_2$ has a solution if and only if $sm = 1 \pmod{3}$. When $m \pm n$ is even, we have $d_0 = 12$ so the same equation now has a solution if and only if $sm = 2 \pmod{3}$. We summarize both cases by saying

$$s = \frac{m \pm n}{\sqrt{d_0/3}} \pmod{3} \text{ and } s = \pm 1.$$
 (D43)

6. AA, AB, and BA stacking commensurate configurations

We say that a commensurate configuration has AA stacking if there is an A sublattice atom on the top layer that is directly above some A sublattice atom on the bottom layer. Similarly



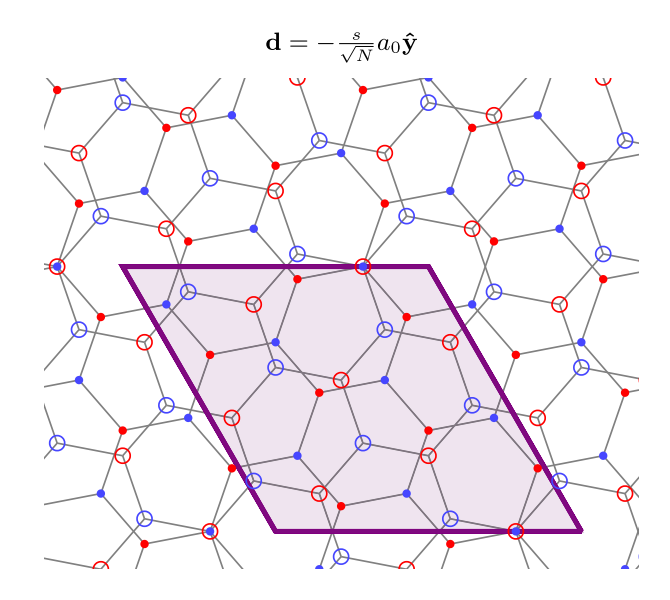


FIG. 14. The real space structure of commensurate twisted bilayer graphene as in Fig. 2 but now with nonzero **d**. The left (right) plot corresponds to AB (BA) stacking. The top (bottom) atoms are represented by dots (circles), the A (B) sublattices in each layer are colored blue (red), and the purple rhombus is a primitive unit cell for $L_- \cap L_+$.

we say that a commensurate configuration has AB (BA) stacking if there is a B (A) sublattice atom on the top layer that is directly above some A (B) sublattice atom on the bottom layer. For the commensurate configuration with $\theta_0 = 0$, it is clear that $\mathbf{d} = \mathbf{0}$ (i.e., no interlayer translation) corresponds to AA stacking, $\mathbf{d} = a_0\hat{\mathbf{y}}$ corresponds to AB stacking, and $\mathbf{d} = -a_0\hat{\mathbf{y}}$ corresponds to BA stacking. We will now derive a generalization of this correspondence for commensurate configurations with 3|n.

We first consider AA stacking. In this case, there is a pair of vectors $\mathbf{r}_+ \in L_+$ and $\mathbf{r}_- \in L_-$ such that $\mathbf{r}_+ + \boldsymbol{\tau}_A^+ = \mathbf{r}_- + \boldsymbol{\tau}_A^-$. Equivalently, we have $\boldsymbol{\tau}_A^+ - \boldsymbol{\tau}_A^- \in L_- + L_+$. Using Eq. (D40), we have

$$\boldsymbol{\tau}_{A}^{+} - \boldsymbol{\tau}_{A}^{-} = \left(R_{-\theta_{0}/2} \boldsymbol{\tau}_{A} - \mathbf{d}/2 \right) - \left(R_{\theta_{0}/2} \boldsymbol{\tau}_{A} + \mathbf{d}/2 \right) \\
= - \left(R_{\theta_{0}/2} - R_{-\theta_{0}/2} \right) (a_{0} \hat{\mathbf{y}}) - \mathbf{d} \\
= 2 \sin(\theta_{0}/2) (a_{0} \hat{\mathbf{x}}) - \mathbf{d} \\
= \frac{2n}{\sqrt{d_{0}N}} a_{0} \hat{\mathbf{x}} - \mathbf{d} \\
= n' \mathbf{a}_{1} / \sqrt{N} - \mathbf{d}, \tag{D44}$$

where $n'=2n/\sqrt{3d_0}$ is an integer since 3|n and $d_0 \in \{3,12\}$ by Eq. (D13). Since we found in Appendix D 5 that $L_- + L_+ = L/\sqrt{N}$ we see that $\tau_A^+ - \tau_A^- \in L_- + L_+$ if and only if $\mathbf{d} \in L_- + L_+$. We conclude that AA stacking corresponds to $\mathbf{d} \in L_- + L_+$. Since $\tau_B = R_{-\pi/3}\tau_A$ and $\mathbf{a}_2 = R_{-\pi/3}\mathbf{a}_1$ we have

$$\boldsymbol{\tau}_{B}^{+} - \boldsymbol{\tau}_{B}^{-} = n' \mathbf{a}_{2} / \sqrt{N} - \mathbf{d}$$
 (D45)

so that $\tau_B^+ - \tau_B^- \in L_- + L_+$ if and only if $\mathbf{d} \in L_- + L_+$. It follows that AA stacking can equivalently be defined by saying that there is a B sublattice atom on the top layer that is directly above some B sublattice atom on the bottom layer. A commensurate configuration with AA stacking is shown in Fig. 2.

Next, we consider AB and BA stacking. In AB stacking, there are vectors $\mathbf{r}_l \in L_l$ such that $\mathbf{r}_+ + \boldsymbol{\tau}_B^+ = \mathbf{r}_- + \boldsymbol{\tau}_A^-$, or equivalently $\boldsymbol{\tau}_B^+ - \boldsymbol{\tau}_A^- \in L_- + L_+$. Similarly, BA stacking is equivalent to $\boldsymbol{\tau}_A^+ - \boldsymbol{\tau}_B^- \in L_- + L_+$. Using Eqs. (D39) and (D40), we have

$$\tau_{A}^{l} - \tau_{B}^{-l} = -(R_{l\theta_{0}/2}\tau_{B} - R_{-l\theta_{0}/2}\tau_{A}) - l\mathbf{d}
= -R_{-\pi/6}(R_{(l\theta_{0}-\pi/3)/2} - R_{-(l\theta_{0}-\pi/3)/2})\tau_{A} - l\mathbf{d}
= 2\sin((l\theta_{0}-\pi/3)/2)R_{-\pi/6}(a_{0}\hat{\mathbf{x}}) - l\mathbf{d}
= (l\sin(\theta_{0}/2)\sqrt{3} - \cos(\theta_{0}/2))(\tau_{B} - \tau_{A}) - l\mathbf{d}
= -m'(\tau_{B} - \tau_{A})/\sqrt{N} - l\mathbf{d},$$
(D46)

where $m' = (m - ln)/\sqrt{d_0/3}$ is an integer with m' = s (mod 3) by Eq. (D43). It follows that $\boldsymbol{\tau}_A^l - \boldsymbol{\tau}_B^{-l} \in L_- + L_+$ if and only if $\mathbf{d} \in -\frac{lsa_0}{\sqrt{N}}\mathbf{\hat{y}} + L_- + L_+$ so that AB stacking corresponds to $\mathbf{d} \in \frac{s}{\sqrt{N}}a_0\mathbf{\hat{y}} + L_- + L_+$ and BA stacking corresponds to $\mathbf{d} \in -\frac{s}{\sqrt{N}}a_0\mathbf{\hat{y}} + L_- + L_+$. Commensurate configurations with AB and BA stacking are shown in Fig. 14.

APPENDIX E: $L_- + L_+$ and $P_- + P_+$ ARE DENSE FOR INCOMMENSURATE θ

Suppose θ is an incommensurate angle. Recall from Appendix D 1 that this implies x_0 and y_0 are not both rational. It follows from Eq. (D4) that both columns and both rows of the matrix $a^{-1}R_{\theta}a$ contain an irrational value. It is well known that for any irrational number z, the set of fractional parts of integer multiples of z is dense in the interval [0, 1). Equivalently, the set of integer linear combinations of 1 and z is dense in \mathbb{R} . It follows that he set of integer linear combinations of $a^{-1}R_{\theta}a\hat{\mathbf{x}}$, $a^{-1}R_{\theta}a\hat{\mathbf{y}}$, $\hat{\mathbf{x}}$, $\hat{\mathbf{y}}$ is dense in \mathbb{R}^2 . Since the linear map $R_{-\theta/2}a$ is continuous and density is preserved under continuous maps, we conclude that $L_- + L_+$ is dense in \mathbb{R}^2 . A similar argument using Eq. (D5) shows that $P_- + P_+$ is dense in \mathbb{R}^2 as well.

APPENDIX F: PROPERTIES OF THE DISTANCE FUNCTION d

- (1) We consider 1 in Sec. II C which claims $d(\mathbf{k}, l, \mathbf{k}, l) = 0$. If we write $\mathbf{k} + \mathbf{G}_l = \mathbf{k} + \mathbf{G}_{-l}$ where $\mathbf{G}_l = \mathbf{G}_{-l} = \mathbf{0}$, we then have $d(\mathbf{k}, l, \mathbf{k}, l) = |\mathbf{G}_{-l}| = 0$.
- (2) We consider 2 in Sec. II C which claims $d(\mathbf{k}, l, \mathbf{k}', l') = d(\mathbf{k}', l', \mathbf{k}, l)$. If $\mathbf{k}' \mathbf{k} \notin P_- + P_+$ then $d(\mathbf{k}, l, \mathbf{k}', l') = \infty = d(\mathbf{k}', l', \mathbf{k}, l)$. Otherwise, suppose $\mathbf{k} + \mathbf{G}_l = \mathbf{k}' + \mathbf{G}_{-l}$ for some $\mathbf{G}_- \in P_-$, $\mathbf{G}_+ \in P_+$. There are two cases to consider.

(i) If
$$l' = -l$$
 then $\mathbf{k}' + \mathbf{G}_{l'} = \mathbf{k} + \mathbf{G}_{-l'}$ so that
$$d(\mathbf{k}, l, \mathbf{k}', l') = |\mathbf{k} + \mathbf{G}_{l}| = |\mathbf{k}' + \mathbf{G}_{l'}|$$

$$= d(\mathbf{k}', l', \mathbf{k}, l).$$
(F1)

(ii) If l' = l then $\mathbf{k}' - \mathbf{G}_{l'} = \mathbf{k} - \mathbf{G}_{-l'}$ so that

$$d(\mathbf{k}, l, \mathbf{k}', l') = |\mathbf{G}_{-l}| = |-\mathbf{G}_{-l'}| = d(\mathbf{k}', l', \mathbf{k}, l).$$
 (F2)

(3) We consider 3 in Sec. II C which claims

$$d(\mathbf{k}, l, \mathbf{k}'', l'') \le d(\mathbf{k}, l, \mathbf{k}', l') + d(\mathbf{k}', l', \mathbf{k}'', l'').$$
 (F3)

When either term on the right-hand side is ∞ , the inequality is trivially satisfied. If the left-hand side is ∞ then $\mathbf{k''} - \mathbf{k} \notin P_- + P_+$. This implies that at least one of the terms on the right-hand side must be ∞ as well, so the inequality is satisfied

Otherwise, suppose

$$\mathbf{k} + \mathbf{G}_{l} = \mathbf{k}' + \mathbf{G}_{-l},$$

$$\mathbf{k}' + \mathbf{G}'_{l'} = \mathbf{k}'' + \mathbf{G}'_{-l'}$$
 (F4)

for some $G_-, G'_- \in P_-$ and $G_+, G'_+ \in P_+$. It follows that

$$\mathbf{k} + \mathbf{G}_l + \mathbf{G}'_{l'} = \mathbf{k}'' + \mathbf{G}_{-l} + \mathbf{G}'_{-l'}.$$
 (F5)

We now consider three cases.

(a) Suppose l = l' = l'' and without loss of generality we take l = l' = l'' = +. Then $d(\mathbf{k}, l, \mathbf{k}', l') = |\mathbf{G}_{-}|$, $d(\mathbf{k}', l', \mathbf{k}'', l'') = |\mathbf{G}'_{-}|$ and $\mathbf{k} + \mathbf{G}''_{-} = \mathbf{k}'' + \mathbf{G}''_{-}$, where

$$G''_{-} = G_{-} + G'_{-},$$

 $G''_{+} = G_{+} + G'_{+}.$ (F6)

We then have

$$d(\mathbf{k}, l, \mathbf{k}'', l'') = |\mathbf{G}''_{-}|$$

$$= |\mathbf{G}_{-} + \mathbf{G}'_{-}|$$

$$\leq d(\mathbf{k}, l, \mathbf{k}', l') + d(\mathbf{k}', l', \mathbf{k}'', l''). \quad (F7)$$

(b) Suppose $l=l'\neq l''$ and without loss of generality we take l=l'=+, l''=-. Then $d(\mathbf{k},l,\mathbf{k}',l')=|\mathbf{G}_{-}|$, $d(\mathbf{k}',l',\mathbf{k}'',l'')=|\mathbf{k}''+\mathbf{G}'_{-}|$ and $\mathbf{k}+\mathbf{G}''_{l}=\mathbf{k}''+\mathbf{G}''_{-l}$, where

$$\mathbf{G}''_{-} = \mathbf{G}_{-} + \mathbf{G}'_{-},$$

 $\mathbf{G}''_{+} = \mathbf{G}_{+} + \mathbf{G}'_{+}.$ (F8)

We then have

$$d(\mathbf{k}, l, \mathbf{k}'', l'') = |\mathbf{k}'' + \mathbf{G}''_{-}|$$

$$= |\mathbf{G}_{-} + (\mathbf{k}'' + \mathbf{G}'_{-})|$$

$$\leq d(\mathbf{k}, l, \mathbf{k}', l') + d(\mathbf{k}', l', \mathbf{k}'', l''). \quad (F9)$$

(c) Suppose $l=l''\neq l'$ and without loss of generality we take l=l''=+, l'=-. Then $d(\mathbf{k},l,\mathbf{k}',l')=|\mathbf{k}'+\mathbf{G}_-|$, $d(\mathbf{k}',l',\mathbf{k}'',l'')=|\mathbf{k}'+\mathbf{G}'_-|$ and $\mathbf{k}+\mathbf{G}''=\mathbf{k}''+\mathbf{G}''_-|$, where

$$\mathbf{G}''_{-} = \mathbf{G}_{-} - \mathbf{G}'_{-},$$
 $\mathbf{G}''_{-} = \mathbf{G}_{+} - \mathbf{G}'_{+}.$ (F10)

We then have

$$d(\mathbf{k}, l, \mathbf{k}'', l'') = |\mathbf{G}''_{-}|$$

$$= |\mathbf{G}_{-} - \mathbf{G}'_{-}|$$

$$= |(\mathbf{k}' + \mathbf{G}_{-}) - (\mathbf{k}' + \mathbf{G}'_{-})|$$

$$\leq d(\mathbf{k}, l, \mathbf{k}', l') + d(\mathbf{k}', l', \mathbf{k}'', l''). (F11)$$

The last case in which $l \neq l' = l''$ follows from the symmetry of d and the case $l = l' \neq l''$.

APPENDIX G: LEVEL SETS OF d

In this section, we prove the characterization of d described in Sec. II D. Recall that $P_{\pm}^0 = R_{-l\theta_0/2}P$ and that $\theta = \theta_0 + \delta\theta$ is an incommensurate angle, where θ_0 is a commensurate angle and $\delta\theta$ is small. Let $\mathbf{k} \in \mathbb{R}^2$, $l \in \{+, -\}$, and let $\mathbf{k}_0 = R_{l\delta\theta/2}\mathbf{k}$. Suppose that \mathbf{k}', l' satisfy $d(\mathbf{k}, l, \mathbf{k}', l') < \infty$ so that we can write $\mathbf{k} + \mathbf{G}_l = \mathbf{k}' + \mathbf{G}_{-l}$ for unique vectors $\mathbf{G}_- \in P_-$, $\mathbf{G}_+ \in P_+$. Define $\mathbf{G}_+^0 = R_{\pm\delta\theta/2}\mathbf{G}_\pm \in P_\pm^0$ and $\mathbf{k}_0' = \mathbf{k}_0 + \mathbf{G}_l^0 - \mathbf{G}_{-l}^0 \in \mathbf{k}_0 + P_-^0 + P_+^0$. We then have

$$\mathbf{k}' - R_{l\delta\theta/2}\mathbf{k}'_0 = (\mathbf{k} + \mathbf{G}_l - \mathbf{G}_{-l}) - R_{l\delta\theta/2}(\mathbf{k}_0 + \mathbf{G}_l^0 - \mathbf{G}_{-l}^0)$$

$$= R_{-l\delta\theta/2}(\mathbf{k}_0 + \mathbf{G}_l^0) - R_{l\delta\theta/2}(\mathbf{k}_0 + \mathbf{G}_l^0)$$

$$= -lD(\delta\theta)\mathbf{Q}_{-l}, \tag{G1}$$

where $D(\delta\theta)$ is defined by Eq. (19) and

$$\mathbf{Q}_{-l} = \mathbf{k}_{0} + \mathbf{G}_{l}^{0} = \mathbf{k}_{0}' + \mathbf{G}_{-l}^{0} \in (\mathbf{k}_{0} + P_{l}^{0}) \cap (\mathbf{k}_{0}' + P_{-l}^{0})$$

$$= \mathcal{Q}(\mathbf{k}_{0}, l, \mathbf{k}_{0}', -l). \tag{G2}$$

Similarly,

$$\mathbf{k}' - R_{-l\delta\theta/2}\mathbf{k}'_0 = (\mathbf{k} + \mathbf{G}_l - \mathbf{G}_{-l}) - R_{-l\delta\theta/2}(\mathbf{k}_0 + \mathbf{G}_l^0 - \mathbf{G}_{-l}^0)$$

$$= R_{-l\delta\theta/2}\mathbf{G}_{-l}^0 - R_{l\delta\theta/2}\mathbf{G}_{-l}^0$$

$$= -lD(\delta\theta)\mathbf{Q}_l, \tag{G3}$$

where

$$\mathbf{Q}_{l} = \mathbf{G}_{-l}^{0} = \mathbf{k}_{0} - \mathbf{k}_{0}' + \mathbf{G}_{l}^{0} \in P_{-l}^{0} \cap (\mathbf{k}_{0} - \mathbf{k}_{0}' + P_{l}^{0})$$

$$= \mathcal{Q}(\mathbf{k}_{0}, l, \mathbf{k}_{0}', l). \tag{G4}$$

It follows that

$$\mathbf{k}' = R_{-l'\delta\theta/2}\mathbf{k}_0' - lD(\delta\theta)\mathbf{Q}_{l'},\tag{G5}$$

where $\mathbf{Q}_{l'} \in \mathcal{Q}(\mathbf{k}_0, l, \mathbf{k}_0', l')$. Furthermore, the vectors \mathbf{k}_0' and $\mathbf{Q}_{l'}$ are uniquely determined because the vectors \mathbf{G}_- and \mathbf{G}_+ are uniquely determined. Additionally, since $|\mathbf{Q}_{-l}| = |\mathbf{k}_0 + \mathbf{G}_l^0| = |\mathbf{k} + \mathbf{G}_l|$ and $|\mathbf{Q}_l| = |\mathbf{G}_l^0| = |\mathbf{G}_l|$ we have $d(\mathbf{k}, l, \mathbf{k}', l') = |\mathbf{Q}_{l'}|$. The converse statement

can be proved simply by tracing the above argument backwards.

APPENDIX H: EQUIVALENCE OF SMALL ROTATIONS AND SPATIALLY VARYING TRANSLATIONS

We now derive Eqs. (47) and (48) which relate the T and S^l potentials in commensurate and incommensurate configurations. In this section, we denote continuum states $|\mathbf{p}, l, \alpha\rangle_c$ and $|\mathbf{r}, l, \alpha\rangle_c$ with twist angle $\theta = \theta_0 + \delta\theta$ and translation vector \mathbf{d} by $|\mathbf{p}, l, \alpha, \delta\theta, \mathbf{d}\rangle_c$ and $|\mathbf{r}, l, \alpha, \delta\theta, \mathbf{d}\rangle_c$, respectively. Since $|\mathbf{p}, l, \alpha, 0, \mathbf{d}\rangle_c$ is a state with crystal momentum $\mathbf{K}_l + \mathbf{p}$ which has been shifted by $-l\mathbf{d}/2$ we must have

$$|\mathbf{p}, l, \alpha, 0, \mathbf{d}\rangle_c = e^{-il(\mathbf{K}_l + \mathbf{p}) \cdot \mathbf{d}/2} |\mathbf{p}, l, \alpha, 0, \mathbf{0}\rangle_c.$$
 (H1)

Similarly, since $|\mathbf{p}, l, \alpha, \delta\theta, \mathbf{0}\rangle_c$ is a momentum state that has been rotated by $-l\delta\theta/2$, we must have

$$|\mathbf{p}, l, \alpha, \delta\theta, \mathbf{0}\rangle_c = |R_{l\delta\theta/2}\mathbf{p}, l, \alpha, 0, \mathbf{0}\rangle_c$$
. (H2)

By Eq. (40), we then have

$$|\mathbf{r}, l, \alpha, 0, \mathbf{d}\rangle = e^{-il\mathbf{K}_l \cdot \mathbf{d}/2} |\mathbf{r} + l\mathbf{d}/2, l, \alpha, 0, \mathbf{0}\rangle,$$

$$|\mathbf{r}, l, \alpha, \delta\theta, \mathbf{0}\rangle = |R_{l\delta\theta/2}\mathbf{r}, l, \alpha, 0, \mathbf{0}\rangle,$$
(H3)

so that Eq. (45) implies

$$|\mathbf{r}, l, \alpha, \delta\theta, \mathbf{0}\rangle = e^{il\mathbf{K}_l \cdot D(\delta\theta)\mathbf{r}/2} |\mathbf{r}, l, \alpha, 0, D(\delta\theta)\mathbf{r}\rangle + O(\delta\theta^2).$$
(H4)

Next, let the continuum Hamiltonian \tilde{H} with twist angle $\theta = \theta_0 + \delta\theta$ and translation vector \mathbf{d} be denoted $\tilde{H}(\delta\theta, \mathbf{d})$. Since the pattern of atoms near position \mathbf{r} with $\theta = \theta_0 + \delta\theta$ and $\mathbf{d} = \mathbf{0}$ is the same to first order in $\delta\theta$ as the pattern with $\theta = \theta_0$ and $\mathbf{d} = D(\delta\theta)\mathbf{r}$, we must have

$$\langle \mathbf{r}', l', \alpha', \delta\theta, \mathbf{0}|_{c} \tilde{H}(\delta\theta, \mathbf{0}) | \mathbf{r}, l, \alpha, \delta\theta, \mathbf{0} \rangle_{c}$$

$$= \langle \mathbf{r}', l', \alpha', \delta\theta, \mathbf{0}|_{c} \tilde{H}(0, D(\delta\theta)\mathbf{r}) | \mathbf{r}, l, \alpha, \delta\theta, \mathbf{0} \rangle_{c}$$

$$+ O(\delta\theta^{2}). \tag{H5}$$

It follows that

$$T(\mathbf{r}, \delta\theta, \mathbf{0}) = (\langle \mathbf{r}, +, A, \delta\theta, \mathbf{0} |_{c} \quad \langle \mathbf{r}, +, B, \delta\theta, \mathbf{0} |_{c}) \tilde{H}(\delta\theta, \mathbf{0}) \begin{pmatrix} |\mathbf{r}, -, A, \delta\theta, \mathbf{0} \rangle_{c} \\ |\mathbf{r}, -, B, \delta\theta, \mathbf{0} \rangle_{c} \end{pmatrix}$$

$$= e^{-i(\mathbf{K}_{-} + \mathbf{K}_{+}) \cdot D(\delta\theta)\mathbf{r}/2} (\langle \mathbf{r}, +, A, 0, D(\delta\theta)\mathbf{r} |_{c} \quad \langle \mathbf{r}, +, B, 0, D(\delta\theta)\mathbf{r} |_{c}) \tilde{H}(0, D(\delta\theta)\mathbf{r}) \begin{pmatrix} |\mathbf{r}, -, A, 0, D(\delta\theta)\mathbf{r} \rangle_{c} \\ |\mathbf{r}, -, B, 0, D(\delta\theta)\mathbf{r} \rangle_{c} \end{pmatrix} + O(\delta\theta^{2})$$

$$= e^{-i\cos(\theta/2)\mathbf{K} \cdot D(\delta\theta)\mathbf{r}} T(\mathbf{r}, 0, D(\delta\theta)\mathbf{r}) + O(\delta\theta^{2}), \tag{H6}$$

which is equivalent to Eq. (47). Equation (48) follows from a similar calculation.

APPENDIX I: SYMMETRY REPRESENTATIONS

In this section, we give the representations of the unitary and antiunitary symmetries of twisted bilayer graphene referred to in Sec. III. For $\theta \neq 0$, the spinless symmetries of the full Hamiltonian are generated by the unitary operators C_{6z} (rotation by $\pi/3$ about $\hat{\mathbf{z}}$), C_{2x} (rotation by π about $\hat{\mathbf{x}}$), and the antiunitary operator \mathcal{T} (time reversal). These operators take the form

$$C_{6z} |\mathbf{k}, l, \alpha\rangle = |R_{\pi/3}\mathbf{k}, l, -\alpha\rangle,$$

$$C_{2x} |\mathbf{k}, l, \alpha\rangle = -|R^{x}\mathbf{k}, -l, -\alpha\rangle,$$

$$\mathcal{T} |\mathbf{k}, l, \alpha\rangle = |-\mathbf{k}, l, \alpha\rangle,$$
(I1)

where R^x denotes reflection across the x axis. The minus sign for C_{2x} reflects the fact that $|\mathbf{r}, l, \alpha\rangle$ are p_z orbitals. The symmetry subgroup preserving valley is generated by $C_{2z}\mathcal{T}$, C_{3z} , and C_{2x} , where $C_{2z} = C_{6z}^3$ and $C_{3z} = C_{6z}^2$. Using Eq. (4), we find

$$C_{2z}\mathcal{T} |\mathbf{K}_{l} + \mathbf{p}, l, \alpha\rangle = |\mathbf{K}_{l} + \mathbf{p}, l, -\alpha\rangle,$$

$$C_{3z} |\mathbf{K}_{l} + \mathbf{p}, l, \alpha\rangle = e^{i(2\pi/3)\alpha} |\mathbf{K}_{l} + R_{2\pi/3}\mathbf{p}, l, \alpha\rangle,$$

$$C_{2x} |\mathbf{K}_{l} + \mathbf{p}, l, \alpha\rangle = -|\mathbf{K}_{-l} + R^{x}\mathbf{p}, -l, -\alpha\rangle.$$
(I2)

As a result, the appropriate representations on the $|\mathbf{p},l,\alpha\rangle_c$ space are

$$C_{2z}\mathcal{T}|\mathbf{p}\rangle_{c} = |\mathbf{p}\rangle_{c} \begin{pmatrix} \sigma_{x} & 0\\ 0 & \sigma_{x} \end{pmatrix},$$

$$C_{3z}|\mathbf{p}\rangle_{c} = |R_{2\pi/3}\mathbf{p}\rangle_{c} \begin{pmatrix} e^{i(2\pi/3)\sigma_{z}} & 0\\ 0 & e^{i(2\pi/3)\sigma_{z}} \end{pmatrix}, \quad (I3)$$

$$C_{2x}|\mathbf{p}\rangle_{c} = |R^{x}\mathbf{p}\rangle_{c} \begin{pmatrix} 0 & -\sigma_{x}\\ -\sigma_{x} & 0 \end{pmatrix},$$

where $|\mathbf{p}\rangle_c$ is defined in Eq. (29).

In the case $\theta = 0$, there is an additional valley preserving unitary symmetry M_y (reflection across the xz plane). This operator has representations

$$M_{y} | \mathbf{k}, l, \alpha \rangle = | R^{x} \mathbf{k}, l, -\alpha \rangle ,$$

$$M_{y} | \mathbf{K} + \mathbf{p}, l, \alpha \rangle = | \mathbf{K} + R^{x} \mathbf{p}, l, -\alpha \rangle ,$$

$$M_{y} | \mathbf{p} \rangle_{c} = | R^{x} \mathbf{p} \rangle_{c} \begin{pmatrix} \sigma_{x} & 0 \\ 0 & \sigma_{x} \end{pmatrix} .$$
(I4)

For θ near 0, M_{ν} can be considered an approximate symmetry.

APPENDIX J: DETERMINING THE MODEL PARAMETERS WHEN $\delta\theta=0$

Recall from Sec. IIE that in the commensurate case, the continuum Hamiltonian approximates the four bands of H nearest the Fermi level at charge neutrality. Explicitly, this

model takes the form of a \mathbf{p} dependent 4×4 matrix as shown in Eq. (59). In order to determine the parameters for this model, we will now describe a method to determine an effective Hamiltonian for these four bands directly from the microscopic Hamiltonian H.

Recall from Sec. IIB that for commensurate configurations, H is block diagonal with blocks of dimension 4N. Let $H(\mathbf{p})$ be the Hamiltonian block containing Bloch states $|\mathbf{K}_l + \mathbf{p}, l, \alpha\rangle$ for $l \in \{+, -\}$, $\alpha \in \{A, B\}$. In practice, the $4N \times 4N$ matrix representation for $H(\mathbf{p})$ can be computed accurately from Eqs. (6) and (9) with finitely many terms for each sum as long as the hopping functions $t_+(\mathbf{r})$ and $\hat{t}_-(\mathbf{k})$ decay rapidly enough. We diagonalize $H(\mathbf{p})$ as

$$H(\mathbf{p}) = \sum_{j=1}^{4N} E_j(\mathbf{p}) |\mathbf{p}, j\rangle \langle \mathbf{p}, j|$$
 (J1)

for real eigenvalues $E_1(\mathbf{p}) \leqslant E_2(\mathbf{p}) \leqslant \cdots \leqslant E_{4N}(\mathbf{p})$ and orthonormal eigenvectors $|\mathbf{p}, j\rangle$. The indices j from 2N-1 to 2N+2 correspond to the four bands described by the continuum Hamiltonian.

Define the projection operators

$$P_0(\mathbf{p}) = \sum_{l=\pm} \sum_{\alpha=\pm} |\mathbf{K}_l + \mathbf{p}, l, \alpha\rangle \langle \mathbf{K}_l + \mathbf{p}, l, \alpha|,$$

$$P_1(\mathbf{p}) = \sum_{j=2N-1}^{2N+2} |\mathbf{p}, j\rangle \langle \mathbf{p}, j|.$$
 (J2)

Since the states $|\mathbf{p}, j\rangle$ are almost completely supported on the states $|\mathbf{K}_l + \mathbf{p}, l, \alpha\rangle$, the operators $P_0(\mathbf{p})$ and $P_1(\mathbf{p})$ are nearly the same. It follows that there is a canonical unitary operator $U(\mathbf{p})$ called the direct rotation that satisfies

$$U(\mathbf{p})P_1(\mathbf{p})U^{\dagger}(\mathbf{p}) = P_0(\mathbf{p}) \tag{J3}$$

and minimizes the Frobenius norm of $U(\mathbf{p})-I$ over all unitary operators satisfying Eq. (J3) [97]. The only condition upon which this theorem is dependent is $||P_0(\mathbf{p})-P_1(\mathbf{p})||_{op} < 1$, which is satisfied in practice. Here, we use the notation $||M||_{op}$ to denote the operator norm of M. The direct rotation is given explicitly by

$$U(\mathbf{p}) = \sqrt{(I - 2P_0(\mathbf{p}))(I - 2P_1(\mathbf{p}))},$$
 (J4)

where \sqrt{M} denotes the operator square root of M and is defined using a branch cut of the function $z \mapsto \sqrt{z}$ along the negative real axis in the complex plane, with $\sqrt{1} = 1$. The operator

$$H_{\text{eff}}(\mathbf{p}) = \sum_{j=2N-1}^{2N+2} E_j(\mathbf{p}) U(\mathbf{p}) |\mathbf{p}, j\rangle \langle \mathbf{p}, j| U^{\dagger}(\mathbf{p})$$
 (J5)

is the result of projecting $H(\mathbf{p})$ onto the four bands of interest and then applying the direct rotation into the subspace spanned by the Bloch states $|\mathbf{K}_l + \mathbf{p}, l, \alpha\rangle$. Under the mapping $|\mathbf{K}_l + \mathbf{p}, l, \alpha\rangle \mapsto |\mathbf{p}, l, \alpha\rangle_c$, $H_{\text{eff}}(\mathbf{p})$ maps to an operator that should be considered the correct continuum Hamiltonian.

Let $\mathcal{H}_{\text{eff}}(\mathbf{p})$ be the 4×4 matrix representation of $H_{\text{eff}}(\mathbf{p})$ with respect to the basis $|\mathbf{K}_l + \mathbf{p}, l, \alpha\rangle$ so that $\mathcal{H}_{\text{eff}}(\mathbf{p})$ is

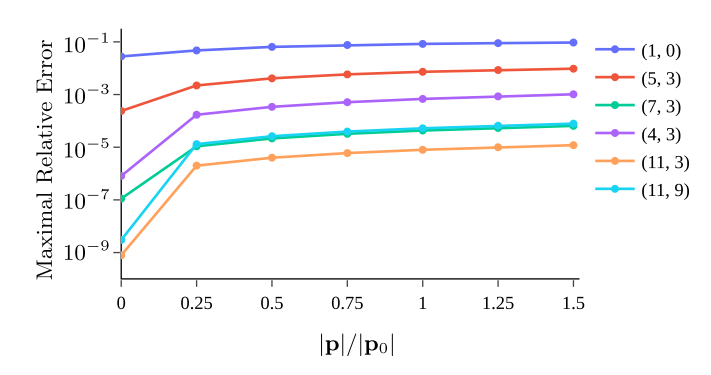


FIG. 15. The maximal relative error between $\mathcal{H}_{\rm eff}(\mathbf{p})$ and $\mathcal{H}_0(\mathbf{p})$ as a function of $|\mathbf{p}|/|\mathbf{p}_0|$, where $\hbar v_F |\mathbf{p}_0| = 3|w_0|$ [see Eq. (J7)]. The maximum is taken over \mathbf{d} in a 10×10 discretization of a unit cell of $2L/\sqrt{N}$ and five values of \mathbf{p} with a given norm.

directly comparable to the matrix $\mathcal{H}_0(\mathbf{p})$ defined in Eq. (59). These two matrices are explicitly dependent on \mathbf{p} , but also implicitly dependent on the translation vector \mathbf{d} . Recall from Appendix D 6 that $\mathbf{d} = \mathbf{0}$ corresponds to AA stacking, $\mathbf{d} = \frac{s}{\sqrt{N}} a_0 \hat{\mathbf{y}}$ corresponds to AB stacking, and $\mathbf{d} = -\frac{s}{\sqrt{N}} a_0 \hat{\mathbf{y}}$ corresponds to BA stacking. By Eqs. (57) and (60), we have

$$T_0(\mathbf{0}) = 3w_0 e^{i\chi_0 \sigma_z},$$

$$T_0(\pm \mathbf{d}_{AB}) = \frac{3}{2} w_1(\sigma_x \mp i\sigma_y),$$
 (J6)

where $\mathbf{d}_{AB} = \frac{s}{\sqrt{N}} a_0 \hat{\mathbf{y}}$ so that w_0 , χ_0 , w_2 determine $\mathcal{H}_0(\mathbf{p})$ for AA stacking configurations, while w_1 , w_2 determine $\mathcal{H}_0(\mathbf{p})$ for AB and BA stacking configurations. Furthermore, to determine the model parameters, it suffices to compare $\mathcal{H}_{\text{eff}}(\mathbf{p})$ and $\mathcal{H}_0(\mathbf{p})$ at $\mathbf{p} = \mathbf{0}$ and a single generic \mathbf{d} value. For simplicity, we instead use $\mathbf{p} = \mathbf{0}$ and both $\mathbf{d} = \mathbf{0}$ and $\mathbf{d} = \mathbf{d}_{AB}$ to determine the model parameters shown in Tables I and II. These computations are performed using the hopping functions $t_{\pm}(\mathbf{r})$ given in Appendix K.

To validate the accuracy of these results, we compute the relative error

$$\frac{||\mathcal{H}_{eff}(\mathbf{p}) - \mathcal{H}_{0}(\mathbf{p})||}{||\mathcal{H}_{eff}(\mathbf{p})||} \tag{J7}$$

using the parameters in Table II, where ||M|| denotes the Frobenius norm of M. We compute this relative error as a function of **d** and **p**, where **d** varies over a unit cell of $2L/\sqrt{N}$ (recalling from Sec. IIE that both H and \tilde{H} are periodic up to unitary equivalence with respect to L/\sqrt{N}), and $|\mathbf{p}|$ varies from 0 to $3|\mathbf{p}_0|/2$ where $\hbar v_F|\mathbf{p}_0|=3|w_0|$ (see Fig. 5). Specifically, for each value of $|\mathbf{p}|$, we compute the maximal relative error for **d** in a 10×10 discretization of a unit cell of $2L/\sqrt{N}$ and for five values of **p** with the given magnitude. The results are shown in Fig. 15 for the first 6 commensurate configurations. The relative errors for all configurations other than (m, n) = (1, 0) (and $\theta_0 = 0^\circ$) are less than 10^{-2} for all $|\mathbf{p}|$ values considered and are less than $10^{-3.5}$ for $\mathbf{p} = \mathbf{0}$. The relative errors for (m, n) = (1, 0) are larger but still bounded by 10^{-1} for all $|\mathbf{p}|$ values considered, and the relative error at $\mathbf{p} = \mathbf{0}$ is less than 0.03. We conclude that \tilde{H} is an accurate model for the four bands of H nearest the Fermi level at

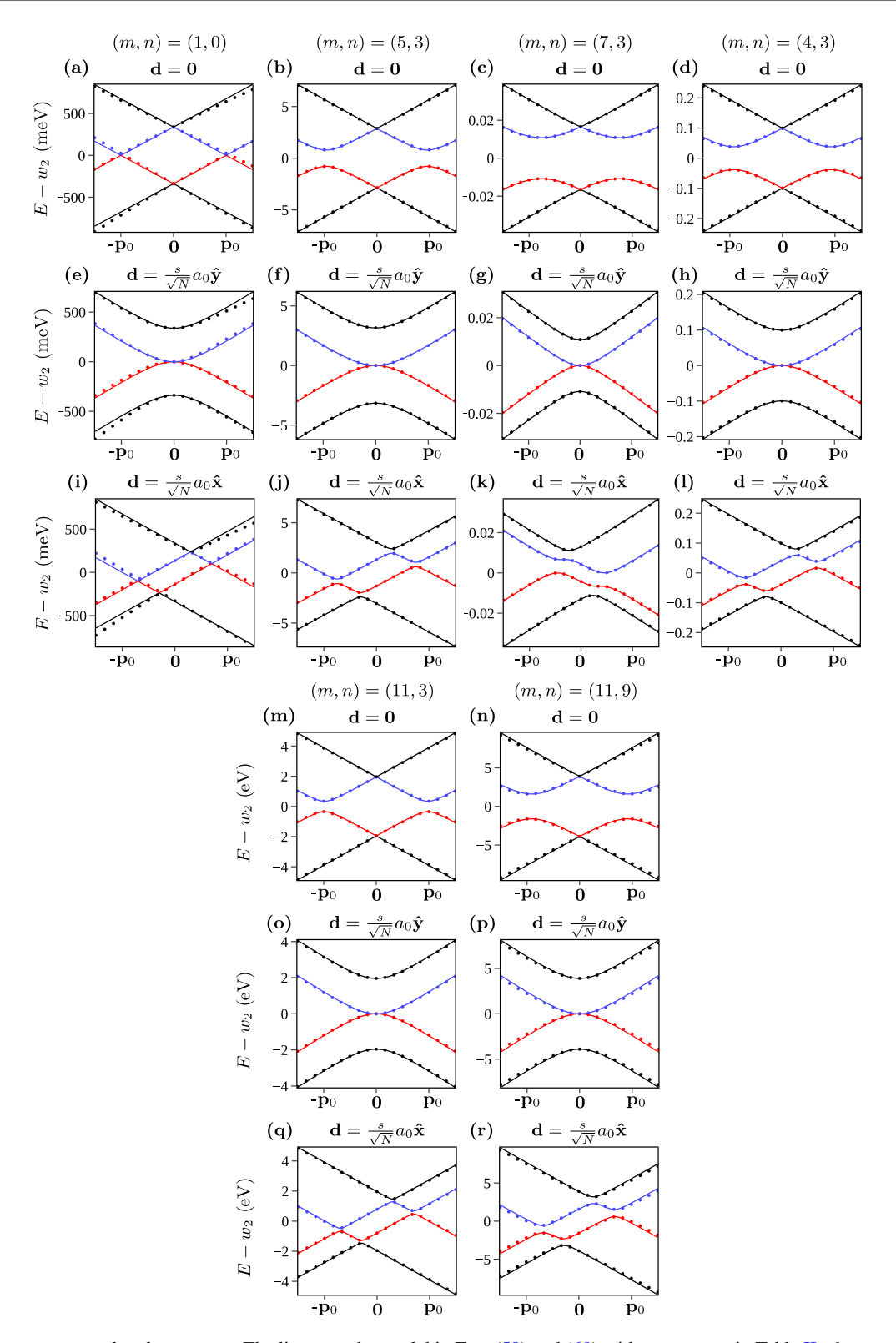


FIG. 16. Commensurate band structures. The lines use the model in Eqs. (59) and (60) with parameters in Table II whereas the dots use the microscopic Hamiltonian in Eqs. (6) and (9). The vector \mathbf{p} ranges linearly from $-3\mathbf{p}_0/2$ to $3\mathbf{p}_0/2$, where $\hbar v_F \mathbf{p}_0 = 3|w_0|\hat{\mathbf{x}}$. Recall that $\mathbf{d} = \mathbf{0}$ and $\mathbf{d} = \frac{s}{\sqrt{N}} a_0 \hat{\mathbf{y}}$ correspond to AA and AB stacking, respectively.

charge neutrality for all \mathbf{d} and small \mathbf{p} . Figure 16 compares the eigenvalues of $\mathcal{H}_{eff}(\mathbf{p})$ and $\mathcal{H}_0(\mathbf{p})$ for each commensurate configuration in Table II as a function of \mathbf{p} for three values of \mathbf{d} .

APPENDIX K: $t_{\pm}(\mathbf{r})$ FUNCTIONS

Following Ref. [77], we take

$$t_{+}(\mathbf{r}) = A_0 e^{(a_0 - |\mathbf{r}|)/\delta_0},$$

(m, n)	θ_0	N	S	Χο	(w_0, w_1, w_2) in μ eV	$\delta \theta_{ m magic}$ in microdegrees
(1, 0)	0°	1	1	0.0°	(112682.504, 112682.504, 0.0)	1255782.99
(5, 3)	38.2132107°	7	1	-3.09972641°	(958.62462, 1051.57009, -4444.6652)	4421.48495
(7, 3)	27.7957725°	13	-1	125.164435°	(5.5027, 3.61749, -4431.53104)	9.96025
(4, 3)	46.8264489°	19	1	-0.993893031°	(33.1618, 33.19161, -4320.05111)	83.97407
(11, 3)	17.8965511°	31	1	1.23811361°	(0.65302, 0.65326, -4426.40937)	1.31881
(11, 9)	50.5699921°	37	1	-0.861668226°	(1.29978, 1.30022, -4026.88676)	2.34902

TABLE II. Numerically determined model parameters reported with nine significant figures.

$$t_{-}(\mathbf{r}) = A_{0}e^{(a_{0} - \sqrt{|\mathbf{r}|^{2} + r_{z}^{2}})/\delta_{0}} \frac{|\mathbf{r}|^{2}}{|\mathbf{r}|^{2} + r_{z}^{2}} + B_{0}e^{(r_{z} - \sqrt{|\mathbf{r}|^{2} + r_{z}^{2}})/\delta_{0}} \frac{r_{z}^{2}}{|\mathbf{r}|^{2} + r_{z}^{2}},$$
 (K1)

where $A_0 = -2.7 \,\mathrm{eV}$ and $B_0 = 0.48 \,\mathrm{eV}$ are transfer integrals, $r_z = 2.36 a_0$ is the interlayer spacing, and $\delta_0 = 0.318 a_0$ is chosen so that $t_+(\mathbf{a}_1) \approx t_+(\boldsymbol{\tau}_B - \boldsymbol{\tau}_A)/10$. Using Eqs. (6) and (7), we find

$$\hbar v_F / a_0 \approx 3.68423316 \,\text{eV}.$$
 (K2)

APPENDIX L: SIGNS OF THE PARAMETERS AND DISCRETE SYMMETRIES

We now consider the continuum Hamiltonian \tilde{H} in Eq. (69) as a function $\tilde{H}(\phi_0, w_0, w_1, w_2, \delta\theta, s)$ of the shown parameters. By Eq. (36), we have

$$\begin{split} \tilde{H}(\phi_0, w_0, w_1, w_2, -\delta\theta, s) \\ &= \tilde{H}(\phi_0, w_0, w_1, w_2, \delta\theta, -s) \\ &= -\tilde{H}(\phi_0, -w_0, -w_1, -w_2, \delta\theta, s). \end{split} \tag{L1}$$

Similarly, by Eq. (71), we have

$$\tilde{H}(\phi_0 + \pi, w_0, w_1, w_2, \delta\theta, s) = \tilde{H}(\phi_0, -w_0, w_1, w_2, \delta\theta, s).$$

Next, we consider the particle hole operator P, first chiral operator C (which is often simply called the "chiral operator" [12] when there is no ambiguity), and second chiral operator C' defined in Ref. [56]

$$P|\mathbf{p}\rangle_{c}' = |-\mathbf{p}\rangle_{c}' \begin{pmatrix} 0 & -I \\ I & 0 \end{pmatrix},$$

$$C|\mathbf{p}\rangle_{c}' = |\mathbf{p}\rangle_{c}' \begin{pmatrix} \sigma_{z} & 0 \\ 0 & \sigma_{z} \end{pmatrix},$$

$$C'|\mathbf{p}\rangle_{c}' = |\mathbf{p}\rangle_{c}' \begin{pmatrix} \sigma_{z} & 0 \\ 0 & -\sigma_{z} \end{pmatrix}.$$
(L3)

These operators act within the **K** valley and the origin of quasimomentum **p** is the Γ_M point of the moiré Brillouin zone. These operators are unitary and satisfy

$$P\tilde{H}(\phi_0, w_0, w_1, w_2, \delta\theta, s)P^{-1}$$

$$= -\tilde{H}(-\phi_0, w_0, w_1, -w_2, \delta\theta, s),$$

$$C\tilde{H}(\phi_0, w_0, w_1, w_2, \delta\theta, s)C^{-1}$$

$$= -\tilde{H}(\phi_0, -w_0, w_1, -w_2, \delta\theta, s),$$

$$C'\tilde{H}(\phi_0, w_0, w_1, w_2, \delta\theta, s)C'^{-1}$$

= $-\tilde{H}(\phi_0, w_0, -w_1, -w_2, \delta\theta, s).$ (L4)

It follows that \tilde{H} is always equivalent up to a sign and a unitary change of basis from the case in which $s=1, 0 \leqslant \phi_0 \leqslant \pi/2$, and $w_0, w_1, \delta\theta \geqslant 0$, so it is sufficient to restrict the parameters in these ranges in calculations.

In particular, we have

$$CP\tilde{H}(\phi_0, w_0, w_1, w_2, \delta\theta, s)(CP)^{-1}$$

= $\tilde{H}(\pi - \phi_0, w_0, w_1, w_2, \delta\theta, s)$. (L5)

Therefore, when $\phi_0 = \pi/2$, the system has a combined *CP* symmetry, although neither *C* nor *P* is a symmetry. Moreover, noting that the *CP* operator map momentum **p** to $-\mathbf{p}$, *CP* symmetry implies that the energy spectrum at $\phi_0 = \pi/2$ is symmetric between **p** and $-\mathbf{p}$, as can be seen in Figs. 10(d)–10(f).

APPENDIX M: WILSON LOOPS AND QUASIMOMENTUM TRUNCATION

In order to make the moiré translation symmetry of the Hamiltonian in Eq. (69) more explicit, we now reparametrize the states $|\mathbf{p}\rangle_c'$ defined in Eq. (68), following the approach of [80]. Note that we can write the moiré quasimomentum $\mathbf{p} + l\mathbf{q}_1$ uniquely in the form $\mathbf{q} + \mathbf{g}_0$ where $\mathbf{q} \in \mathrm{BZ}_M$ and $\mathbf{g}_0 \in D(\delta\theta)\mathcal{Q}_0$. We then have $\mathbf{p} = \mathbf{q} - \mathbf{g}$ where $\mathbf{g} = l\mathbf{q}_1 - \mathbf{g}_0 \in D(\delta\theta)\mathcal{Q}_l$. With this motivation, for $\mathbf{q} \in \mathbb{R}^2$, $\mathbf{g} \in D(\delta\theta)\mathcal{Q}_l$, $l \in \{+, -\}$, and $\alpha \in \{A, B\}$, we define

$$|\mathbf{q}, \mathbf{g}, \alpha\rangle_M = |\mathbf{q} - \mathbf{g}, l, \alpha\rangle_c'$$
 (M1)

where the row vector of states $|\mathbf{p}\rangle_c$ is given in components by

$$|\mathbf{p}\rangle_c' = (|\mathbf{p}, +, A\rangle_c' |\mathbf{p}, +, B\rangle_c' |\mathbf{p}, -, A\rangle_c' |\mathbf{p}, -, B\rangle_c').$$
(M2)

Although the states $|\mathbf{q}, \mathbf{g}, \alpha\rangle_M$ for $\mathbf{q} \in \mathrm{BZ}_M$ form a continuous basis for the Hilbert space, it is useful to define the overcomplete set of states $|\mathbf{q}, \mathbf{g}, \alpha\rangle_M$ for $\mathbf{q} \in \mathbb{R}^2$.

Using this notation, the continuum Hamiltonian can be written

$$\begin{split} \tilde{H} &= \int_{\mathrm{BZ}_{M}} d^{2}\mathbf{q} \sum_{\substack{\mathbf{g}',\mathbf{g} \in \\ D(\delta\theta)(\mathcal{Q}_{-} \cup \mathcal{Q}_{+})}} \sum_{\substack{\alpha',\alpha \in \\ [A,B]}} |\mathbf{q},\mathbf{g}',\alpha'\rangle_{M} \\ &\times \mathcal{H}(\mathbf{q})_{(\mathbf{g}',\alpha'),(\mathbf{g},\alpha)} \langle \mathbf{q},\mathbf{g},\alpha|_{M}, \end{split} \tag{M3}$$

where the infinite dimensional Hamiltonian matrix $\mathcal{H}(\mathbf{q})$ has elements

$$\mathcal{H}(\mathbf{q})_{(\mathbf{g}',\alpha'),(\mathbf{g},\alpha)} = w_2 \delta_{\mathbf{g}',\mathbf{g}} \delta_{\alpha',\alpha} + \hbar v_F (\boldsymbol{\sigma} \cdot (\mathbf{q} - \mathbf{g}))_{\alpha',\alpha} \delta_{\mathbf{g}',\mathbf{g}}$$

$$+ \sum_{j=1}^{3} (T'_{\mathbf{Q}_j})_{\alpha',\alpha} \delta_{\mathbf{g}',\mathbf{g} - \mathbf{q}_j} + (T'^{\dagger}_{\mathbf{Q}_j})_{\alpha',\alpha} \delta_{\mathbf{g}',\mathbf{g} + \mathbf{q}_j}.$$
(M4)

For $\mathbf{g}_0 \in D(\delta\theta)\mathcal{Q}_0$, we have

$$\mathcal{H}(\mathbf{q} + \mathbf{g}_0)_{(\mathbf{g}',\alpha'),(\mathbf{g},\alpha)} = \mathcal{H}(\mathbf{q})_{(\mathbf{g}' - \mathbf{g}_0,\alpha'),(\mathbf{g} - \mathbf{g}_0,\alpha)}$$
(M5)

so that

$$\mathcal{H}(\mathbf{q} + \mathbf{g}_0) = V(\mathbf{g}_0)\mathcal{H}(\mathbf{q})V^{\dagger}(\mathbf{g}_0), \tag{M6}$$

where the unitary matrix $V(\mathbf{g}_0)$ has elements

$$V(\mathbf{g}_0)_{(\mathbf{g}',\alpha'),(\mathbf{g},\alpha)} = \delta_{\mathbf{g}',\mathbf{g}+\mathbf{g}_0} \delta_{\alpha',\alpha} \tag{M7}$$

and is called the embedding matrix.

Consider some set of $N_b \ge 1$ bands of $\mathcal{H}(\mathbf{q})$ that are disconnected from all other bands throughout BZ_M. Let $U(\mathbf{q})$ be

a matrix whose columns form an orthonormal basis for this set of bands. Importantly, we require

$$U(\mathbf{q} + \mathbf{g}_0) = V(\mathbf{g}_0)U(\mathbf{q}) \tag{M8}$$

for $\mathbf{g}_0 \in D(\delta\theta)\mathcal{Q}_0$. We define the non-Abelian Berry connection

$$\mathcal{A}(\mathbf{q}) = U^{\dagger}(\mathbf{q}) \nabla_{\mathbf{q}} U(\mathbf{q}). \tag{M9}$$

Although U is not actually periodic, Eq. (M8) implies

$$\mathcal{A}(\mathbf{q} + \mathbf{g}_0) = \mathcal{A}(\mathbf{q}) \tag{M10}$$

for $\mathbf{g}_0 \in D(\delta\theta)\mathcal{Q}_0$. As a result, \mathcal{A} is a well defined $U(N_b)$ gauge connection on the torus $\mathbb{T} = \mathbb{R}^2/D(\delta\theta)\mathcal{Q}_0$.

For any closed loop Γ in \mathbb{T} , we define the gauge covariant Wilson loop unitary

$$W(\mathbf{\Gamma}) = \mathcal{P} \exp \left[-\int_{\mathbf{\Gamma}} \mathcal{A}(\mathbf{q}) \cdot d\mathbf{q} \right], \quad (M11)$$

where \mathcal{P} indicates path ordering. For each $0 \le x < 1$, we define the loop $\Gamma_x(t) = x(\mathbf{q}_3 - \mathbf{q}_2) + t(\mathbf{q}_1 - \mathbf{q}_2)$ for $0 \le t \le 1$. Following Ref. [98], we compute

$$W(\mathbf{\Gamma}_{x}) = \mathcal{P} \exp \left[-\int_{\mathbf{\Gamma}_{x}} \mathcal{A}(\mathbf{q}) \cdot d\mathbf{q} \right]$$

$$= \lim_{N_{q} \to \infty} \prod_{j=N_{q}-1}^{0} \exp[-\mathcal{A}(\mathbf{\Gamma}_{x}(t_{j+1})) \cdot (\mathbf{\Gamma}_{x}(t_{j+1}) - \mathbf{\Gamma}_{x}(t_{j}))]$$

$$= \lim_{N_{q} \to \infty} \prod_{j=N_{q}-1}^{0} I - \mathcal{A}(\mathbf{\Gamma}_{x}(t_{j+1})) \cdot (\mathbf{\Gamma}_{x}(t_{j+1}) - \mathbf{\Gamma}_{x}(t_{j}))$$

$$= \lim_{N_{q} \to \infty} \prod_{j=N_{q}-1}^{0} I - U^{\dagger}(\mathbf{\Gamma}_{x}(t_{j+1})) (U(\mathbf{\Gamma}_{x}(t_{j+1})) - U(\mathbf{\Gamma}_{x}(t_{j})))$$

$$= \lim_{N_{q} \to \infty} \prod_{j=N_{q}-1}^{0} U^{\dagger}(\mathbf{\Gamma}_{x}(t_{j+1})) U(\mathbf{\Gamma}_{x}(t_{j})), \qquad (M12)$$

where I is the identity matrix and $t_j = j/N_q$. Since $W(\Gamma_x)$ is gauge covariant, its spectrum is gauge invariant. We will refer to the spectrum of $-i \ln(W(\Gamma_x))$ as a function of x as the Wilson loop band structure.

When we numerically compute the energy or Wilson loop band structure of \tilde{H} , we must truncate the infinite dimensional matrices $\mathcal{H}(\mathbf{q})$, $V(\mathbf{g}_0)$, and $U(\mathbf{q})$ to a finite number of dimensions. Since the infinite dimensional nature of $\mathcal{H}(\mathbf{q})$ comes from the infinite size of \mathcal{Q}_l , we equivalently need to choose a truncation of the lattices \mathcal{Q}_l . In order to make the symmetry operators C_{3z} , C_{2x} , and P well defined (see Appendixes I and L), we need a truncation $\tilde{\mathcal{Q}}_l$ of \mathcal{Q}_l satisfying

$$\begin{split} \tilde{\mathcal{Q}}_{-} &= -\tilde{\mathcal{Q}}_{+}, \\ R_{2\pi/3} \tilde{\mathcal{Q}}_{\pm} &= R^{x} \tilde{\mathcal{Q}}_{\pm} = \tilde{\mathcal{Q}}_{\pm}. \end{split} \tag{M13}$$

One such truncation is given explicitly by

$$\tilde{Q}_{l} = \{n_{1}\mathbf{Q}_{1} + n_{2}\mathbf{Q}_{2} + n_{3}\mathbf{Q}_{3} | n_{1} + n_{2} + n_{3}
= l, |n_{1}| + |n_{2}| + |n_{3}| \leq M\}$$
(M14)

for some $M \ge 1$. See Fig. 17 for an illustration of $D(\delta\theta)\hat{Q}_l$ as defined by Eq. (M14) with M=15. This truncation is equivalent to the " Γ_M -centered model" in Ref. [80]. As long as Eq. (M13) is satisfied, the finite dimensional truncated Hamiltonian retains exact $C_{2z}\mathcal{T}$, C_{3z} , and C_{2x} symmetries, and Eqs. ((L1), (L2), (L4), and (L5) hold as well. However, it should be noted that the moiré translation symmetry in Eq. (M6) is exact only when $M=\infty$.

APPENDIX N: REAL SPACE WAVEFUNCTIONS

In this section, we derive the form of the real space wave functions shown in Fig. 11. Suppose v is an eigenvector of $\mathcal{H}(\mathbf{q})$ where \mathcal{H} is given in Eq. (M4). In that case,

$$|\psi_{v}\rangle = \sum_{\mathbf{g} \in D(\delta\theta)(\mathcal{O}_{-} \cup \mathcal{O}_{+})} \sum_{\alpha \in \{A,B\}} v_{(\mathbf{g},\alpha)} |\mathbf{q}, \mathbf{g}, \alpha\rangle_{M}$$
(N1)

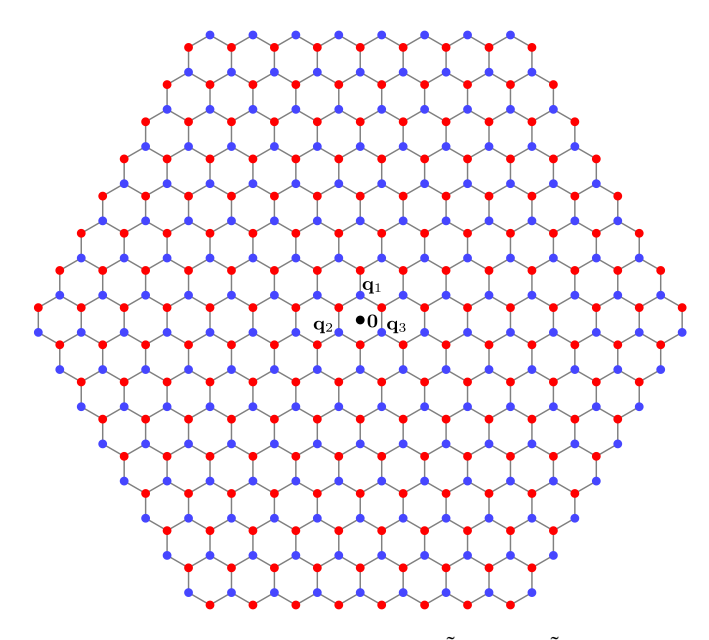


FIG. 17. The truncated lattices $D(\delta\theta)\tilde{\mathcal{Q}}_l$ where $\tilde{\mathcal{Q}}_l$ is given by Eq. (M14) with M=15. The blue (red) dots indicate l=+(-), the black dot indicates the origin, and the gray lines correspond to nonzero interlayer matrix elements in Eq. (M4). Each of $\tilde{\mathcal{Q}}_\pm$ has 192 points so this truncation corresponds to a model with 768 bands.

is the corresponding eigenvector of the continuum Hamiltonian \tilde{H} . Suppose the row vector of states $|\mathbf{r}\rangle_c'$ defined in Eq. (73) can be written in components as

$$|\mathbf{r}\rangle_c' = (|\mathbf{r}, +, A\rangle_c' |\mathbf{r}, +, B\rangle_c' |\mathbf{r}, -, A\rangle_c' |\mathbf{r}, -, B\rangle_c').$$
 (N2)

Note that $|\mathbf{r}, l, \alpha\rangle_c'$ differs from $|\mathbf{r}, l, \alpha\rangle_c$ in Eq. (40) only by a phase and satisfies

$$|\mathbf{r}, l, \alpha\rangle_c' = \frac{1}{2\pi} \int d^2\mathbf{p} e^{-i\mathbf{p}\cdot\mathbf{r}} |\mathbf{p}, l, \alpha\rangle_c'$$
 (N3)

where the states $|\mathbf{p}, l, \alpha\rangle_c'$ are defined in Eq. (M2). Using Eq. (M1), we have

$$\langle \mathbf{r}, l, \alpha |_c' \psi_v \rangle = \frac{e^{i\mathbf{q} \cdot \mathbf{r}}}{2\pi} \sum_{\mathbf{g} \in \mathcal{D}(S\theta) Q} v_{(\mathbf{g}, \alpha)} e^{-i\mathbf{g} \cdot \mathbf{r}}.$$
 (N4)

The plots in Fig. 11 show

$$\sum_{l \in \{+,-\}} \sum_{\alpha \in \{A,B\}} |\langle \mathbf{r}, l, \alpha |_c' \psi_v \rangle|^2$$
 (N5)

summed over one or more eigenvectors v with $\mathbf{q} = \mathbf{\Gamma}_M$. Importantly, this quantity is invariant under unitary mixing of the eigenvectors involved.

APPENDIX O: TRIPOD MODEL APPROXIMATION FOR MAGIC ANGLE CONDITIONS

In this section, we use Eqs. (M3) and (M4) to approximate the condition under which the bands of the continuum Hamiltonian nearest the Fermi level at charge neutrality become flat near the \mathbf{K}_{M} point in the moiré Brillouin zone. In

order to make the model analytically tractable, we use the truncation

$$\tilde{Q}_{+} = \{\mathbf{Q}_{1}\},$$

$$\tilde{Q}_{-} = \mathbf{Q}_{1} + \{\mathbf{Q}_{1}, \mathbf{Q}_{2}, \mathbf{Q}_{3}\},$$
(O1)

which produces a model called the "tripod Hamiltonian" [3,80]. Although this truncation does not satisfy Eq. (M13), it nonetheless enables a simple calculation of the magic angle in small angle TBG.

We now consider the eigenvalue problem for the tripod Hamiltonian near the \mathbf{K}_M point. We decompose the eigenvector ψ in the form

$$\psi = (|\mathbf{K}_{M} + \mathbf{p}, \mathbf{q}_{1}, A\rangle_{M} |\mathbf{K}_{M} + \mathbf{p}, \mathbf{q}_{1}, B\rangle_{M})\psi_{0}$$

$$+ \sum_{j=1}^{3} (|\mathbf{K}_{M} + \mathbf{p}, \mathbf{q}_{1} + \mathbf{q}_{j}, A\rangle_{M} |\mathbf{K}_{M} + \mathbf{p}, \mathbf{q}_{1} + \mathbf{q}_{j}, B\rangle_{M})\psi_{j},$$
(O2)

where ψ_0 , ψ_1 , ψ_2 , ψ_3 are two dimensional complex column vectors, **p** is a small vector, and the states $|\mathbf{q}, \mathbf{g}, \alpha\rangle_M$ are defined in Eq. (M1). The eigenvalue problem then takes the form

$$(w_2 I + \hbar v_F \boldsymbol{\sigma}_0 \cdot \mathbf{p}) \psi_0 + \sum_{j=1}^3 T'_{\mathbf{Q}_j} \psi_j = E \psi_0,$$

$$T'^{\dagger}_{\mathbf{Q}_j} \psi_0 + (w_2 I + \hbar v_F \boldsymbol{\sigma}_0 \cdot (\mathbf{p} - \mathbf{q}_j)) \psi_j = E \psi_j, \quad (O3)$$

where E is the energy and $T'_{\mathbf{Q}_j}$ is given by Eq. (71). Subtracting the w_2 terms and multiplying by

$$\lambda = \frac{s}{\hbar v_F |\mathbf{K}_M|} = \frac{s}{2\hbar v_F \sqrt{N} |\mathbf{K}| \sin(\delta\theta/2)},$$
 (O4)

the eigenvalue problem takes the dimensionless form

$$\boldsymbol{\sigma}_0 \cdot \mathbf{p}' \psi_0 + \sum_{i=1}^3 \tilde{T}'_{\mathbf{Q}_i} \psi_j = E' \psi_0, \tag{O5}$$

$$\tilde{T}_{\mathbf{Q}_{j}}^{\prime\dagger}\psi_{0}+\boldsymbol{\sigma}_{0}\cdot(\mathbf{p}'-\mathbf{q}_{j}'))\psi_{j}=E'\psi_{j},\tag{O6}$$

where $E' = \lambda(E - w_2)$, $\mathbf{p}' = s\mathbf{p}/|\mathbf{K}_M|$, $\tilde{T}_{\mathbf{Q}_j}' = \lambda T_{\mathbf{Q}_j}' = e^{i(\theta_0/4)\sigma_z}(\lambda T_{\mathbf{Q}_j})e^{i(\theta_0/4)\sigma_z}$, and $\mathbf{q}_j' = s\mathbf{q}_j/|\mathbf{K}_M| = R_{2\pi/3}^{j-1}\mathbf{\hat{y}}$. We first solve Eq. (O6) for ψ_j

$$\psi_j = (E'I - \boldsymbol{\sigma}_0 \cdot (\mathbf{p}' - \mathbf{q}'_j))^{-1} \tilde{T}_{\mathbf{Q}_j}^{\prime \dagger} \psi_0 \tag{O7}$$

$$=\frac{E'I+\boldsymbol{\sigma}_{0}\cdot(\mathbf{p}'-\mathbf{q}'_{j})}{E'^{2}-|\mathbf{p}'-\mathbf{q}'_{j}|^{2}}\tilde{T}_{\mathbf{Q}_{j}}^{\prime\dagger}\psi_{0} \tag{O8}$$

assuming that $E'^2 - |\mathbf{p}' - \mathbf{q}'_j|^2 \neq 0$. Next, we use use Eq. (O5) to find

$$\left(E'I - \boldsymbol{\sigma}_0 \cdot \mathbf{p}' + \sum_{j=1}^3 \tilde{T}'_{\mathbf{Q}_j} \frac{E'I + \boldsymbol{\sigma}_0 \cdot (\mathbf{p}' - \mathbf{q}'_j)}{|\mathbf{p}' - \mathbf{q}'_j|^2 - E'^2} \tilde{T}'^{\dagger}_{\mathbf{Q}_j}\right) \psi_0 = 0.$$
(O9)

We first consider the case $\mathbf{p}' = \mathbf{0}$. Eq. (09) then becomes

$$0 = \left(E'I + \sum_{j=1}^{3} \tilde{T}'_{\mathbf{Q}_{j}} \frac{E'I - \sigma_{0} \cdot \mathbf{q}'_{j}}{1 - E'^{2}} \tilde{T}'_{\mathbf{Q}_{j}}^{\dagger} \right) \psi_{0}$$

$$= \left(E'I + \frac{E'}{1 - E'^{2}} \sum_{j=1}^{3} \tilde{T}'_{\mathbf{Q}_{j}} \tilde{T}'_{\mathbf{Q}_{j}}^{\dagger} - \frac{1}{1 - E'^{2}} \sum_{j=1}^{3} \tilde{T}'_{\mathbf{Q}_{j}} (\sigma_{0} \cdot \mathbf{q}'_{j}) \tilde{T}'_{\mathbf{Q}_{j}}^{\dagger} \right) \psi_{0}. \tag{O10}$$

Using the identities

$$\sum_{i=1}^{3} \tilde{T}'_{\mathbf{Q}_{j}} \tilde{T}'^{\dagger}_{\mathbf{Q}_{j}} = 3\lambda^{2} (w_{0}^{2} + w_{1}^{2})I,$$

$$\sum_{j=1}^{3} \tilde{T}'_{\mathbf{Q}_{j}}(\boldsymbol{\sigma}_{0} \cdot \mathbf{q}'_{j}) \tilde{T}'^{\dagger}_{\mathbf{Q}_{j}} = 6\lambda^{2} w_{0} w_{1} \sin(\phi_{0}) I, \tag{O11}$$

Eq. (O10) becomes

$$\left(E' + \frac{E'}{1 - E'^2} 3\lambda^2 \left(w_0^2 + w_1^2\right) - \frac{1}{1 - E'^2} 6\lambda^2 w_0 w_1 \sin(\phi_0)\right) \psi_0 = 0.$$
(O12)

Since $\psi_0 \neq 0$, we conclude

$$E^{3} - E\left[1 + 3\lambda^{2}(w_{0}^{2} + w_{1}^{2})\right] + 6\lambda^{2}w_{0}w_{1}\sin(\phi_{0}) = 0.$$
(O13)

Note that when E' = 1, the cubic polynomial in Eq. (O13) takes the value

$$-3\lambda^{2}(w_{0}^{2}+w_{1}^{2})+6\lambda^{2}w_{0}w_{1}\sin(\phi_{0}) \leqslant -3\lambda^{2}(w_{0}^{2}+w_{1}^{2})+6\lambda^{2}|w_{0}||w_{1}| = -3\lambda^{2}(|w_{0}|-|w_{1}|)^{2} \leqslant 0$$
(O14)

and when E' = -1, it takes the value

$$3\lambda^{2}(w_{0}^{2} + w_{1}^{2}) + 6\lambda^{2}w_{0}w_{1}\sin(\phi_{0}) \geqslant 3\lambda^{2}(w_{0}^{2} + w_{1}^{2}) - 6\lambda^{2}|w_{0}||w_{1}| = 3\lambda^{2}(|w_{0}| - |w_{1}|)^{2} \geqslant 0.$$
(O15)

There is therefore some solution $E'=E'_0$ of Eq. (O13) with E'_0 in the interval [-1,1]. Additionally, when $|\sin(\phi_0)|<1$ or $|w_0|\neq |w_1|$, we can take E'_0 in the interval (-1,1). In this case, we can approximate $E'^3_0\approx 0$ and find

$$E_0' \approx \frac{6\lambda^2 w_0 w_1 \sin(\phi_0)}{1 + 3\lambda^2 (w_0^2 + w_1^2)} \in (-1, 1). \tag{O16}$$

When $|\sin(\phi_0)| = 1$ and $|w_0| = |w_1|$, it is possible that there is no solution of Eq. (O13) in (-1, 1). We will not consider this case further.

Next, we consider Eq. (O9) with $\mathbf{p}' \neq \mathbf{0}$. We take $E' = E'_0 + \delta E'$ and expand to first order in $\delta E'$ and $|\mathbf{p}'|$. Using $|\mathbf{p}' - \mathbf{q}'_j|^2 \approx 1 - 2\mathbf{p}' \cdot \mathbf{q}'_j$, $E'^2 \approx E'_0^2 + 2E'_0\delta E'$, and the fact that E'_0 solves Eq. (O13), we find

$$0 \approx \left((E'_{0} + \delta E')I - \boldsymbol{\sigma}_{0} \cdot \mathbf{p}' + \sum_{j=1}^{3} \tilde{T}'_{\mathbf{Q}_{j}} \frac{(E'_{0} + \delta E')I + \boldsymbol{\sigma}_{0} \cdot (\mathbf{p}' - \mathbf{q}'_{j})}{1 - E'_{0}^{2} - 2\mathbf{p}' \cdot \mathbf{q}'_{j} - 2E'_{0}\delta E'} \tilde{T}'_{\mathbf{Q}_{j}} \right) \psi_{0}$$

$$= \left((E'_{0} + \delta E')I - \boldsymbol{\sigma}_{0} \cdot \mathbf{p}' + \sum_{j=1}^{3} \tilde{T}'_{\mathbf{Q}_{j}} \frac{(E'_{0} + \delta E')I + \boldsymbol{\sigma}_{0} \cdot (\mathbf{p}' - \mathbf{q}'_{j})}{1 - E'_{0}^{2}} \tilde{T}'_{\mathbf{Q}_{j}} \frac{1}{1 - \frac{2\mathbf{p}' \cdot \mathbf{q}'_{j} + 2E'_{0}\delta E'}{1 - E'_{0}^{2}}} \right) \psi_{0}$$

$$\approx ((E'_{0} + \delta E')I - \boldsymbol{\sigma}_{0} \cdot \mathbf{p}') \psi_{0}$$

$$+ \left(\sum_{j=1}^{3} \tilde{T}'_{\mathbf{Q}_{j}} \frac{E'_{0}I - \boldsymbol{\sigma}_{0} \cdot \mathbf{q}'_{j}}{1 - E'_{0}^{2}} \tilde{T}'_{\mathbf{Q}_{j}} + \sum_{j=1}^{3} \tilde{T}'_{\mathbf{Q}_{j}} \frac{\delta E'I + \boldsymbol{\sigma}_{0} \cdot \mathbf{p}'}{1 - E'_{0}^{2}} \tilde{T}'_{\mathbf{Q}_{j}} \right) \left(1 + \frac{2\mathbf{p}' \cdot \mathbf{q}'_{j} + 2E'_{0}\delta E'}{1 - E'_{0}^{2}} \right) \psi_{0}$$

$$\approx \left(\delta E'I - \boldsymbol{\sigma}_{0} \cdot \mathbf{p}' + \sum_{j=1}^{3} \tilde{T}'_{\mathbf{Q}_{j}} \frac{E'_{0}I - \boldsymbol{\sigma}_{0} \cdot \mathbf{q}'_{j}}{1 - E'_{0}^{2}} \tilde{T}'_{\mathbf{Q}_{j}} \right) \frac{2\mathbf{p}' \cdot \mathbf{q}'_{j} + 2E'_{0}\delta E'}{1 - E'_{0}^{2}} + \sum_{j=1}^{3} \tilde{T}'_{\mathbf{Q}_{j}} \frac{\delta E'I + \boldsymbol{\sigma}_{0} \cdot \mathbf{p}'}{1 - E'_{0}^{2}} \tilde{T}'_{\mathbf{Q}_{j}} \right) \psi_{0}. \tag{O17}$$

Using the identities in Eq. (O11) as well as

$$\sum_{j=1}^{3} \tilde{T}'_{\mathbf{Q}_{j}}(\boldsymbol{\sigma}_{0} \cdot \mathbf{q}'_{j})(2\mathbf{p}' \cdot \mathbf{q}'_{j})\tilde{T}'^{\dagger}_{\mathbf{Q}_{j}} = -3\lambda^{2}w_{1}^{2}\boldsymbol{\sigma}_{0} \cdot \mathbf{p}' + 3\lambda^{2}w_{0}^{2}\boldsymbol{\sigma}_{-2\phi_{0}} \cdot \mathbf{p}'$$

$$\sum_{j=1}^{3} \tilde{T}'_{\mathbf{Q}_{j}}(2\mathbf{p}' \cdot \mathbf{q}'_{j})\tilde{T}'^{\dagger}_{\mathbf{Q}_{j}} = 6\lambda^{2}w_{0}w_{1}\boldsymbol{\sigma}_{-\phi_{0}-\pi/2} \cdot \mathbf{p}'$$

$$\sum_{j=1}^{3} \tilde{T}'_{\mathbf{Q}_{j}}(\boldsymbol{\sigma}_{0} \cdot \mathbf{p}')\tilde{T}'^{\dagger}_{\mathbf{Q}_{j}} = 3\lambda^{2}w_{0}^{2}\boldsymbol{\sigma}_{-2\phi_{0}} \cdot \mathbf{p}',$$
(O18)

Equation (O17) becomes

$$\left[\left(1 - \frac{2E_0'^3}{1 - E_0'^2} + \frac{3\lambda^2(w_0^2 + w_1^2)}{1 - E_0'^2} \right) \delta E' I + \left(-1 + \frac{3\lambda^2 w_1^2}{1 - E_0'^2} \right) \boldsymbol{\sigma}_0 \cdot \mathbf{p}' + \frac{E_0'}{1 - E_0'^2} (6\lambda^2 w_0 w_1 \boldsymbol{\sigma}_{-\phi_0 - \pi/2} \cdot \mathbf{p}') \right] \psi_0 = 0.$$
(O19)

We are interested in the conditions under which the terms proportional to \mathbf{p}' in Eq. (O19) vanish so that $\delta E' = 0$ to first order in $|\mathbf{p}'|$. If $E'_0 = 0$, this condition is equivalent to $3\lambda^2 w_1^2 = 1$ or

$$\lambda = \pm \frac{1}{|w_1|\sqrt{3}}.\tag{O20}$$

Since $E_0' = 0$ when $w_0 = 0$ or $\phi_0 = 0$, we recognize this as the magic angle condition identified in Refs. [3,80], which is realizable in small angle TBG. However, there is another solution with $\phi_0 = \pm \pi/2$ and

$$\frac{3\lambda^2 w_1^2}{1 - E_0^{\prime 2}} = 1 \pm \frac{E_0^{\prime}}{1 - E_0^{\prime 2}} 6\lambda^2 w_0 w_1 \tag{O21}$$

or equivalently

$$E_0^{\prime 2} \mp 6\lambda^2 w_0 w_1 E_0^{\prime} + 3\lambda^2 w_1^2 - 1 = 0.$$
(O22)

By Eq. (O13), E'_0 also satisfies

$$E_0^{\prime 3} - E_0^{\prime} \left[1 + 3\lambda^2 (w_0^2 + w_1^2) \right] \pm 6\lambda^2 w_0 w_1 = 0$$
(O23)

so we need to find when these two equations have a common solution for E_0' in the interval (-1, 1). Assuming $|w_0| \neq |w_1|$, we can take the approximation $E_0'^3 \approx 0$ so that Eqs. (O22) and (O23) become

$$27w_1^2(w_1^4 - 2w_0^2w_1^2 - 3w_0^4)\lambda^6 + 9(w_1^4 - w_0^4)\lambda^4 - 3(w_1^2 + 2w_0^2)\lambda^2 - 1 = 0.$$
(O24)

It is easy to see that this equation has real solutions for λ if and only if $|w_0| < |w_1|$.

We conclude that the magic angle conditions for the tripod Hamiltonian are Eq. (O20) when either $w_0 = 0$ or $\phi_0 = 0$, and Eq. (O24) when $\phi_0 = \pm \pi/2$ and $|w_0| < |w_1|$.

APPENDIX P: ADDITIONAL HEATMAPS AND MOIRÉ BAND STRUCTURES

Figures 18–22 show some additional heatmaps and moiré band structures (see captions for details).

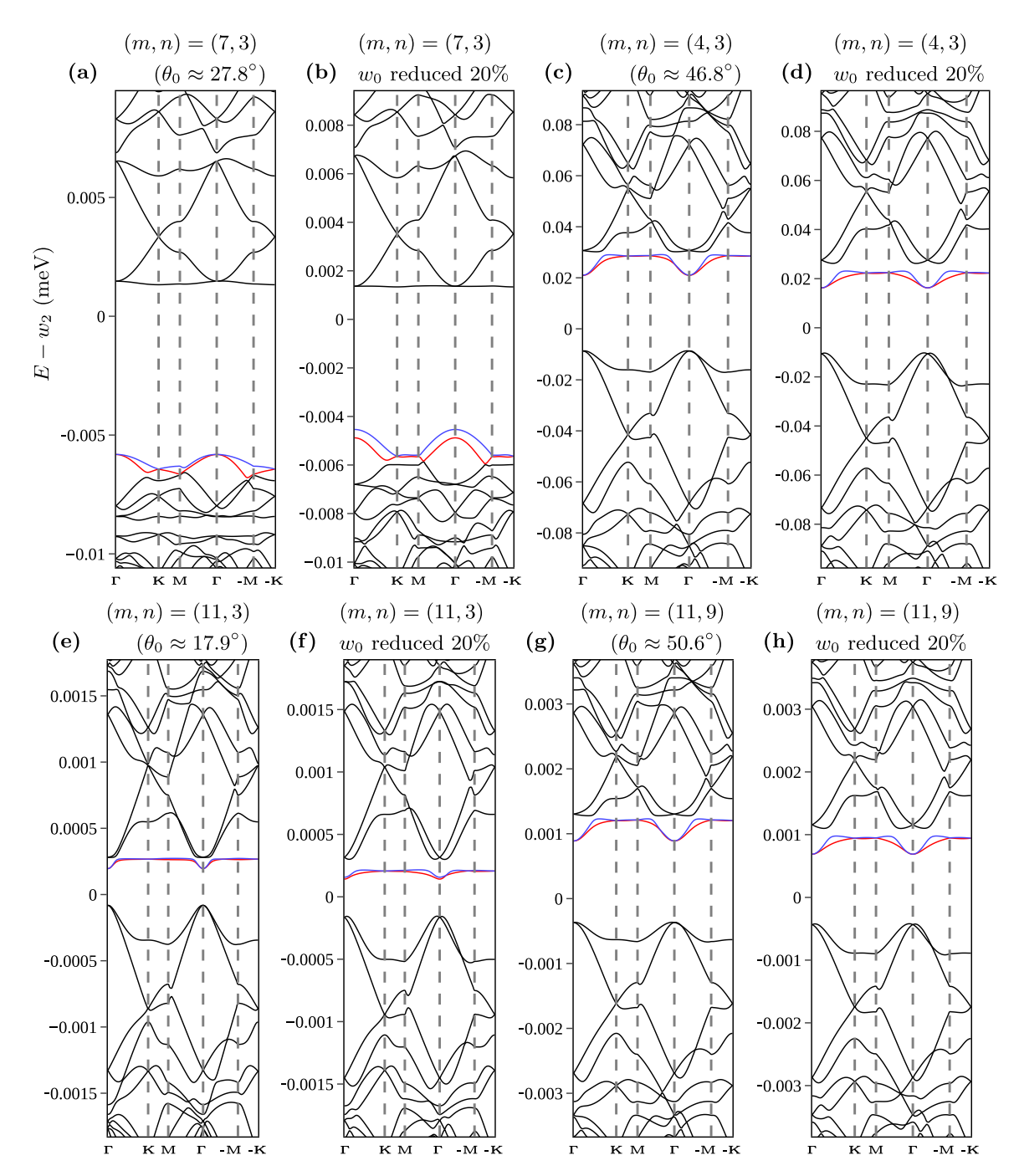


FIG. 18. Moiré band structures at the first magic angle $\delta\theta = \theta - \theta_0 = \delta\theta_{\text{magic}}$ near the latter four (m, n) commensurate configurations in Table II. The band structures were computed with the Hamiltonian in Eq. (63) and the quasimomentum truncation illustrated in Appendix Fig. 17. The horizontal axes follow the moiré quasimomentum trajectory $\Gamma_M \to \mathbf{K}_M \to \mathbf{M}_M \to \mathbf{\Gamma}_M \to -\mathbf{M}_M \to -\mathbf{K}_M$. The two bands nearest charge neutrality are shown in blue and red while all other bands are shown in black. The parameters for (a), (c), (e), and (g) are taken from Table II. The parameters for (b), (d), (f), and (h) are the same as those for (a), (c), (e), and (g) except with the values of w_0 reduced by 20%.

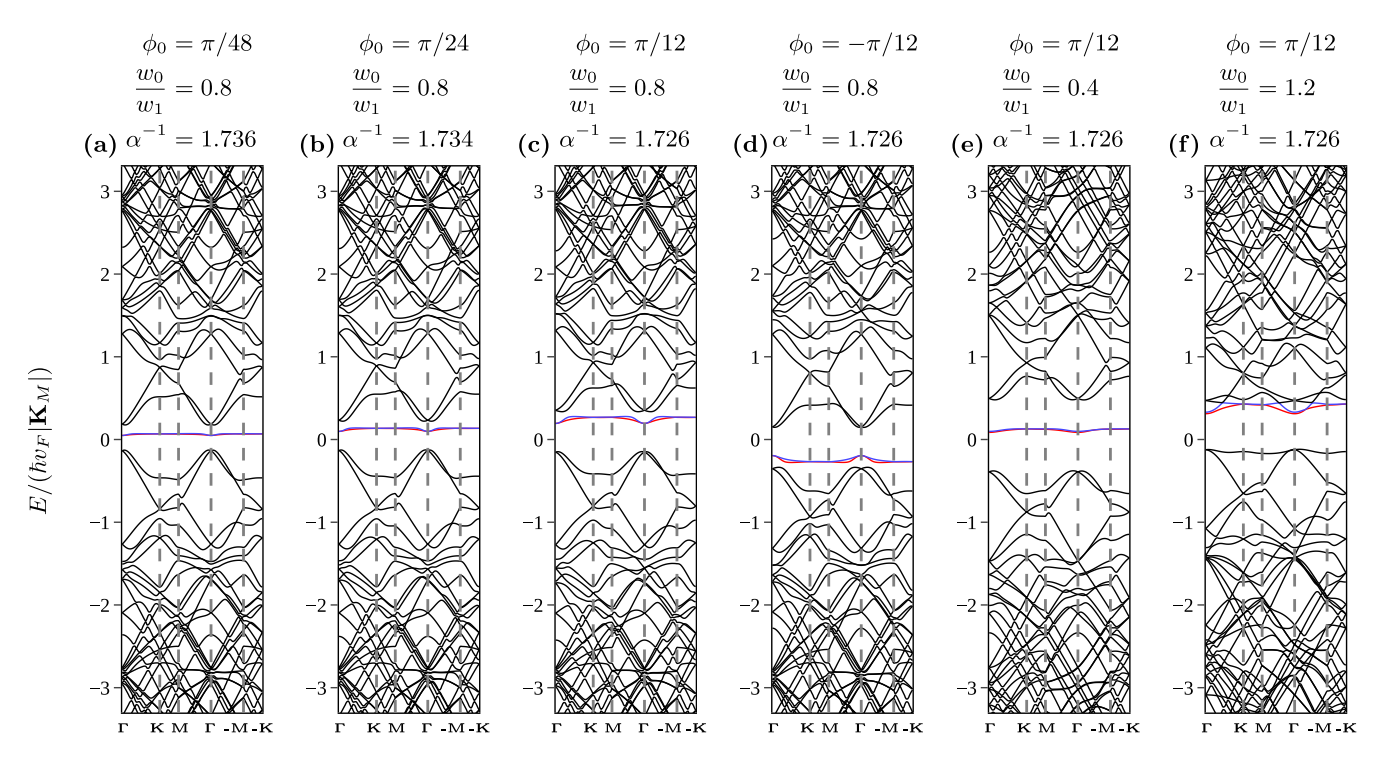


FIG. 19. [(a)-(c)] Moiré band structures in the first magic manifold (see Sec. VIB) for four different small values of ϕ_0 . [(d)-(f)] Variations on (c) in which the value of ϕ_0 is negated or the value of w_0/w_1 is changed. Note that in (f) where w_0/w_1 is large, the lowest two bands at charge neutrality are no longer isolated from the higher bands. All panels use the model of Eq. (69) with $w_2=0$ and the quasimomentum truncation illustrated in Appendix Fig. 17. The horizontal axes follow the moiré quasimomentum trajectory $\Gamma_M \to \mathbf{K}_M \to \mathbf{M}_M \to \mathbf{\Gamma}_M \to -\mathbf{M}_M \to -\mathbf{K}_M$. The two bands nearest charge neutrality are shown in blue and red while all other bands are shown in black.

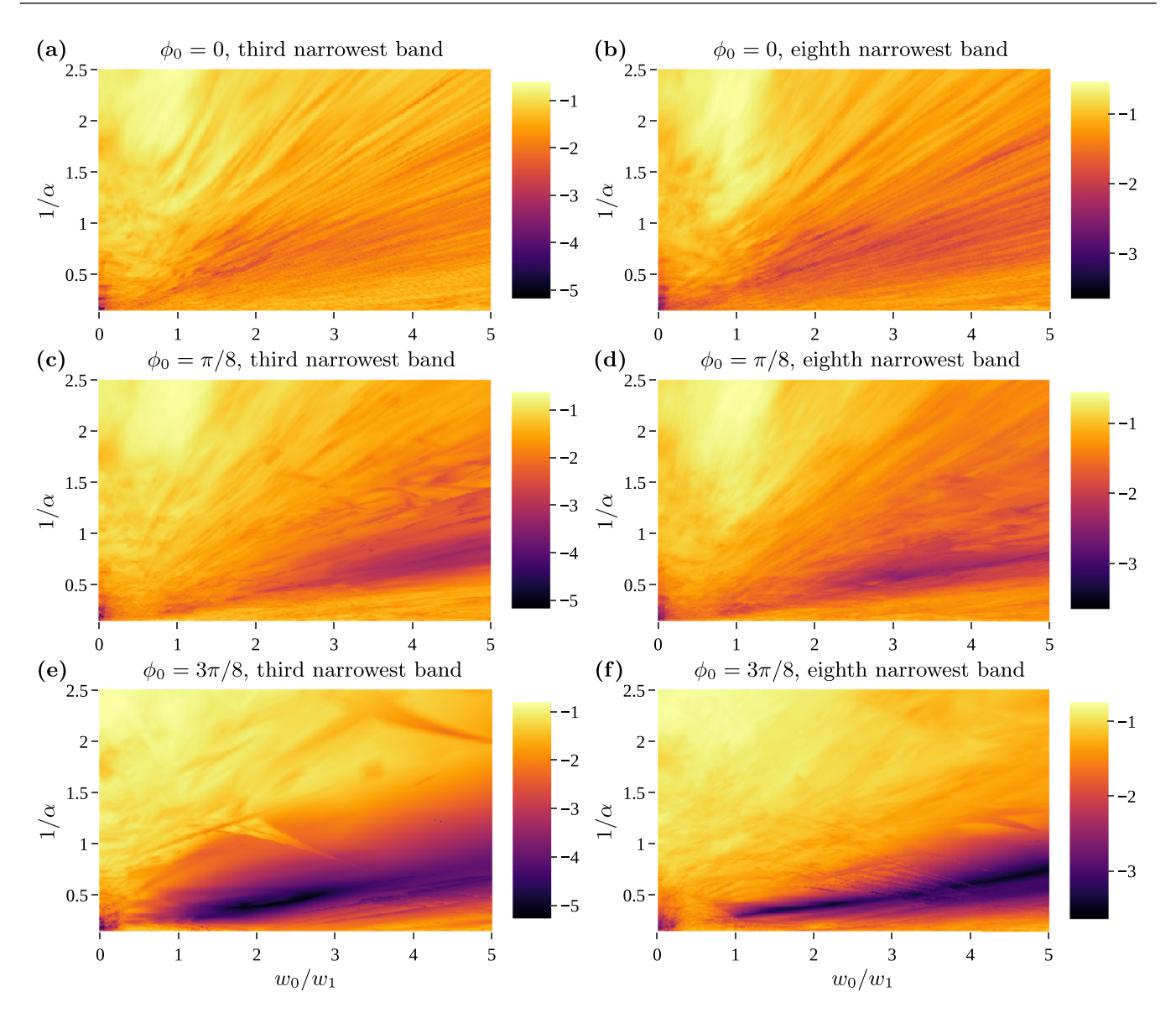


FIG. 20. Heat maps showing the base 10 logarithm of the bandwidth (in units of $\hbar v_F |\mathbf{K}_M|$) of the third and eighth narrowest bands among the first 20 conduction bands and the first 20 valence bands at charge neutrality for $\phi_0 = 0$, $\pi/8$, and $3\pi/8$. The bandwidth was computed with the points Γ_M , \mathbf{K}_M , \mathbf{M}_M , $\mathbf{K}_M/2$, $\mathbf{M}_M/2$, $-\mathbf{M}_M/2$ in BZ_M. For this computation, we use the model in Eq. (69) with the quasimomentum truncation illustrated in Appendix Fig. 17. The dark regions indicate parameters in the hypermagic regime discussed in Sec. VI C. See Fig. 9 for similar heat maps with $\phi_0 = \pi/4$ and $\pi/2$.

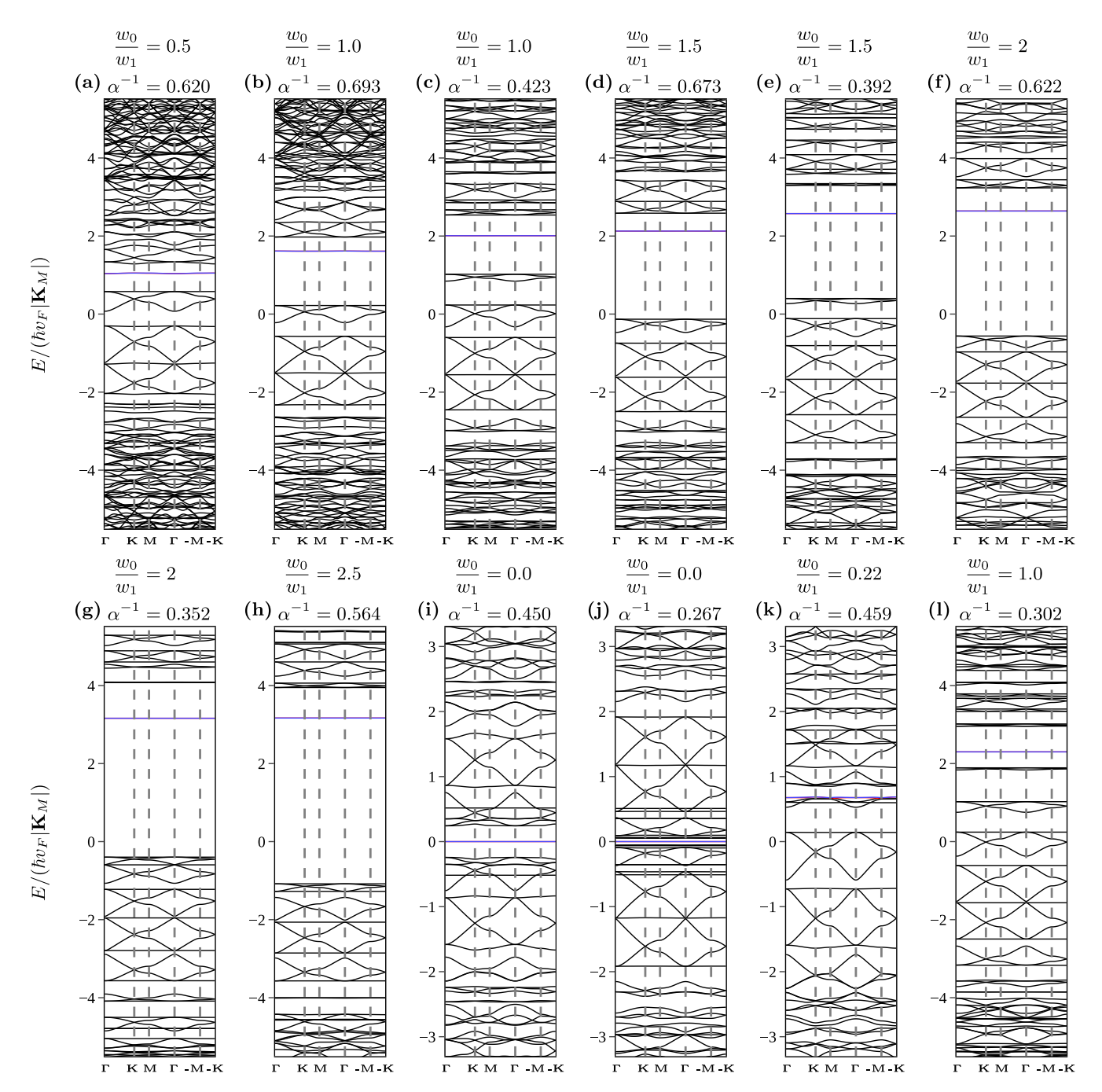


FIG. 21. Moiré band structures using the model in Eq. (69) with $w_2 = 0$, $\phi_0 = \pi/2$, and various parameters w_0/w_1 and α^{-1} located in the three dark curves in Fig. 8(c). Since each panel has many simultaneous flat bands, these parameters all belong to the hypermagic regime discussed in Sec. VI C. For this computation, we use the quasimomentum truncation illustrated in Fig. 17. The horizontal axes follow the moiré quasimomentum trajectory $\Gamma_M \to \mathbf{K}_M \to \mathbf{M}_M \to \mathbf{\Gamma}_M \to -\mathbf{M}_M \to -\mathbf{K}_M$. The two bands nearest charge neutrality are shown in blue and red while all other bands are shown in black. Note that (i) and (j) are in the chiral limit $w_0 = 0$ so that ϕ_0 does not affect their band structure. The α^{-1} values for (i) and (j) correspond to the second and third magic angles in the chiral limit, respectively [12].

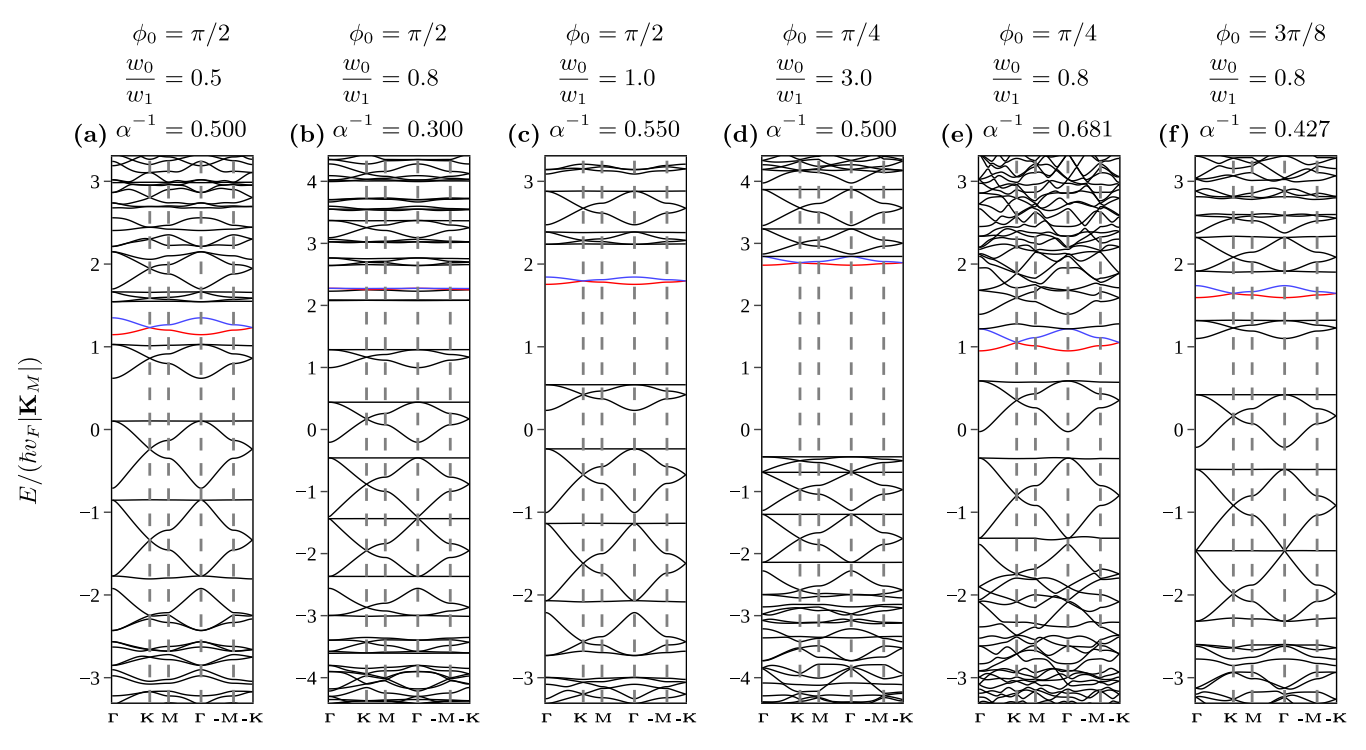


FIG. 22. Moiré band structures using the model in Eq. (69) with $w_2 = 0$ and various values of ϕ_0 , w_0/w_1 , and α^{-1} in the hypermagic regime discussed in Sec. VIC but not in the three dark curves in Fig. 8(c). For this computation, we use the quasimomentum truncation illustrated in Fig. 17. The horizontal axes follow the moiré quasimomentum trajectory $\Gamma_M \to K_M \to M_M \to \Gamma_M \to -M_M \to -K_M$. The two bands nearest charge neutrality are shown in blue and red while all other bands are shown in black. The lowest bands in (b), (d), and (e) form kagome-like groups of three as discussed in Sec. VIC. The lowest bands in (b) are also shown in Fig. 12(a). In contrast, the lowest two bands in (a), (c), and (f) are gapped from higher bands and resemble those of graphene. (a)–(c) have $\phi_0 = \pi/2$ while (d)–(f) have smaller values of ϕ_0 . The w_0/w_1 and α^{-1} parameters for (e) and (f) are the same as those for Fig. 10(e) and 10(f).

- [1] S. Shallcross, S. Sharma, and O. A. Pankratov, Quantum Interference at the Twist Boundary in Graphene, Phys. Rev. Lett. **101**, 056803 (2008).
- [2] S. Shallcross, S. Sharma, E. Kandelaki, and O. A. Pankratov, Electronic structure of turbostratic graphene, Phys. Rev. B 81, 165105 (2010).
- [3] R. Bistritzer and A. H. MacDonald, Moiré bands in twisted double-layer graphene, Proc. Natl. Acad. Sci. USA 108, 12233 (2011).
- [4] H. C. Po, L. Zou, A. Vishwanath, and T. Senthil, Origin of Mott Insulating Behavior and Superconductivity in Twisted Bilayer Graphene, Phys. Rev. X 8, 031089 (2018).
- [5] Z. Song, Z. Wang, W. Shi, G. Li, C. Fang, and B. A. Bernevig, All Magic Angles in Twisted Bilayer Graphene are Topological, Phys. Rev. Lett. 123, 036401 (2019).
- [6] H. C. Po, L. Zou, T. Senthil, and A. Vishwanath, Faithful tight-binding models and fragile topology of magic-angle bilayer graphene, Phys. Rev. B 99, 195455 (2019).
- [7] J. Ahn, S. Park, and B.-J. Yang, Failure of Nielsen-Ninomiya Theorem and Fragile Topology in Two-Dimensional Systems with Space-Time Inversion Symmetry: Application to Twisted Bilayer Graphene at Magic Angle, Phys. Rev. X 9, 021013 (2019).
- [8] B. Lian, F. Xie, and B. A. Bernevig, Landau level of fragile topology, Phys. Rev. B **102**, 041402(R) (2020).

- [9] J. Kang and O. Vafek, Symmetry, Maximally Localized Wannier States, and a Low-Energy Model for Twisted Bilayer Graphene Narrow Bands, Phys. Rev. X 8, 031088 (2018).
- [10] M. Koshino, N. F. Q. Yuan, T. Koretsune, M. Ochi, K. Kuroki, and L. Fu, Maximally Localized Wannier Orbitals and the Extended Hubbard Model for Twisted Bilayer Graphene, Phys. Rev. X 8, 031087 (2018).
- [11] J. Liu, J. Liu, and X. Dai, Pseudo Landau level representation of twisted bilayer graphene: Band topology and implications on the correlated insulating phase, Phys. Rev. B **99**, 155415 (2019).
- [12] G. Tarnopolsky, A. J. Kruchkov, and A. Vishwanath, Origin of Magic Angles in Twisted Bilayer Graphene, Phys. Rev. Lett. 122, 106405 (2019).
- [13] Z.-D. Song and B. A. Bernevig, Magic-Angle Twisted Bilayer Graphene as a Topological Heavy Fermion Problem, Phys. Rev. Lett. 129, 047601 (2022).
- [14] J. Wang, Y. Zheng, A. J. Millis, and J. Cano, Chiral approximation to twisted bilayer graphene: Exact intravalley inversion symmetry, nodal structure, and implications for higher magic angles, Phys. Rev. Res. 3, 023155 (2021).
- [15] K. Kim, A. DaSilva, S. Huang, B. Fallahazad, S. Larentis, T. Taniguchi, K. Watanabe, B. J. LeRoy, A. H. MacDonald, and E. Tutuc, Tunable moiré bands and strong correlations in small-

- twist-angle bilayer graphene, Proc. Natl. Acad. Sci. USA 114, 3364 (2017).
- [16] Y. Cao, V. Fatemi, S. Fang, K. Watanabe, T. Taniguchi, E. Kaxiras, and P. Jarillo-Herrero, Unconventional superconductivity in magic-angle graphene superlattices, Nature (London) 556, 43 (2018).
- [17] Y. Cao, V. Fatemi, A. Demir, S. Fang, S. L. Tomarken, J. Y. Luo, J. D. Sanchez-Yamagishi, K. Watanabe, T. Taniguchi, E. Kaxiras, R. C. Ashoori, and P. Jarillo-Herrero, Correlated insulator behaviour at half-filling in magic-angle graphene superlattices, Nature (London) 556, 80 (2018).
- [18] X. Lu, P. Stepanov, W. Yang, M. Xie, M. A. Aamir, I. Das, C. Urgell, K. Watanabe, T. Taniguchi, G. Zhang, A. Bachtold, A. H. MacDonald, and D. K. Efetov, Superconductors, orbital magnets and correlated states in magic-angle bilayer graphene, Nature (London) 574, 653 (2019).
- [19] M. Yankowitz, S. Chen, H. Polshyn, Y. Zhang, K. Watanabe, T. Taniguchi, D. Graf, A. F. Young, and C. R. Dean, Tuning superconductivity in twisted bilayer graphene, Science 363, 1059 (2019).
- [20] Y. Xie, B. Lian, B. Jäck, X. Liu, C. L. Chiu, K. Watanabe, T. Taniguchi, B. A. Bernevig, and A. Yazdani, Spectroscopic signatures of many-body correlations in magic-angle twisted bilayer graphene, Nature (London) 572, 101 (2019).
- [21] Y. Choi, J. Kemmer, Y. Peng, A. Thomson, H. Arora, R. Polski, Y. Zhang, H. Ren, J. Alicea, G. Refael, F. von Oppen, K. Watanabe, T. Taniguchi, and S. Nadj-Perge, Electronic correlations in twisted bilayer graphene near the magic angle, Nat. Phys. 15, 1174 (2019).
- [22] Y. Jiang, X. Lai, K. Watanabe, T. Taniguchi, K. Haule, J. Mao, and E. Y. Andrei, Charge order and broken rotational symmetry in magic-angle twisted bilayer graphene, Nature (London) 573, 91 (2019).
- [23] A. Kerelsky, L. J. McGilly, D. M. Kennes, L. Xian, M. Yankowitz, S. Chen, K. Watanabe, T. Taniguchi, J. Hone, C. Dean, A. Rubio, and A. N. Pasupathy, Maximized electron interactions at the magic angle in twisted bilayer graphene, Nature (London) 572, 95 (2019).
- [24] A. L. Sharpe, E. J. Fox, A. W. Barnard, J. Finney, K. Watanabe, T. Taniguchi, M. A. Kastner, and D. Goldhaber-Gordon, Emergent ferromagnetism near three-quarters filling in twisted bilayer graphene, Science 365, 605 (2019).
- [25] Y. Cao, D. Chowdhury, D. Rodan-Legrain, O. Rubies-Bigorda, K. Watanabe, T. Taniguchi, T. Senthil, and P. Jarillo-Herrero, Strange Metal in Magic-Angle Graphene with near Planckian Dissipation, Phys. Rev. Lett. 124, 076801 (2020).
- [26] M. Serlin, C. L. Tschirhart, H. Polshyn, Y. Zhang, J. Zhu, K. Watanabe, T. Taniguchi, L. Balents, and A. F. Young, Intrinsic quantized anomalous Hall effect in a moiré heterostructure, Science 367, 900 (2020).
- [27] D. Wong, K. P. Nuckolls, M. Oh, B. Lian, Y. Xie, S. Jeon, K. Watanabe, T. Taniguchi, B. A. Bernevig, and A. Yazdani, Cascade of electronic transitions in magic-angle twisted bilayer graphene, Nature (London) 582, 198 (2020).
- [28] K. P. Nuckolls, M. Oh, D. Wong, B. Lian, K. Watanabe, T. Taniguchi, B. A. Bernevig, and A. Yazdani, Strongly correlated Chern insulators in magic-angle twisted bilayer graphene, Nature (London) 588, 610 (2020).
- [29] Y. Choi, H. Kim, Y. Peng, A. Thomson, C. Lewandowski, R. Polski, Y. Zhang, H. S. Arora, K. Watanabe, T. Taniguchi *et al.*,

- Correlation-driven topological phases in magic-angle twisted bilayer graphene, Nature (London) **589**, 536 (2021).
- [30] Y. Saito, J. Ge, L. Rademaker, K. Watanabe, T. Taniguchi, D. A. Abanin, and A. F. Young, Hofstadter subband ferromagnetism and symmetry-broken Chern insulators in twisted bilayer graphene, Nat. Phys. 17, 478 (2021).
- [31] I. Das, X. Lu, J. Herzog-Arbeitman, Z.-D. Song, K. Watanabe, T. Taniguchi, B. A. Bernevig, and D. K. Efetov, Symmetry broken Chern insulators and magic series of Rashba-like Landau level crossings in magic angle bilayer graphene, Nat. Phys. 17, 710 (2021).
- [32] S. Wu, Z. Zhang, K. Watanabe, T. Taniguchi, and E. Y. Andrei, Chern insulators, van Hove singularities and topological flat bands in magic-angle twisted bilayer graphene, Nat. Mater. 20, 488 (2021).
- [33] M. Oh, K. P. Nuckolls, D. Wong, R. L. Lee, X. Liu, K. Watanabe, T. Taniguchi, and A. Yazdani, Evidence for unconventional superconductivity in twisted bilayer graphene, Nature (London) 600, 240 (2021).
- [34] M. Ochi, M. Koshino, and K. Kuroki, Possible correlated insulating states in magic-angle twisted bilayer graphene under strongly competing interactions, Phys. Rev. B 98, 081102(R) (2018).
- [35] F. Guinea and N. R. Walet, Electrostatic effects, band distortions, and superconductivity in twisted graphene bilayers, Proc. Natl. Acad. Sci. USA 115, 13174 (2018).
- [36] J. W. F. Venderbos and R. M. Fernandes, Correlations and electronic order in a two-orbital honeycomb lattice model for twisted bilayer graphene, Phys. Rev. B **98**, 245103 (2018).
- [37] B. Lian, Z. Wang, and B. A. Bernevig, Twisted Bilayer Graphene: A Phonon-Driven Superconductor, Phys. Rev. Lett. 122, 257002 (2019).
- [38] F. Wu, A. H. MacDonald, and I. Martin, Theory of Phonon-Mediated Superconductivity in Twisted Bilayer Graphene, Phys. Rev. Lett. 121, 257001 (2018).
- [39] H. Isobe, N. F. Q. Yuan, and L. Fu, Unconventional Superconductivity and Density Waves in Twisted Bilayer Graphene, Phys. Rev. X 8, 041041 (2018).
- [40] A. Thomson, S. Chatterjee, S. Sachdev, and M. S. Scheurer, Triangular antiferromagnetism on the honeycomb lattice of twisted bilayer graphene, Phys. Rev. B 98, 075109 (2018).
- [41] J. F. Dodaro, S. A. Kivelson, Y. Schattner, X.-Q. Sun, and C. Wang, Phases of a phenomenological model of twisted bilayer graphene, Phys. Rev. B **98**, 075154 (2018).
- [42] J. Gonzalez and T. Stauber, Kohn-Luttinger Superconductivity in Twisted Bilayer Graphene, Phys. Rev. Lett. **122**, 026801 (2019).
- [43] N. F. Q. Yuan and L. Fu, Model for the metal-insulator transition in graphene superlattices and beyond, Phys. Rev. B 98, 045103 (2018)
- [44] J. Kang and O. Vafek, Strong Coupling Phases of Partially Filled Twisted Bilayer Graphene Narrow Bands, Phys. Rev. Lett. **122**, 246401 (2019).
- [45] N. Bultinck, E. Khalaf, S. Liu, S. Chatterjee, A. Vishwanath, and M. P. Zaletel, Ground State and Hidden Symmetry of Magic-Angle Graphene at Even Integer Filling, Phys. Rev. X 10, 031034 (2020).
- [46] K. Seo, V. N. Kotov, and B. Uchoa, Ferromagnetic Mott State in Twisted Graphene Bilayers at the Magic Angle, Phys. Rev. Lett. 122, 246402 (2019).

- [47] K. Hejazi, X. Chen, and L. Balents, Hybrid Wannier Chern bands in magic angle twisted bilayer graphene and the quantized anomalous Hall effect, Phys. Rev. Res. 3, 013242 (2021).
- [48] E. Khalaf, S. Chatterjee, N. Bultinck, M. P. Zaletel, and A. Vishwanath, Charged skyrmions and topological origin of superconductivity in magic-angle graphene, Sci. Adv. 7, eabf5299 (2021).
- [49] F. Xie, Z. Song, B. Lian, and B. A. Bernevig, Topology-Bounded Superfluid Weight in Twisted Bilayer Graphene, Phys. Rev. Lett. 124, 167002 (2020).
- [50] A. Julku, T. J. Peltonen, L. Liang, T. T. Heikkilä, and P. Törmä, Superfluid weight and Berezinskii-Kosterlitz-Thouless transition temperature of twisted bilayer graphene, Phys. Rev. B 101, 060505 (2020).
- [51] X. Hu, T. Hyart, D. I. Pikulin, and E. Rossi, Geometric and Conventional Contribution to the Superfluid Weight in Twisted Bilayer Graphene, Phys. Rev. Lett. 123, 237002 (2019).
- [52] J. H. Pixley and E. Y. Andrei, Ferromagnetism in magic-angle graphene, Science 365, 543 (2019).
- [53] M. Xie and A. H. MacDonald, Nature of the Correlated Insulator States in Twisted Bilayer Graphene, Phys. Rev. Lett. 124, 097601 (2020).
- [54] Y. Zhang, K. Jiang, Z. Wang, and F. Zhang, Correlated insulating phases of twisted bilayer graphene at commensurate filling fractions: A Hartree-Fock study, Phys. Rev. B 102, 035136 (2020).
- [55] R. M. Fernandes and J. W. F. Venderbos, Nematicity with a twist: Rotational symmetry breaking in a moiré superlattice, Sci. Adv. 6, eaba8834 (2020).
- [56] B. A. Bernevig, Z. D. Song, N. Regnault, and B. Lian, Twisted bilayer graphene. III. Interacting Hamiltonian and exact symmetries, Phys. Rev. B 103, 205413 (2021).
- [57] B. Lian, Z.-D. Song, N. Regnault, D. K. Efetov, A. Yazdani, and B. A. Bernevig, Twisted bilayer graphene. IV. Exact insulator ground states and phase diagram, Phys. Rev. B 103, 205414 (2021).
- [58] B. A. Bernevig, B. Lian, A. Cowsik, F. Xie, N. Regnault, and Z.-D. Song, Twisted bilayer graphene. V. Exact analytic many-body excitations in Coulomb Hamiltonians: Charge gap, Goldstone modes, and absence of Cooper pairing, Phys. Rev. B 103, 205415 (2021).
- [59] F. Xie, A. Cowsik, Z.-D. Song, B. Lian, B. A. Bernevig, and N. Regnault, Twisted bilayer graphene. VI. An exact diagonalization study at nonzero integer filling, Phys. Rev. B 103, 205416 (2021).
- [60] G. W. Burg, J. Zhu, T. Taniguchi, K. Watanabe, A. H. MacDonald, and E. Tutuc, Correlated Insulating States in Twisted Double Bilayer Graphene, Phys. Rev. Lett. 123, 197702 (2019).
- [61] C. Shen, Y. Chu, Q. S. Wu, N. Li, S. Wang, Y. Zhao, J. Tang, J. Liu, J. Tian, K. Watanabe, T. Taniguchi, R. Yang, Z. Y. Meng, D. Shi, O. V. Yazyev, and G. Zhang, Correlated states in twisted double bilayer graphene, Nat. Phys. 16, 520 (2020).
- [62] X. Liu, Z. Hao, E. Khalaf, J. Y. Lee, Y. Ronen, H. Yoo, D. Haei Najafabadi, K. Watanabe, T. Taniguchi, A. Vishwanath, and P. Kim, Tunable spin-polarized correlated states in twisted double bilayer graphene, Nature (London) 583, 221 (2020).
- [63] Y. Cao, D. Rodan-Legrain, O. Rubies-Bigorda, J. M. Park, K. Watanabe, T. Taniguchi, and P. Jarillo-Herrero, Tunable corre-

- lated states and spin-polarized phases in twisted bilayer-bilayer graphene, Nature (London) **583**, 215 (2020).
- [64] E. Khalaf, A. J. Kruchkov, G. Tarnopolsky, and A. Vishwanath, Magic angle hierarchy in twisted graphene multilayers, Phys. Rev. B 100, 085109 (2019).
- [65] C. Mora, N. Regnault, and B. A. Bernevig, Flatbands and Perfect Metal in Trilayer Moiré Graphene, Phys. Rev. Lett. 123, 026402 (2019).
- [66] Z. Hao, A. M. Zimmerman, P. Ledwith, E. Khalaf, D. H. Najafabadi, K. Watanabe, T. Taniguchi, A. Vishwanath, and P. Kim, Electric field–tunable superconductivity in alternatingtwist magic-angle trilayer graphene, Science 371, 1133 (2021).
- [67] J. M. Park, Y. Cao, K. Watanabe, T. Taniguchi, and P. Jarillo-Herrero, Tunable strongly coupled superconductivity in magic-angle twisted trilayer graphene, Nature (London) 590, 249 (2021).
- [68] Y. Zhang, R. Polski, C. Lewandowski, A. Thomson, Y. Peng, Y. Choi, H. Kim, K. Watanabe, T. Taniguchi, J. Alicea, F. von Oppen, G. Refael, and S. Nadj-Perge, Ascendance of superconductivity in magic-angle graphene multilayers, arXiv:2112.09270 [cond-mat.supr-con].
- [69] J. M. Park, Y. Cao, L.-Q. Xia, S. Sun, K. Watanabe, T. Taniguchi, and P. Jarillo-Herrero, Robust superconductivity in magic-angle multilayer graphene family, Nat. Mater. 21, 877 (2022).
- [70] G. Chen, A. L. Sharpe, P. Gallagher, I. T. Rosen, E. J. Fox, L. Jiang, B. Lyu, H. Li, K. Watanabe, T. Taniguchi, J. Jung, Z. Shi, D. Goldhaber-Gordon, Y. Zhang, and F. Wang, Signatures of tunable superconductivity in a trilayer graphene moiré superlattice, Nature (London) 572, 215 (2019).
- [71] G. Chen, L. Jiang, S. Wu, B. Lyu, H. Li, B. L. Chittari, K. Watanabe, T. Taniguchi, Z. Shi, J. Jung, Y. Zhang, and F. Wang, Evidence of a gate-tunable Mott insulator in a trilayer graphene moiré superlattice, Nat. Phys. 15, 237 (2019).
- [72] G. Chen, A. L. Sharpe, E. J. Fox, Y. H. Zhang, S. Wang, L. Jiang, B. Lyu, H. Li, K. Watanabe, T. Taniguchi, Z. Shi, T. Senthil, D. Goldhaber-Gordon, Y. Zhang, and F. Wang, Tunable correlated Chern insulator and ferromagnetism in a moiré superlattice, Nature (London) 579, 56 (2020).
- [73] H. Zhou, T. Xie, T. Taniguchi, K. Watanabe, and A. F. Young, Superconductivity in rhombohedral trilayer graphene, Nature (London) 598, 434 (2021).
- [74] L. Wang, E. M. Shih, A. Ghiotto, L. Xian, D. A. Rhodes, C. Tan, M. Claassen, D. M. Kennes, Y. Bai, B. Kim, K. Watanabe, T. Taniguchi, X. Zhu, J. Hone, A. Rubio, A. N. Pasupathy, and C. R. Dean, Correlated electronic phases in twisted bilayer transition metal dichalcogenides, Nat. Mater. 19, 861 (2020).
- [75] E. C. Regan, D. Wang, C. Jin, M. I. Bakti Utama, B. Gao, X. Wei, S. Zhao, W. Zhao, Z. Zhang, K. Yumigeta, M. Blei, J. D. Carlström, K. Watanabe, T. Taniguchi, S. Tongay, M. Crommie, A. Zettl, and F. Wang, Mott and generalized Wigner crystal states in WSe₂/WS₂ moiré superlattices, Nature (London) 579, 359 (2020).
- [76] P. Wang, G. Yu, Y. H. Kwan, Y. Jia, S. Lei, S. Klemenz, F. Alexandre Cevallos, R. Singha, T. Devakul, K. Watanabe, T. Taniguchi, S. L. Sondhi, R. J. Cava, L. M. Schoop, S. A. Parameswaran, and S. Wu, One-Dimensional Luttinger Liquids in a Two-Dimensional Moiré Lattice, Nature (London) 605, 57 (2022).

- [77] P. Moon and M. Koshino, Optical absorption in twisted bilayer graphene, Phys. Rev. B 87, 205404 (2013).
- [78] N. N. T. Nam and M. Koshino, Lattice relaxation and energy band modulation in twisted bilayer graphene, Phys. Rev. B 96, 075311 (2017).
- [79] S. Carr, S. Fang, Z. Zhu, and E. Kaxiras, Exact continuum model for low-energy electronic states of twisted bilayer graphene, Phys. Rev. Res. 1, 013001 (2019).
- [80] B. A. Bernevig, Z. D. Song, N. Regnault, and B. Lian, Twisted bilayer graphene. I. Matrix elements, approximations, perturbation theory, and a $k \cdot p$ two-band model, Phys. Rev. B **103**, 205411 (2021).
- [81] C. Wu, D. Bergman, L. Balents, and S. Das Sarma, Flat Bands and Wigner Crystallization in the Honeycomb Optical Lattice, Phys. Rev. Lett. **99**, 070401 (2007).
- [82] D. L. Bergman, C. Wu, and L. Balents, Band touching from real-space topology in frustrated hopping models, Phys. Rev. B 78, 125104 (2008).
- [83] J. Sichau, M. Prada, T. Anlauf, T. J. Lyon, B. Bosnjak, L. Tiemann, and R. H. Blick, Resonance Microwave Measurements of an Intrinsic Spin-Orbit Coupling Gap in Graphene: A Possible Indication of a Topological State, Phys. Rev. Lett. 122, 046403 (2019).
- [84] J. C. Slater and G. F. Koster, Simplified LCAO method for the periodic potential problem, Phys. Rev. 94, 1498 (1954).
- [85] E. McCann and V. I. Fal'ko, Landau-Level Degeneracy and Quantum Hall Effect in a Graphite Bilayer, Phys. Rev. Lett. 96, 086805 (2006).
- [86] Z.-D. Song, B. Lian, N. Regnault, and B. A. Bernevig, Twisted bilayer graphene. II. Stable symmetry anomaly, Phys. Rev. B **103**, 205412 (2021).
- [87] E. Tang, J.-W. Mei, and X.-G. Wen, High-Temperature Fractional Quantum Hall States, Phys. Rev. Lett. **106**, 236802 (2011).

- [88] G. Xu, B. Lian, and S.-C. Zhang, Intrinsic Quantum Anomalous Hall Effect in the Kagome Lattice Cs₂LiMn₃F₁₂, Phys. Rev. Lett. **115**, 186802 (2015).
- [89] R. Yu, X. L. Qi, A. Bernevig, Z. Fang, and X. Dai, Equivalent expression of \mathbb{Z}_2 topological invariant for band insulators using the non-Abelian Berry connection, Phys. Rev. B **84**, 075119 (2011).
- [90] A. Alexandradinata, X. Dai, and B. A. Bernevig, Wilson-loop characterization of inversion-symmetric topological insulators, Phys. Rev. B 89, 155114 (2014).
- [91] S. Haskell and A. Principi, Emergent hyper-magic manifold in twisted Kitaev bilayers, arXiv:2203.10963 [cond-mat.str-el].
- [92] H. C. Po, H. Watanabe, and A. Vishwanath, Fragile Topology and Wannier Obstructions, Phys. Rev. Lett. 121, 126402 (2018).
- [93] J. Cano, B. Bradlyn, Z. Wang, L. Elcoro, M. G. Vergniory, C. Felser, M. I. Aroyo, and B. A. Bernevig, Topology of Disconnected Elementary Band Representations, Phys. Rev. Lett. 120, 266401 (2018).
- [94] A. Bouhon, A. M. Black-Schaffer, and R.-J. Slager, Wilson loop approach to fragile topology of split elementary band representations and topological crystalline insulators with time-reversal symmetry, Phys. Rev. B 100, 195135 (2019).
- [95] G. W. Semenoff, Condensed-Matter Simulation of a Three-Dimensional Anomaly, Phys. Rev. Lett. 53, 2449 (1984).
- [96] A. H. Castro Neto, F. Guinea, N. M. R. Peres, K. S. Novoselov, and A. K. Geim, The electronic properties of graphene, Rev. Mod. Phys. 81, 109 (2009).
- [97] S. Bravyi, D. P. DiVincenzo, and D. Loss, Schrieffer-Wolff transformation for quantum many-body systems, Ann. Phys. 326, 2793 (2011).
- [98] T. Neupert and F. Schindler, Topological crystalline insulators, in *Topological Matter: Lectures from the Topological Matter School 2017*, edited by D. Bercioux, J. Cayssol, M. G. Vergniory, and M. Reyes Calvo (Springer International Publishing, Cham, 2018), pp. 31–61.